Joint EEG-fMRI signal model for EEG separation and localization

PENG SUN

DECLARATION

This work has not previously been accepted in substance for any degree and is not concurrently submitted in candidature for any degree.

Signed …….. (Candidate) Date……

STATEMENT 1

This thesis is being submitted in partial fulfilment of the requirements for the degree of MPhil

Signed …… (Candidate) Date ……

STATEMENT 2

This thesis is the result of my own independent work/investigation, except where otherwise stated. Other sources are acknowledged by explicit references

Signed …….. (Candidate) Date ……..

STATEMENT 3

I hereby give consent for my dissertation, if accepted, to be available for photocopying and for inter-library loan, and for the title and summary to be made available to outside organisations.

Signed …….. (Candidate) Date ……

Abstract

Electroencephalography (EEG) offers a rich representation of human brain activity in the time domain. EEG would in many circumstances be the preferred technique for analysing brain activity, as it is less expensive and more practical to use than other modalities such as functional Magnetic Resonance Imaging (fMRI), notably due to its size. However, its spatial resolution is limited, which hampers its ability to characterise activity across spatially distributed brain networks.

In comparison, functional Magnetic Resonance Imaging (fMRI) offers very good spatial resolution but the hemodynamic nature of the signal limits its temporal resolution to the order of seconds. A possible solution to this problem is to use both EEG and fMRI signals, but this approach would lead to the loss of convenience of EEG alone. Hence it is desirable to bring the advantages of an fMRI signal into EEG assessment of the brain's state and responses without the necessity for the presence of fMRI equipment on site.

In this work, a joint statistical model of fMRI/EEG signals is proposed and used for processing of EEG signals. The performance of a standard Blind Source Separation (BSS) method is compared with the new method, which uses the above joint EEG-fMRI model, which in turn shows improvement in the precision of both source separation and localisation.

List of Figures

List of Abbreviations

2D	Two-dimensional
3D	Three-dimensional
BEM	Boundary element method
BOLD	Blood oxygen level dependent
BSS	Blind source separation
EEG	Electroencephalography
ERP	Event related potential
FDM	Finite difference method
FEM	Finite element method
FMRI	Functional magnetic resonance imaging
GMM	Gaussian mixture model
HRF	Hemodynamic response function
ICA	Independent component analysis
MN	Minimal norm
MRI	Magnetic resonance imaging
MRJI	Model reduced joint inverse
POWR	Power constrained
SOBI	Second order blind identification
SPM	Statistical parametric mapping

Contents

1. Introduction

1.1 Motivation

Electroencephalography (EEG) records brain activity by placing electrodes on the surface of the scalp. Neural activity recording is quite important, because it is widely used in many areas, such as physiology, neuroscience, medicine and engineering. Neural activity can be used to diagnose different brain diseases such as, for example, Parkinson's **[10]**. Rita Levi-Montalcini (1986 Nobel Prize winner in Medicine) said, "At the beginning of the third millennium, due to prolonged aging, neurodevelopment disorders are growing and a much deeper knowledge of the brain is necessary" **[41]**. In addition, neural activity recording could be used to improve the quality of human life. In 2012, a research group at Brown University researched methods based on brain-computer interface in order to allow people with paralysis to control a prosthetic robotic arm **[7]**.

The EEG signals of the human brain were first recorded by Han Berger in the 1920s **[33]**. He used a one-channel bipolar method with fronto-occipital leads in his experiments. Nowadays, up to 256 channels can be used for measurement. Scalp EEG has a number of advantages over other brain activity recording techniques. More specifically, it records neural activity directly, has high temporal resolution, and is non-invasive and relatively inexpensive. However, EEG's lack of spatial resolution limits its scope in measuring neural activity. In addition, the recorded EEG signals are a mixture of sources inside the brain, the precise locations of which we do not know and hence they may be difficult to interpret.

Compared with EEG measurement, functional magnetic resonance imaging (fMRI) technology measures oxygen concentration change in the brain caused by the neural activity of the brain. fMRI can offer ideal spatial resolution but lacks the temporal resolution, as the hemodynamic signals record is naturally limited in this regard. In addition, fMRI does not show the neural activity directly and,

hence, these signals may also be difficult to interpret.

Multimodal technology combining EEG and fMRI shows the benefits of using complementary signals to describe neural activity more fully **[26]**. It was also shown that joint EEG-fMRI can improve both EEG source separation and localisation **[30]**.

EEG source separation and localisation is quite important, especially in clinical applications, because accurate source separation is important to disease prevention and recognition. In addition, different areas of the brain control different human functions, which can be used in the interpretation of brain signals and the study of brain functionality.

Source separation is the process of separating several mixed observation signals into several original signals; one classic example of application of source separation is the cocktail party problem. Another special application of source separation is brain signal processing. Due to the fact that nothing is known about the original source signals, blind source separation is used to extract the sources. We usually use Independent Component Analysis (ICA) to solve this problem **[20]**. ICA is a method for finding the underlying factors or components from multivariate statistical data **[20]**. There are many different existing implementations of ICA, such as FastICA and Second Order Blind Identification (SOBI) **[32]**, but none of them can separate the brain sources perfectly due to the complexity of the problem **[32]**.

By source localisation we mean finding the positions of the original signals in the brain as opposed to the signals recorded on the scalp surface. Source localisation is related to forward and inverse problems **[6]**. The forward problem is finding the scalp potential that would result from hypothetical dipoles, or more generally from a current distribution inside the head. The inverse problem uses the actual EEG data measured at specified positions of electrodes on the scalp to work back and estimate the sources that fit these measurements **[14]**. The solution to the forward problem is based on the Maxwell equation **[39]** and the solution to the inverse problem is based on the ICA algorithm. Source localisation is essential

for neural surgery, as the diagnosis of some neural diseases requires the accurate localisation of brain signals. More accurate localisation can potentially improve post-surgical prognosis. Some ICA algorithms are used for source localisation, such as SOBI. SPM5 (statistical parametric mapping) is a software application that can be used for solving the source localisation problem, but the problem of localisation itself has not been solved fully either.

1.2 Aim and objectives

In my research, I worked on improving both EEG source separation and localisation. My motivation stems from two reasons. Firstly, both separation and localisation are not solved completely; in other words, there is much room for improvement. Secondly, EEG source separation and localisation can be used in many areas, such as neuroscience, engineering and physiology. Finally, these problems are very challenging and hence represent a good research topic.

My approach to solving the above problems will rely on the hypothesis that fMRI-assisted EEG source separation and localisation shows better results than EEG only.

The main aim of this research is to develop new signal processing methods to make EEG source separation and localisation more accurate. The solution to the problem addressed by this research will contribute to the neuroscience and clinical fields, because accurate EEG source separation and localisation are very important in those fields.

The main objectives of my research are as follows:

1. Develop a set of generative features describing EEG and fMRI signals to decrease the dimensionality of the data by removing irrelevant information and unwanted noise.
2. Create a model of the correlations between EEG and fMRI data to remove the necessity of using fMRI machines for fMRI-assisted EEG separation.
3. Develop a method for source separation of EEG data relying on the above model of correlations to increase the accuracy of source separation from EEG only.
4. Develop a method for source localisation of EEG data relying on the above model of correlations to increase the precision of source localisation from EEG only.
5. Develop the framework for more accurate EEG source separation and localisation based on a joint EEG and fMRI model of correlations.

2. Medical Background

2.1 EEG

EEG is an abbreviation for electroencephalogram; it means the electrical neural activity of the brain. EEG is the record and measurement of electrical signals created in the brain; it is widely used in many areas such as engineering, medicine, psychology and biology. The measurement of a scalp EEG signal is shown in Figure 2.1 **[40]**.

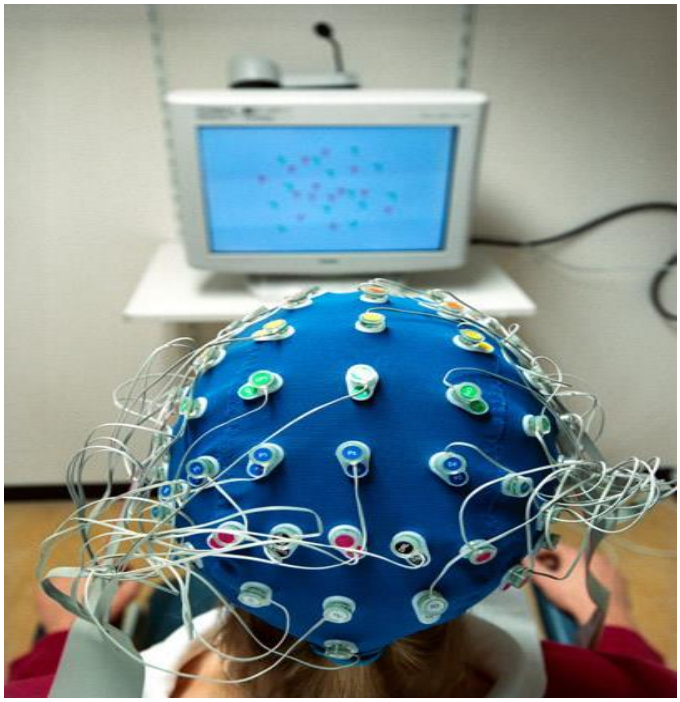

Figure 2.1 The measurement of a scalp EEG signal **[40]**

The measurement of an EEG signal occurs via current flow during synaptic excitations of dendrites of a large number of pyramidal neurons in the cerebral cortex. The current in the brain is mainly generated by pumping the positive ions of sodium, calcium and potassium and the negative ions of chlorine.

The most popular method of EEG signal measurement in recent years has been the 10-20 system electrode placement method, which can be called the

international 10-20 system; but interestingly, the 10 or 20 does not denote the number of electrodes, but represents the percentage of the length (10% or 20%) between them, which is shown in the right graphic of Figure 2.2. The 3D and 2D maps of the 10-20 system are presented in Figure 2.2.

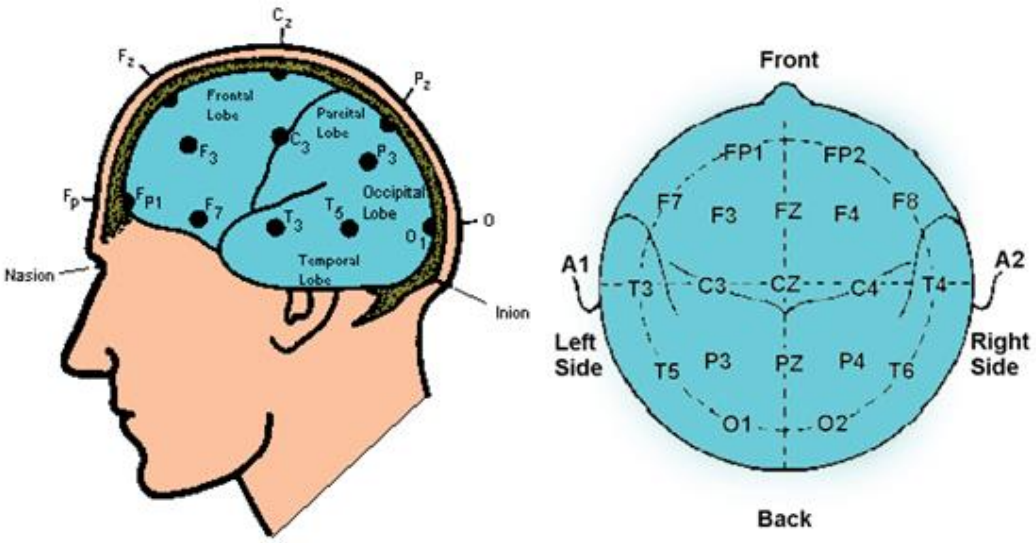

Figure 2.2 3D and 2D maps of 10-20 system [2]

There are five lobes: Frontal lobe (F), Temporal lobe (T), Central lobe (C), Parietal lobe (P) and Occipital lobe (O) **[4][38]**, and there are five points between the nasion (the point between the forehead and nose) and the inion (the bump at the back of the skull): Fp (Front polar), Front (F), Centre C), Partial (P) and Occipital (O). The distance between Front polar and nasion occupy 10% of the whole length, and the distance between Occipital and inion occupy 10% of the whole distance. The other four distances, which are the distance between Fp (Front polar) and Front (F), between Front (F) and Centre (C), between Centre (C) and Parietal (P), and between Parietal (P) and Occipital (O) occupy 20% of the whole distance. Z replaces the electrode placed on the middle line, the bigger number means the further in position to the middle line, while in contrast the smaller number replaces the closer the position to the middle line. Odd numbers represent the left hemisphere while even numbers the right hemisphere.

2.2 fMRI

Functional magnetic resonance imaging (fMRI) has rapidly developed since the 1990s; it is based on the magnetic resonance imaging (MRI) technique and records brain function activity. The MRI technique includes multi-parameter, multi-faceted characteristics and can provide high resolution and high comparability of anatomy.

Functional magnetic resonance imaging (fMRI) is the sort of specialised MRI scan used to measure the hemodynamic response related to neural activity in the brain or spinal cord of humans or other animals. There are some differences between traditional MRI and fMRI methods. Traditional MRI uses the structure of water molecules in the hydrogen nucleus, where the magnetic field occurs due to a magnetic resonance phenomenon, which shows imaging with the tissue structures. FMRI is the direct measurement from blood flow via the brain as it is being stimulated; therefore, the result could be functionally changed during disease.

Blood oxygen level dependence (BOLD) is the most widely used method of fMRI. It measures blood oxygen changes in the different locations of the brain's function areas. For humans, the weight of the brain only occupies 2% of their whole weight, but the consumption of oxygen approximately takes up a total of 20%. When the brain carries out a special task or responds to stimulus, some areas of the neuronal activity increase suddenly, caused by a blood flow increase, and this leads to a misbalance between the oxygen provided and consumed in the blood **[27]**, **[28]**. The fMRI measurement picture is shown in Figure 2.3 **[18]**.

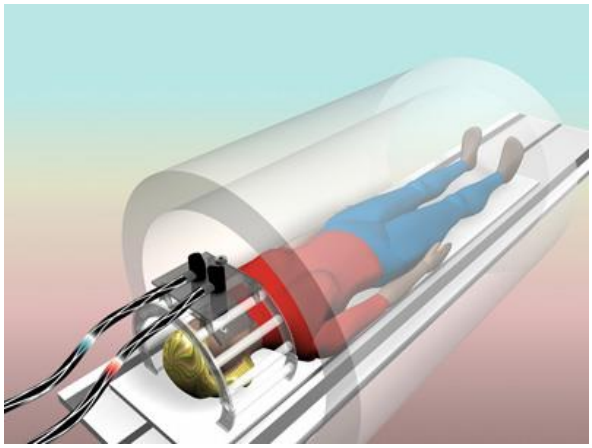

Figure 2.3 fMRI scanner measuring model [10]

An fMRI scanner has a powerful electro-magnetic field, while a typical scanner has a 3 tesla magnetic field, which is around 5000 times larger than Earth's field **[2]**. A scan magnetic field influences the magnetic nuclei of atoms. Atomic nuclei are randomly oriented but under the effect of a magnetic field the nuclei combine with the direction of the field. When pointing in the same direction, the small magnetic signals from individual nuclei add up coherently, resulting in a signal that is enough to measure. In fMRI, the magnetic signal from hydrogen nuclei in water (H2O) is detected **[17]**.

The core of MRI is that the signal from hydrogen nuclei changes in strength depending on the surroundings. This provides a means of discriminating among gray matter, white matter and cerebral spinal fluid in structural images of the brain **[17]**.

Oxygen is delivered to neurons by haemoglobin in capillary red blood cells. When neuronal activity increases there is an increased demand for oxygen and the local response is an increase in blood flow to regions of increased neural activity **[2]**.

Haemoglobin is diamagnetic when oxygenated but paramagnetic when deoxygenated. The difference in magnetic properties causes small differences in the magnetic resonance signal of blood depending on the degree of oxygenation. Since blood oxygenation varies according to the levels of neural activity these

differences could be used to detect brain activity. This form of MRI is known as blood oxygenation level dependent (BOLD) imaging **[17]**. One example of fMRI measurement can be shown in Figure 2.4 **[17]**.

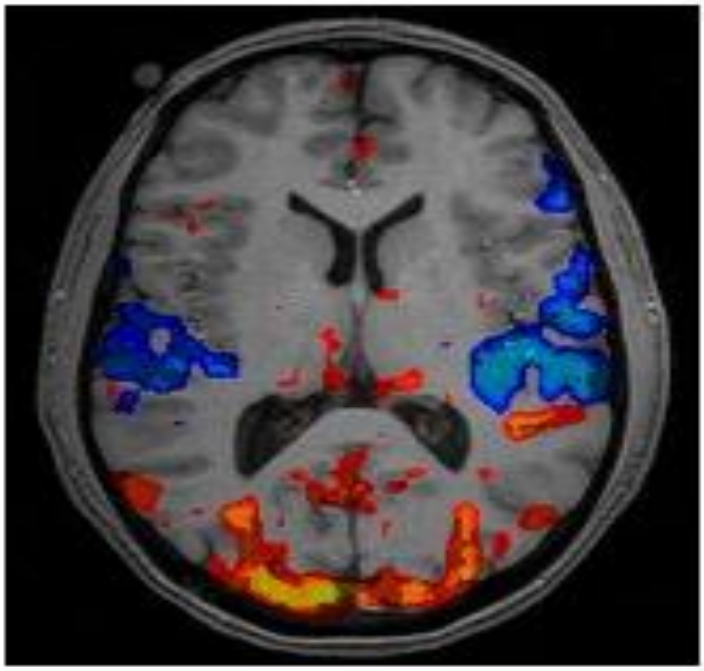

Figure 2.4 One fMRI measurement result **[17]**

2.3 Joint EEG and fMRI

EEG and fMRI can offer complementary spatial and temporal information about the brain's function **[9]**. EEG could offer good temporal resolution, as it can reach milliseconds, but it lacks high spatial resolution. There are many methods for combining the information in modalities using a constrained analysis.

There are many researchers working on joint EEG and fMRI. For example, Bledowski researched how to combine the event-related potential and FMRI **[2]**. Bonmassar worked on spatiotemporal images of the brain using joint EEG and fMRI **[3]**. Debener worked on a trial by trial coupling of concurrent EEG and fMRI to identify the dynamics of performance monitoring **[11]**. In recent years, more and more methods and applications have been used in joint EEG and fMRI models, whereby the aim is to use fMRI's good spatial resolution to improve EEGs.

3. Independent Component Analysis

3.1 Independent Component Analysis

Independent Component Analysis (ICA) is a computational method for separating a multivariate signal into additive subcomponents assuming the mutual statistical independence of the non-Gaussian source signals.

The ICA algorithm uses the known observation matrix to estimate the source signals. The general ICA model is seen in equation (3.1) **[20]**.

$$\begin{pmatrix} \boldsymbol{x}_1(t) \\ \boldsymbol{x}_2(t) \\ \vdots \\ \boldsymbol{x}_m(t) \end{pmatrix} = \mathbf{L} \begin{pmatrix} \boldsymbol{s}_1(t) \\ \boldsymbol{s}_2(t) \\ \vdots \\ \boldsymbol{s}_n(t) \end{pmatrix} \tag{3.1}$$

The matrix **X** is the observation matrix, it is the known matrix from measurement, and the mixing matrix **L** is some unknown matrix. The aim of the ICA algorithm is to estimate the matrix **L** and source signal $\boldsymbol{s}_i(t)$, with the subscript 'i' denoting the integer number between *1* and n. Even for the same observation matrix, different methods perform differently.

ICA data analysis can be used in many areas including digital imaging, document databases, economics and medical data **[20]**. ICA is the most important method for blind source separation; the word "blind" means that both the mixing matrix and source signal are unknown. ICA does not have a unique solution, but it is able to obtain the approximately estimated result. The aim for each estimated subcomponent should be as independent as possible.

EEG offers a good temporal resolution but poor spatial resolution, whereas fMRI is good at spatial resolution but has a lack of temporal resolution. An ICA algorithm can also be applied in two ways: spatial and temporal, which will be

discussed below.

3.1.1 Spatial ICA

The first application of spatial ICA on fMRI data was done by McKeown **[25]**. In the spatial ICA model, the brain's areas carry out different tasks and assume spatial independence. Each of these areas can be considered as an independent component with a time course. Based on statistics and their independent definition, the spatial independence can be written down as equation (3.2):

$$p(S_1, S_2, \dots, S_n) = \prod_{i=1}^{n} p_i(S_i) \qquad (3.2)$$

Where S_i is the *i*-th independent and the joint probability density function (pdf) p_i (.) is the multiplication of the marginal pdfs of the components. As for the conventional ICA model, the spatial ICA model can be defined as below:

$$\mathbf{X} = \mathbf{L} \cdot \mathbf{S} \qquad (3.3)$$

In equation (3.3), **X** is a T×V matrix of the mixtures, T is the length of an fMRI scan, V denotes the number of brain voxels involved in analysis, **S** is an N×V matrix of unknown sources, **L** is a T×N mixing matrix and N is the number of unknown spatially independent sources. Each column of **L** denotes the time course of the corresponding independent component. In this model, fMRI signals could be decomposed into a number of spatially independent components **S** and their associated time course of activation **L**. The spatial components can be estimated from:

$$\mathbf{S} = \mathbf{W} \cdot \mathbf{X} \qquad (3.4)$$

Where **W** is the unmixing matrix to be estimated and the size of **W** is an N×T. The aim of spatial ICA is to find the appropriate unmixing matrix **W [21].**

3.1.2 Temporal ICA

Spatial ICA can obtain different spatial ICA components whereas temporal ICA could obtain different temporal ICA components. The formula of temporal ICA forms is the same as the spatial ICA shown as equation (3.3) but the mixture matrix **X** of temporal ICA is the transpose matrix of spatial ICA. In other words, the size of the mixture matrix **X** of temporal ICA is V×T, the mixing matrix **L** is V×M, M is the number of unknown temporal independent sources, while **S** is a M×T matrix of unknown sources.

The temporal component can be estimated from equation (3.4), as the size of unmixing matrix **W** is M×V. Similarly, the main purpose of temporal ICA is to obtain the suitable unmixing matrix **W**. Figure 3.1 illustrates the comparison of spatial and temporal ICA.

Based on the good spatial resolution of fMRI, a spatial ICA algorithm is often used for fMRI data. In contrast, temporal ICA is used for EEG data, because of the good temporal resolution of EEG. Therefore, for a joint EEG-fMRI model, if the research is more based on EEG data, it is better to use the temporal ICA; otherwise, it is better to use the spatial ICA. One simple way to estimate the unmixing matrix **W** is to find the pseudo inverse of the mixing matrix **L**. According to the pseudo inverse definition, the unmixing matrix can be written down as equation (3.5) **[33]**.

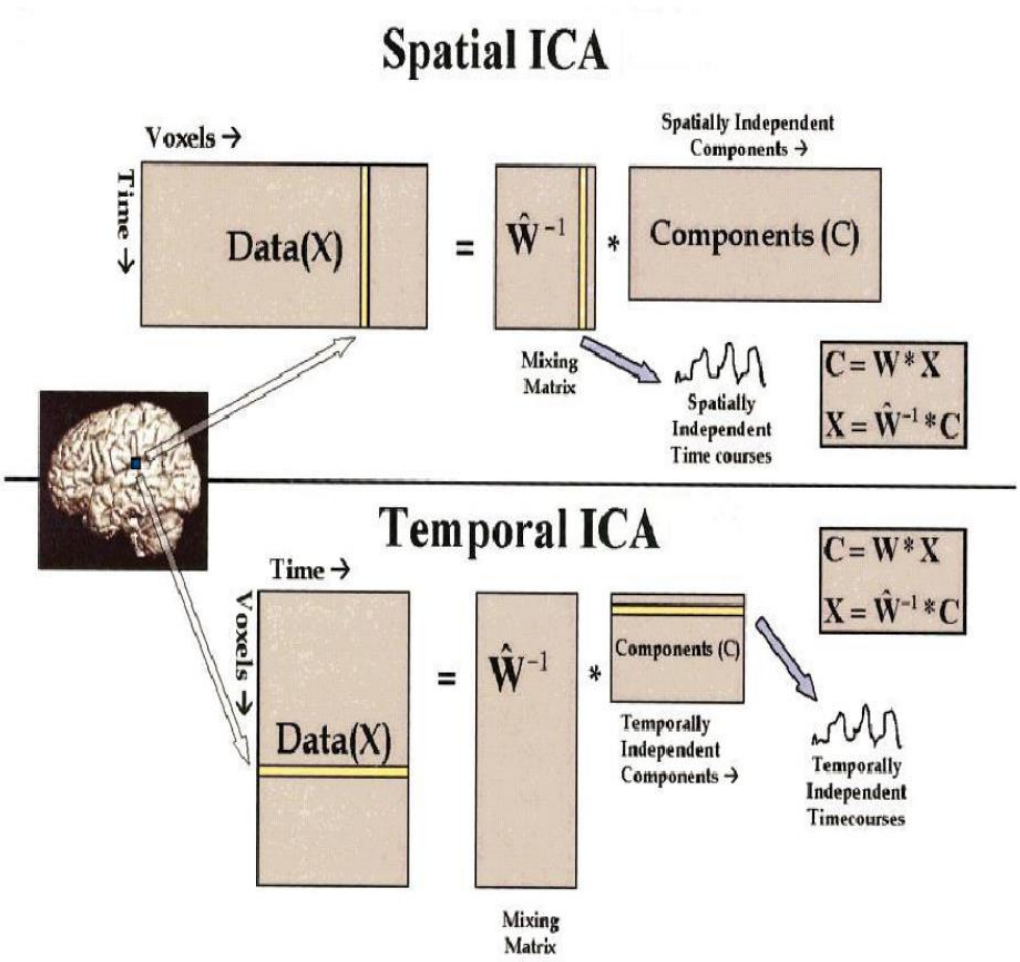

Figure 3.1 Comparison of spatial and temporal ICA **[21]**

$$\mathbf{W} = (\mathbf{L}^{\mathbf{T}} \cdot \mathbf{L})^{-1} \cdot \mathbf{L}^{\mathbf{T}} \tag{3.5}$$

And the estimation of the source matrix from equation (3.4) can be written down as equation (3.6):

$$\mathbf{S} = (\mathbf{L}^{\mathbf{T}} \cdot \mathbf{L})^{-1} \cdot \mathbf{L}^{\mathbf{T}} \cdot \mathbf{X} \tag{3.6}$$

In many cases, the unmixing matrix $\mathbf{W}$ cannot use the inverse of the mixing matrix directly. Due to the system being highly underdetermined, the size of mixing matrix $\mathbf{L}$ is T×N and the number of T is much less than the number of N; therefore, the different regularised methods could result in different solutions.

3.1.3 Minimum norm solution

The Minimum Norm (MN) is the generally applicable solution for an underdetermined ICA problem. This solution was proposed by Hamalainen **[16]**.

Let us define the matrix $\boldsymbol{\Gamma}$ as the square of the mixing matrix $\mathbf{L}$. It exists according to the relation (3.7). Eigendecompose the square matrix $\boldsymbol{\Gamma}$, as in equation (3.8), so each column of the matrix $\boldsymbol{V}$ is the eigenvector of the matrix $\boldsymbol{\Gamma}$, and meanwhile the matrix $\boldsymbol{V}$ is orthogonal matrix, as shown in equation (3.9).

$$\boldsymbol{\Gamma} = \mathbf{L}\mathbf{L}^{\mathbf{T}} \tag{3.7}$$

$$\boldsymbol{\Gamma} = \boldsymbol{V}\boldsymbol{\Lambda}\boldsymbol{V}^{\boldsymbol{T}} \tag{3.8}$$

$$\boldsymbol{I} = \boldsymbol{V}\boldsymbol{V}^{\boldsymbol{T}} \tag{3.9}$$

The diagonal matrix $\boldsymbol{\Lambda}$ is shown in equation (3.10).

$$\boldsymbol{\Lambda} = \boldsymbol{diag}(\boldsymbol{\lambda_1}, \boldsymbol{\lambda_2}, \dots, \boldsymbol{\lambda_M}) \tag{3.10}$$

Where $\boldsymbol{\lambda_1} > \boldsymbol{\lambda_2} > \cdots > \boldsymbol{\lambda_M}$ are the eigenvalues, and each column of the matrix $\boldsymbol{V}$ is an eigenvector. Then equation (3.11) is the inverse of the matrix $\boldsymbol{\Gamma}$

$$\boldsymbol{\Gamma^{-1}} = \boldsymbol{V}\boldsymbol{\Lambda^{-1}}\boldsymbol{V^T} \tag{3.11}$$

Regularisation may be carried out by replacing $\boldsymbol{\Lambda^{-1}}$ by equation (3.12).

$$\breve{\boldsymbol{\Lambda}}^{\boldsymbol{-1}} = \boldsymbol{diag}(\boldsymbol{\lambda_1^{-1}}, \boldsymbol{\lambda_2^{-1}}, \dots, \boldsymbol{\lambda_K^{-1}}) \tag{3.12}$$

The number $K \leq M$ is selected so that the regularised minimum norm estimation does not contain excessive contribution from noise.

To obtain a regularised inverse matrix of $\boldsymbol{\Gamma}$ it can be shown as equation (3.13).

$$\widetilde{\boldsymbol{\Gamma}^{-1}} = \boldsymbol{V}\breve{\boldsymbol{\Lambda}}^{-1}\boldsymbol{V}^{\boldsymbol{T}} \tag{3.13}$$

The solution of the minimum norm is shown in equation (3.14) **[15].**

$$\breve{\boldsymbol{S}} = \boldsymbol{L}^{\boldsymbol{T}}(\widetilde{\boldsymbol{\Gamma}^{-1}}\boldsymbol{E}) \tag{3.14}$$

3.2 Joint EEG-fMRI separation

Since the sources of interest in the EEG and joint EEG-fMRI signals are not directly observed we use blind source separation and independent component analysis, which is an efficient approach for recovering the unknown sources from the sensor signals.

There are many researchers working on BSS for EEG and fMRI. For example, Liu et al.'s work is based on the spatiotemporal images of the brain by combining the EEG and fMRI signals **[24]**. Eichele et al. studied unmixing concurrent EEG-fMRI signals with parallel ICA **[12]**.

ICA is one important application of BSS, which is an approach used to estimate the independent source signals observed at the record channels. Acoustic signal BSS usually means the separation of individual sounds from many recordings in an uncontrolled conditions. The BSS technique is widely used in different areas, like medical signal processing, communication systems, the financial field, imaging processing and voice signal processing.

In general, the convolutive BSS algorithms are not considered for real world application scenarios due to their complexity, when the observation signals are delayed and the recorded data is a result of the convolution of many signals. The convolutive BSS algorithms cannot evaluate the exact latency between the mixed received signals. In addition, noise may exist, but not white noise as it is often assumed. The instantaneous case (whereby the source signals arrived at the sensor without delays) is the simplest method and the most widely used. This is used for the EEG signals, which have narrow bandwidth and low sampling frequency.

EEG separation is a kind of inverse problem and is one application of BSS. There are several methods for EEG separation. Bayesian statistical methods were proposed by Phillips et al. **[29]**. A minimal norm algorithm was proposed by Hamalainen in **[16]** and Grech in **[14]**. Weighted minimal norm was proposed by

Grech in **[14]** and Brown in **[6]**. Joint EEG-fMRI separation, which combines the spatial information of fMRI, could get better results than EEG separation alone, such as the Infomax algorithm by Bell in **[1]** and Hyvarinen in **[20]**. Other suggestions are FastICA algorithm by Hyvarinen in **[19]**, Power constraint (PowR) proposed by Brown in **[6]**, the fMRI regularised inverse method proposed by Brookings in **[5]**, and model reduced joint inverse (MRJI) described by Brown in **[6]** and Brooking et al. in **[5]**.

3.2.1 General EEG separation

This section describes a standard approach to EEG only source separation.

Firstly, EEG separation is similar to ICA, which is defined as equation (3.3), where **X** is the matrix of electrode voltage, also called model observation matrix. **L** is the linear Green's function, which propagates the interior sources to the scalp, and **S** is the desired source matrix.

The equation (3.15) is based on the least-square rules, the solution to which is given in equation (3.14). In order to obtain the accurate desired source matrix, model least square function $\mathrm{f}_{\mathrm{EEG}}(\mathbf{S})$ should be minimised. $\mathrm{f}_{\mathrm{EEG}}(\mathbf{S})$ is used for EEG term estimation as below **[6]**.

$$\mathrm{f}_{\mathrm{EEG}}(\mathbf{S}) = \frac{1}{2}\mathrm{Tr}\{(\mathbf{X}-\mathbf{LS})^{\mathrm{T}}(\mathbf{X}-\mathbf{LS})\} \tag{3.15}$$

$$\mathrm{C}(\mathbf{S}) = \frac{1}{2}\mathrm{Tr}\left\{(\mathbf{X}-\mathbf{LS})^{\mathrm{T}}\Sigma_{\mathbf{X}}^{-1}(\mathbf{X}-\mathbf{LS})\right\} + \frac{\mu_1}{2}\mathrm{f}_{\mathrm{fMRI}}(\mathbf{S}) + \frac{\mu_2}{2}\mathrm{f}_{\mathrm{R}}(\mathbf{S}) \tag{3.16}$$

The joint cost function can be shown as in equation (3.16), which needs to be minimised. The first term of equation (3.16) denotes the fit to the EEG data **X** whereby $\Sigma_{\mathbf{X}}$ is the electrode-electrode covariance matrix. The second term is the fit to fMRI data and the third term is a regularising term. In other words, the second term constrains the fMRI, and the third term is the regularising constraint. The two terms will be different in different algorithms. Generally μ_1 and μ_2

are both set equal to 1 **[6]**. But for EEG only separation, the $f_R(\mathbf{S})$ does not exist, as it is equal to zero.

In practice, the dimension of data is huge, much of which is redundant, and therefore reducing the data's dimensionality could improve the efficiency of the algorithm. Equation (3.17) describes the collection of task-related data extracted from measurements, but obviously the task-related data is much smaller (usually by more than 100 times) than the measurement.

$$\mathbf{S} = \boldsymbol{\alpha}\boldsymbol{\varepsilon} \tag{3.17}$$

Where $\boldsymbol{\varepsilon}$ is the averaged, smoothed, task-related EEG sources, $\boldsymbol{\alpha}$ is the task-related matrix and the size is much smaller (usually 100 or more) than **S**. We can apply equation (3.17) to equation (3.16) to get a new cost function as seen in equation (3.18):

$$C(\boldsymbol{\alpha}) = \frac{1}{2}\mathrm{Tr}\left\{(\mathbf{X} - \mathbf{L}\boldsymbol{\alpha}\boldsymbol{\varepsilon})^T \Sigma_{\mathbf{X}}^{-1}(\mathbf{X} - \mathbf{L}\boldsymbol{\alpha}\boldsymbol{\varepsilon})\right\} + \frac{\mu_1}{2} f_{\mathrm{fMRI}}(\boldsymbol{\alpha}) + \frac{\mu_2}{2} f_R(\boldsymbol{\alpha}) \tag{3.18}$$

This section describes the joint EEG-fMRI source separation. The joint EEG and fMRI flow chart is shown in Figure 3.2, whereby the blue part is the EEG part, including detrend electrode, temporal ICA, task-related source activity, electrode loaclation, smooth and lead field. Both red and green parts are the MRI part, including correct slice timing, within subject registration, spatial normalisation, detrend voxels, segment, wrap and reslice, spatial ICA, task-related activity, weight and average.

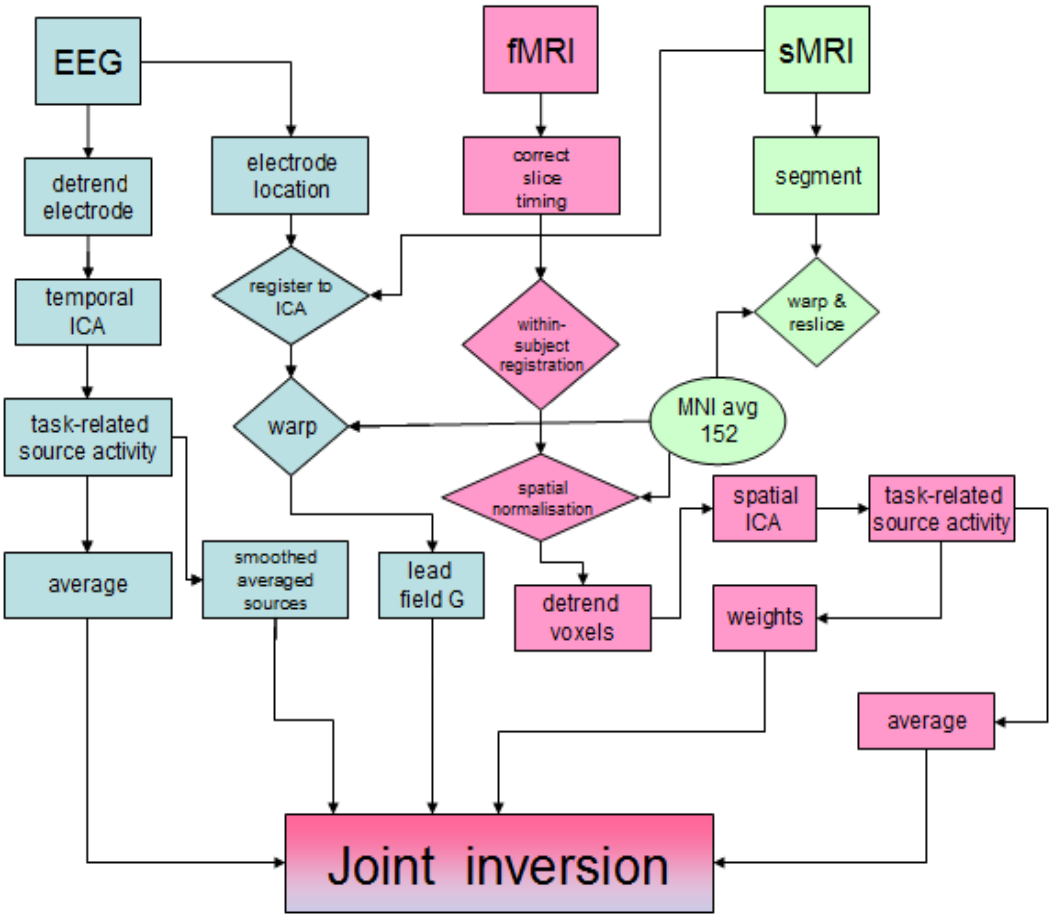

Figure 3.2 Flow chart of joint EEG and fMRI inversion. Adopted from **[6]**

3.2.2 Power constrained (PowR)

There are several methods for joint EEG and separation, and the one regulation is power constrained (PowR), which was proposed by Brown **[6]**. There is no regularising term, and the final term of equation (3.4) is zero. The fMRI fitting term takes the form as equation (3.19).

$$f_{fMRI}(\boldsymbol{\alpha}) = \frac{1}{\sigma_P^2}(\lambda \mathbf{p} - P(\boldsymbol{\alpha}))^T(\lambda \mathbf{p} - P(\boldsymbol{\alpha})) \qquad (3.19)$$

The number σ_P^2 is the variance of the distribution of voxel power, the scalar λ absorbs the unknown conversion between BOLD units and solution intensity can

be calculated from $\partial \mathbf{C}/\partial \lambda$. $\mathbf{C}=\boldsymbol{\varepsilon}\boldsymbol{\varepsilon}^{\mathbf{T}}$. The vector $\mathbf{p}$ is the observed fMRI signal power at each solution point; the i-th element can be computed from the reconstructed BOLD data B as equation (3.20).

$$\mathbf{p}_{\boldsymbol{i}} = \sum_{\mathrm{t}} \mathrm{B}_{it}^{2} \tag{3.20}$$

The vector $\mathrm{P}(\boldsymbol{\alpha})$ is the calculated solution power, which for parameter $\boldsymbol{\alpha}$ can be seen in equation (3.21) **[6]**.

$$\mathrm{P}_{i}(\boldsymbol{\alpha}) = [\boldsymbol{\alpha}\mathbf{C}\boldsymbol{\alpha}^{\mathbf{T}}]_{ii} \tag{3.21}$$

The cost function of the Power constrained (PowR) method can be written as equation (3.22).

$$\mathrm{C}(\boldsymbol{\alpha}) = \frac{1}{2}\mathrm{Tr}\{(\mathbf{X}-\mathbf{L}\boldsymbol{\alpha}\boldsymbol{\varepsilon})^{\mathrm{T}}\Sigma_{\mathbf{X}}^{-1}(\mathbf{X}-\mathbf{L}\boldsymbol{\alpha}\boldsymbol{\varepsilon})\} + \frac{1}{2} * \frac{1}{\sigma_{\mathrm{P}}^{2}}\left(\lambda\mathbf{p}-\mathrm{P}(\boldsymbol{\alpha})\right)^{\mathrm{T}}(\lambda\mathbf{p}-\mathrm{P}(\boldsymbol{\alpha})) \tag{3.22}$$

3.2.3 Model reduced joint inverse (MRJI)

Another joint EEG and fMRI separation regulation is model reduce joint inverse (MRJI), which was created by Brown **[6]**. The cost function of MRJI can be defined as equation (3.23). There are two terms of cost function: EEG and fMRI. The aim is to obtain EEG and fMRI symmetrically as possible.

$$\mathrm{C}(\boldsymbol{\alpha},\lambda,\mathrm{k}) = \frac{1}{2}\mathrm{Tr}\{(\mathbf{X}-\mathbf{L}\boldsymbol{\alpha}\boldsymbol{\varepsilon})^{\mathrm{T}}(\mathbf{X}-\mathbf{L}\boldsymbol{\alpha}\boldsymbol{\varepsilon})\} + \frac{\mathrm{g}}{2} * \mathrm{Tr}\{(\lambda\mathbf{B}+\mathrm{k}\mathbf{I}-\boldsymbol{\alpha}\boldsymbol{\beta})^{\mathrm{T}}(\lambda\mathbf{B}+\mathrm{k}\mathbf{I}-\boldsymbol{\alpha}\boldsymbol{\beta})\} \tag{3.23}$$

The matrix $\boldsymbol{\beta}$ contains the fMRI source, $\mathbf{B}$ denotes the BOLD activity; we assume that the fMRI activity can be written as a linear combination of the fMRI basis function, corresponding to calculate the BOLD response to the EEG source $\boldsymbol{\varepsilon}$**.** The scalar g is the gain term to balance the weight of both the EEG and fMRI term, and aims to make the same magnitude to balance the weight of the EEG and fMRI term **[6]**.

3.2.4 FMRI regularised inverse

FMRI regularised inverse is one of the regularization methods for joint EEG and fMRI separation proposed by Brooking **[5]**. FMRI regularised inverse aims to use independent fMRI data to select between the many infinite solutions given by the EEG data. To construct fMRI regularised inverse, one considered solution can be written as equation (3.24).

$$\mathbf{S} = \mathbf{L}^{+}\mathbf{X} + \mathbf{N_L}\boldsymbol{\alpha} \tag{3.24}$$

Superscript "+" denotes the pseudo inverse and $\mathbf{N_L}$ whose columns are equal to the row number of $\boldsymbol{\alpha}$ in the null space of L. The regularised rule of fMRI regularised inverse can be seen in equation (3.25).

$$\sigma\mathbf{B} = \min_{\{\boldsymbol{\alpha},\lambda,k\}} \| |\mathbf{L}^{+}\mathbf{X} + \mathbf{N_L}\boldsymbol{\alpha}| - \lambda\mathbf{B} + k\mathbf{I}\| \tag{3.25}$$

We can minimise equation (3.25) to get the final result of the fMRI regularised inverse model **[5]**. All three of these algorithms (PowR, MRJI, fMRI regularised) are part of a joint EEG-fMRI model, but they are different.

For PowR, it must be solved through an iterative method. While cost function is no longer a simple quadratic, it is not highly non-linear or merely quartic, but it is a relative mild nonlinearity.

FMRI has a regularised start with minimum norm for inversion of the EEG data, then improves the agreement with EEG regularised. And cost function is not a linear function but the non-linearity is also mild enough. It is easy to implement, but the vital disadvantage is that we cannot make use of the realistic model of BOLD response because it does not have an estimate of how the neural activities vary with time until it creates its solution.

The MRJI model has several advantages; firstly, it is a more accurate treatment of BOLD. Secondly, its linearity guarantees that the speed and the size of inverse

are reduced dramatically. Thirdly, this procedure allows EEG and fMRI data to be inversed simultaneously, and the weight of EEG and fMRI are equal. MRJI performs extremely well in tests on synthetic data but is less successful with human subject data, as the drawback is that each row is identical **[6]**. Having compared it with different methods, the MRJI method was adopted for the experiment.

4. Proposed Method

This chapter will firstly introduce the proposed method for EEG source separation, which is based on joint EEG and fMRI separation method (MRJI) described in Chapter 3. It will then introduce the process of EEG localisation.

4.1 Proposed method

In this research, we will use joint EEG-fMRI separation based on the statistical model of correlations between EEG and fMRI prior recordings.

The flow chart of joint EEG and fMRI with GMM is shown in Figure 4.1. It is similar to Figure 3.2. The blue part is the EEG. The prepossessing of EEG can be carried out in EEGLAB (a Matlab toolbox). The red part is the fMRI part. The prepossessing of fMRI can be carried out in fMRIB (a Matlab toolbox). The black and green parts are related to building a GMM. This is the core of our method. The Gaussian mixture model can be clearly shown in Figure 4.2, and the more detail will be introduced in section 6.1. The blue part is the same as the blue part in Figure 3.2, this part is EEG prepossessing; the orange part is the same as the red part in Figure 3.2, this part is fMRI prepossessing. Then, we combine the EEG dataset and fMRI dataset to build a Gaussian mixture model (GMM). This process needs to use PCA to reduce the dimensionality of the data and also keep the most important information from the EEG and fMRI data. Then, we choose the appropriate number of clusters, and apply the expectation maximization (EM) algorithm to evaluate the values of the GMM parameters. This is the green part in Figure 4.2. After that, the GMM is built.

The fMRI dataset only needs to be processed once to build the GMM; after the GMM model is built we only need to update the input EEG data. We assume the size of EEG dataset is same; finally, we carry out a joint EEG and fMRI algorithm by using training GMM instead of fMRI data. Joint EEG and simulated fMRI data from the GMM model is shown in Figure 4.3. We update

the new EEG data as input into the GMM (which is already built in Figure 4.2) to create generated artificial fMRI data from the GMM model and then use it in the BSS algorithm.

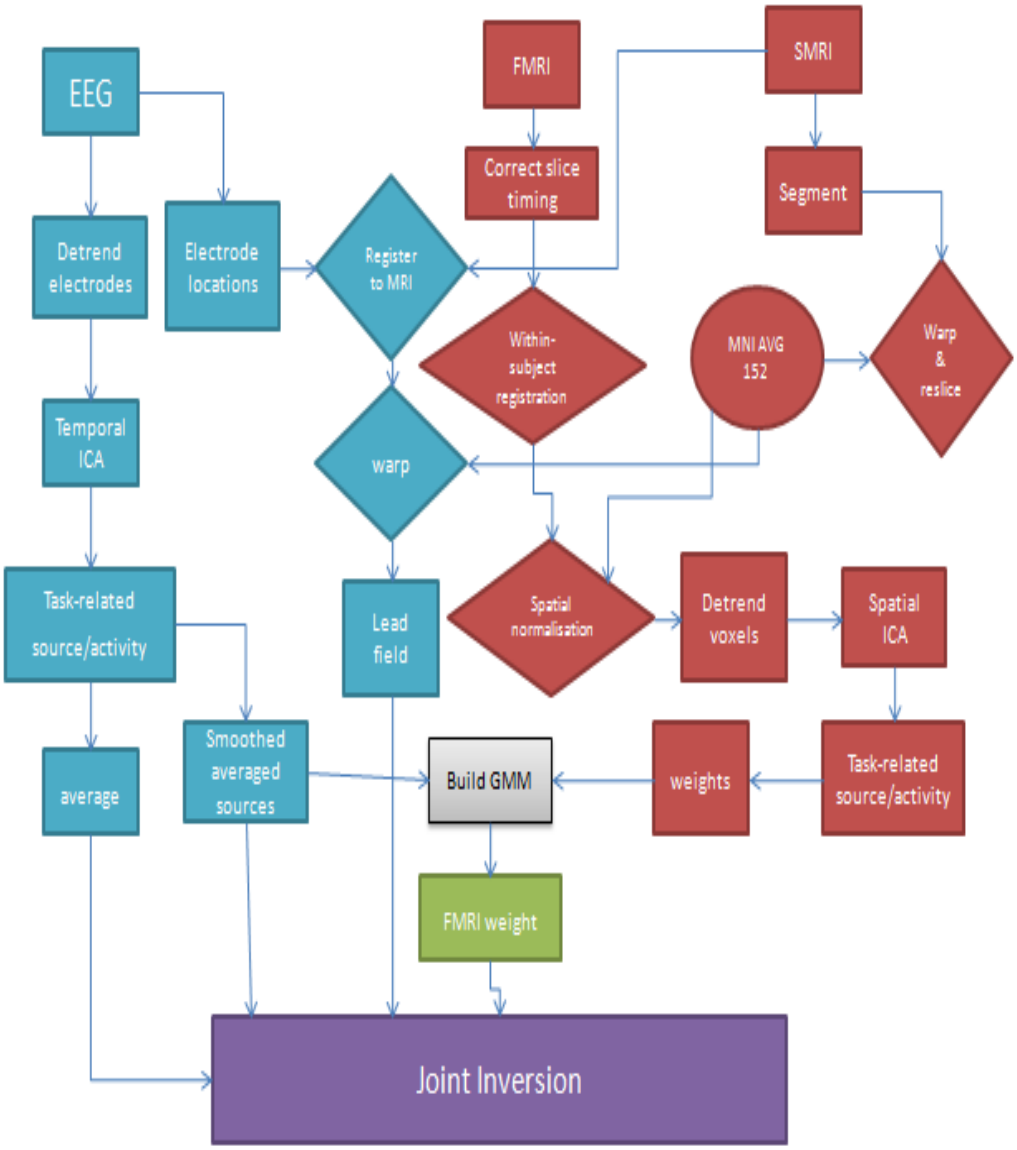

Figure 4.1 Flow chart of joint EEG-fMRI with the GMM model

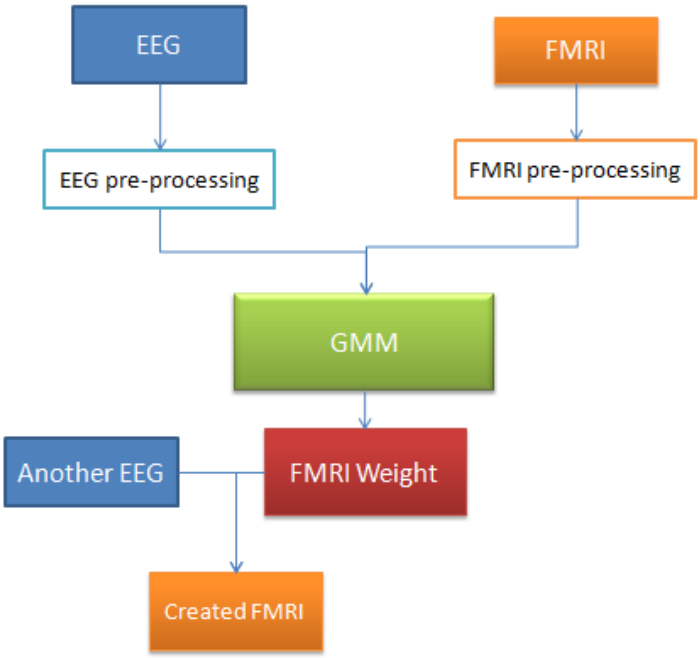

Figure 4.2 Flow chart of GMM model and created fMRI data

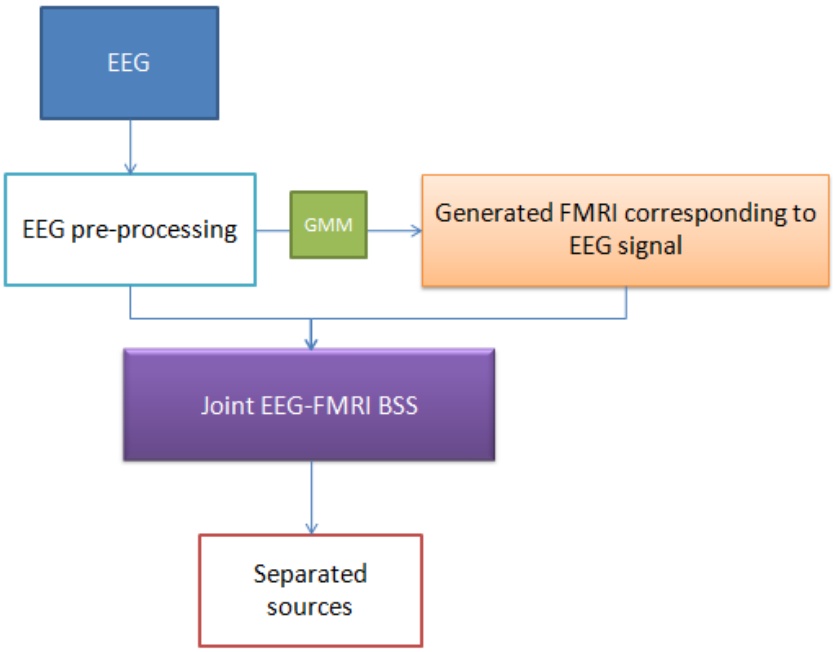

Figure 4.3 Flow chart of the joint EEG-simulated fMRI by using the GMM model

4.2 EEG source localisation

Localisation of brain sources is essential to many research areas such as neuroscience and studies of epilepsy. Neural brain sources localisation based on EEG uses potential data to infer the location of underlying neural activity. EEG source localisation uses the forward and inverse models. The forward model solves the observed matrix (X in equation (3.16)) and the inverse model estimates the source signal of the neuron system.

4.2.1 Lead field matrix

The lead field matrix defines a projection from current sources at discrete locations to current sources at discrete recording sites on the scalp. This is necessary for the cost function of the ICA algorithm in this project; it is the **L** of equation (3.16). As such, the lead field matrix can be used to solve the forward problem **[37]**.

Source localisation on a single sphere model of the head is more popular due to its high computational efficiency and relative accuracy; whereas on a realistic model it remains slow **[39]**. The conductors of the skull, the soft tissue and the scalp, are different. Three sphere shells model assumes that head consists of three concentric homogeneous sphere shells.

When the EEG is measured, the distribution of the electromagnetic field in the head can be defined as a linear Poisson equation (4.1) **[39]**, with a no-flux Neumann boundary condition on the scalp, as in equation (3.27) **[39]**.

$$\nabla \cdot (\sigma \nabla \emptyset) = \nabla \cdot \mathbf{J_S} \tag{4.1}$$

$$\sigma(\nabla \emptyset) \cdot \mathbf{n} = \mathbf{0} \tag{4.2}$$

Where σ denotes electrical conductivity scalar, $\emptyset$ is the electrical potential and $\mathbf{J_S}$ represents electrical current sources, while $\mathbf{n}$ is the noise of the system.

The resistivity of the scalp is 2.22 Ωm; the resistivity of the skull is 177Ωm; and the resistivity of the brain is 2.22Ωm **[33]**. The conductivity of the skull is much lower than the conductivity of the scalp and brain. Therefore, the conductor of the head uses a three-shell concentric spherical head model instead of the homogeneous sphere. The inner sphere represents the brain, the middle sphere is the skull and the outer sphere represents the scalp. The three-shell head model is shown in Figure 4.4, and the electrical potential at point p1 ($\emptyset_{\mathbf{p1}}$) for the proposed dipole can be defined as equation (4.3) **[15].**

$$\emptyset_{\mathbf{p1}} = \frac{1}{4\pi S_r R^2}\sum_{i=1}^{\infty}\frac{X_r(2i+1)^3}{g_i(i+1)i}b^{i-1}[id_z P_i(\cos\theta) + d_x P_i^1(\cos\theta)] \quad (4.3)$$

Where g_i is given in equation (4.4).

$$g_i = [(i+1)X_r + i]\left(\frac{iX_r}{i+1}\right) + (1-X_r)[(i+1)X_r + i]\left(f_1^{i_1} - f_2^{i_1}\right) - i(1-X_r)^2\left(f_1/f_2\right)^{i_1} \quad (4.4)$$

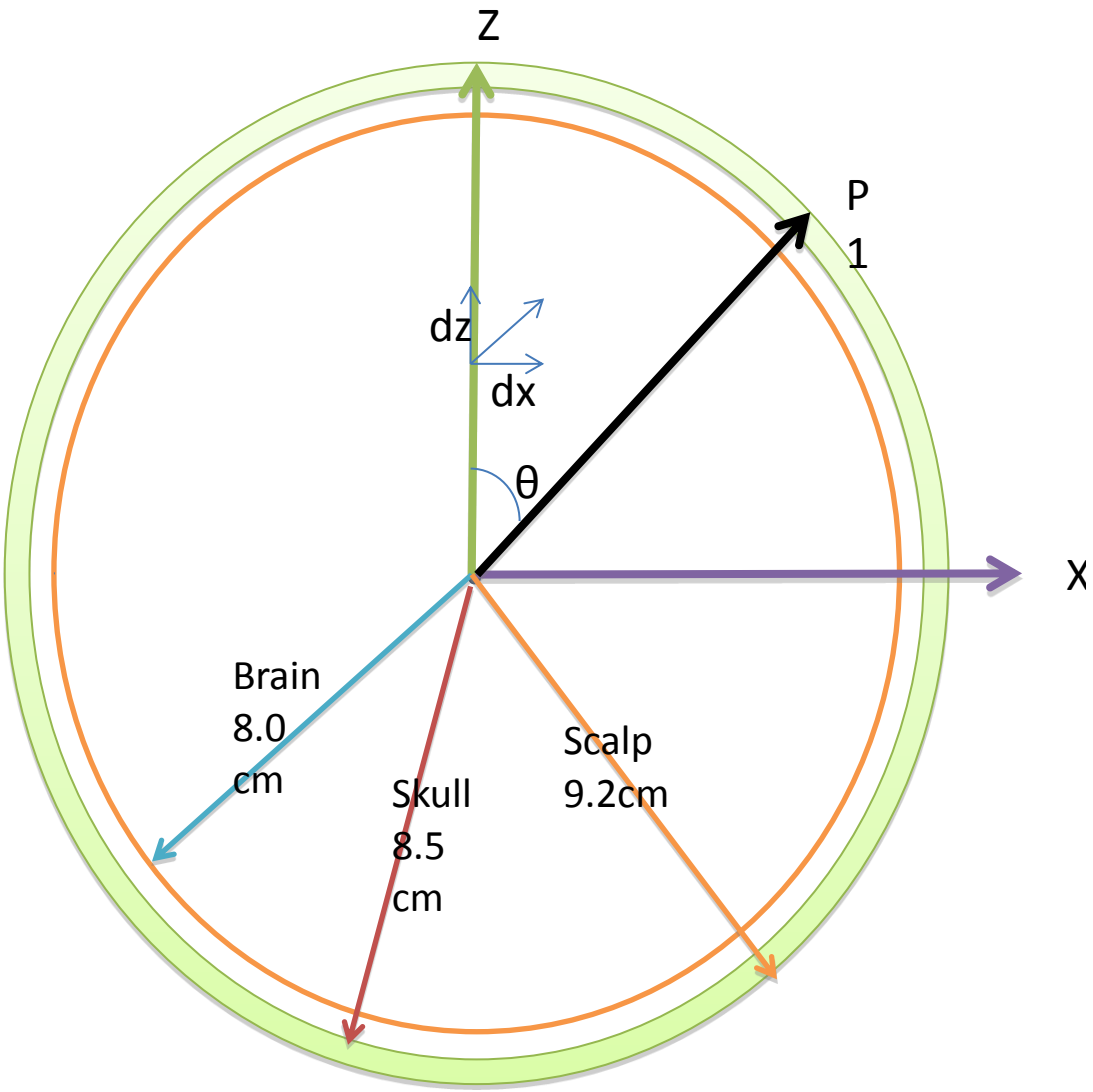

Figure 4.4 The three-shell spherical head model

The component orthogonal to the *xz* plane belongs to zero potential and makes no contribution to the scalp point p1. From the equation (4.3), d_z denotes the radial component of *xz* plane; d_x denotes the tangential component; R is the radius of the outer shell (scalp, 9.2 cm); S_r represents the conductivity of scalp and brain; X_r denotes the ratio between the skull and the scalp; b is the relative distance of dipole from centre; θ denotes the polar angle of the surface point, i is an index start from 1 and end to infinite; i_1 is equal $2i$+1, f_1 denotes the ratio between inner shell radius and the outer shell radius; f_2 represents the ratio between middle shell radius and the outer shell radius; $P_i(\cdot)$ is the Legendre polynomial; and $P_i^1(\cdot)$ denotes the associated Legendre polynomial.

There are several numerical methods for accurately calculating the lead field matrix on a realistic head model, such as the boundary element method (BEM), the finite element method (FEM) and the finite difference method FDM **[15] [37]**.

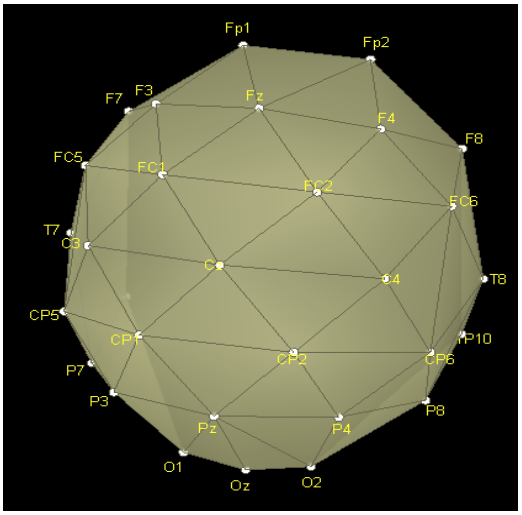

Figure 4.5 30 electrodes name graph

In practice, there are some Matlab toolboxes that can be used to calculate the lead field matrix, such as Brainstorm and Fieldtrip. This project uses Brainstorm to calculate the lead field matrix. The two dimensions of the 30 electrodes in the head model graph are illustrated in Figure 4.5, and the three-dimension electrodes head model graph is shown in Figure 4.6.

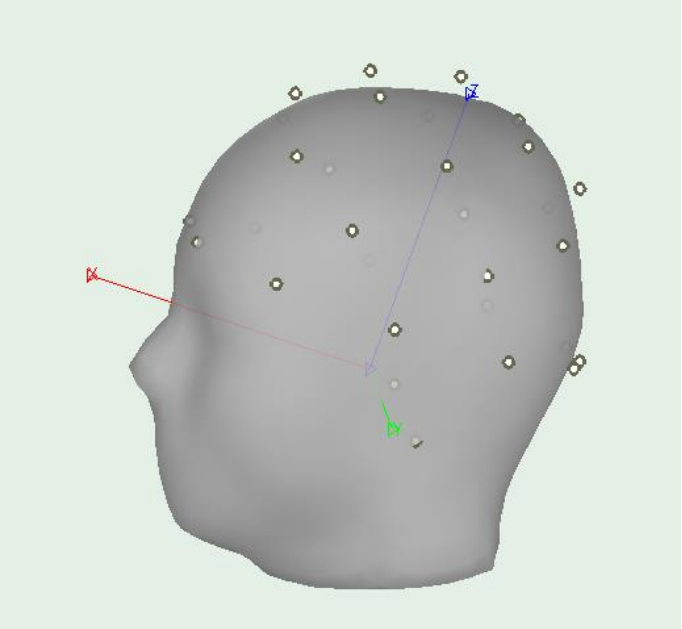

Figure 4.6 3D head and electrode

Different people could have different head sizes; thus, it can be difficult to obtain the radius and the centre of the sphere. In this work, for simplicity we use the default radius (94.96mm) and centre position (2.03, 1.11, 53.41), which was offered by Brainstorm. Selecting the three shell sphere model and calculate lead field matrix, it is very easy to extract the lead field matrix from the mat file headmodel_surf_eeg_3sphereberg. It can be read that the size of the lead field matrix is 30 times 45,084. The Brainstorm simulated graph is shown in Figure 4.7.

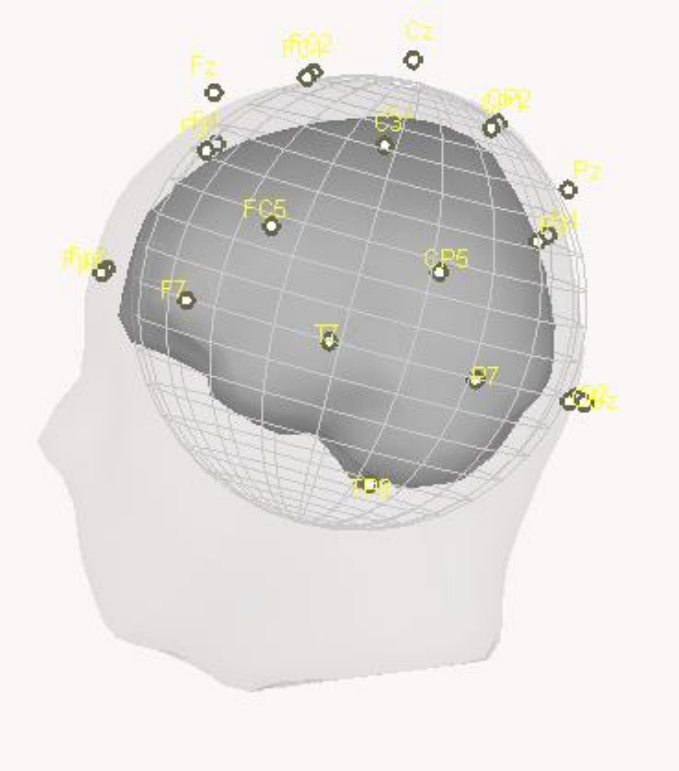

Figure 4.7 3D simulated brain graph

Due to the size of the lead field gain matrix being 30 times 45,084, Brainstorm uses the 3D data; therefore, the 15,028 sources after three shells algorithm can be found. Therefore, the source matrix size is 15,028 times 1500; and the observation matrix is 30 times 1500.

4.2.2 EEG source localisation

Neural activity starts from the link between the dendrite and postsynaptic, with the neuron membrane at its resting potential before the ion flows into the dendrite. The current of ion flows into the dendrite and denotes primary current $\boldsymbol{J_P}$ while ion flows leave dendrite in a very short distance (around 0.1mm). The ion flows around the neural cell affected by the primary current is called volume current $\boldsymbol{J_V}$. The ion flows satisfy the ohm's law, which is illustrated in equation (4.5), while $\boldsymbol{E}$ denotes the electrical field.

$$\boldsymbol{J_V} = \sigma \cdot \boldsymbol{E} \tag{4.5}$$

The total current $\boldsymbol{J}$ is the sum of primary and volume current, as shown in equation (4.6)

$$\boldsymbol{J} = \boldsymbol{J_P} + \boldsymbol{J_V} \tag{4.6}$$

Primary current decays exponentially (e^{-d}, d is approximately 0.1mm) when the ion flow was far away from the postsynaptic. Compared with the distance between neural and electrode on the scalp, the distance of ion flow in the dendrite is much too small, so it can be ignored. Therefore, the primary current can be considered as the point current source. The current dipole $\boldsymbol{Q}$ can be defined as the primary current $\boldsymbol{J_P}$ for both the amplitude and the orient of the point in the space, and is illustrated in equation (4.7)

$$\boldsymbol{J_P}(\boldsymbol{r}) = \boldsymbol{Q}\delta(\boldsymbol{r} - \boldsymbol{r_Q}) \tag{4.7}$$

The vector $\boldsymbol{r}$ denotes the position vector; the vector $\boldsymbol{r_Q}$ is the position of the current dipole $\boldsymbol{Q}$. The current dipole $\boldsymbol{Q}$ is similar to the current dipole moment, and the unit of current dipole $\boldsymbol{Q}$ is A·m.

The electrical potential of the dipole can be defined as equation (4.8). We assume that the distance between the potential point and the dipole is much longer than the length of the dipole. The number q is the charge of the dipole; the number d_p denotes the length of the dipoles. The value of vacuum permittivity ε_0 is 8.854 pF/m. The angle θ is the angle between the dipole and potential point.

$$\phi(d) = \frac{q d_p \cos\theta}{4\pi\varepsilon_0 d^2} \tag{4.8}$$

The distance between the source *R* and the scalp electrode *i* can be described as equation (4.9); the vector $\boldsymbol{f_k}$ is the location of the k-th source; the vector $\boldsymbol{\alpha_j}$ is the location of the j-th scalp electrode and d_{kj} is the distance between the k-th source and j-th scalp electrode **[33]**.

$$\left\|\boldsymbol{f_k} - \boldsymbol{\alpha_j}\right\|_2 = d_{kj} \tag{4.9}$$

The correlation of the source and the electrode is nonlinear; the magnitude of the source attenuates with $1/d_{kj}^2$, as shown in equation (4.10) **[34]**

$$Cor(\boldsymbol{X}, \boldsymbol{s_k}) = \langle \boldsymbol{X}, \boldsymbol{s_k} \rangle = \boldsymbol{LS} \cdot \boldsymbol{s_k} \tag{4.10}$$

After the correlation is calculated, the distance d_j can be computed as equation (4.11) **[35]**

$$d_{kj} = \frac{1}{\sqrt{Cor(\boldsymbol{X}, \boldsymbol{s_k})}} \tag{4.11}$$

For source localisation, in equations (4.9), (4.10) and (4.11) only $\boldsymbol{f_k}$ is unknown, and if the problem coverts to the mathematic problem it can be calculated by Gaussian elimination **[8].** We need to calculate the vector $\boldsymbol{f_k}$ in equation (3.34), while equation (4.12) is expanded from equation (4.9)

$$\boldsymbol{f_k^T f_k} - 2\boldsymbol{\alpha_j^T f_k} + \boldsymbol{\alpha_j^T \alpha_j} = d_{kj}^2 \tag{4.12}$$

Rewrite equation (4.12) as equation (4.13), where $r = \boldsymbol{f_k^T f_k}$ and $b_j = \boldsymbol{\alpha_j^T \alpha_j} - d_{kj}^2$

$$\boldsymbol{\alpha_j^T f_k} = {(r + b_j)}/{2} \tag{4.13}$$

For the matrix form, equation (4.13) can be rewritten as equation (4.14), the vector $\boldsymbol{u}$ is shown as equation (4.16) and the vector $\boldsymbol{v}$ is shown as equation (4.17). The vector $\boldsymbol{e}$ is the unit vector.

$$\boldsymbol{A^T f_k} = (r\boldsymbol{e} + \boldsymbol{b})/2 \tag{4.14}$$

$$\boldsymbol{f_k} = (r\boldsymbol{u} + \boldsymbol{v})/2 \tag{4.15}$$

$$\boldsymbol{u} = \boldsymbol{A^{-T} e} \tag{4.16}$$

$$\boldsymbol{v} = \boldsymbol{A^{-T} b} \tag{4.17}$$

Therefore, $r = \boldsymbol{f_k^T f_k} = \frac{1}{4}(r\boldsymbol{u} + \boldsymbol{v})^{\boldsymbol{T}}(r\boldsymbol{u} + \boldsymbol{v})$ equals equation (4.18), which is the quadratic equation, with the solution as equation (4.19). Finally, we combine equations (4.15), (4.16) and (4.17) to give the position of the source $\boldsymbol{f_k}$.

$$(\boldsymbol{u^T u})r^2 + (2\boldsymbol{u^T v} - 4)r + \boldsymbol{v^T v} = 0 \tag{4.18}$$

$$r = \frac{2 - \boldsymbol{u^T v} \pm \sqrt{(2 - \boldsymbol{u^T v})^2 - (\boldsymbol{u^T u})(\boldsymbol{v^T v})}}{\boldsymbol{u^T u}} \tag{4.19}$$

Following the above procedure, we obtain the position of the source. This process is known as EEG source localisation. The principle of this process is based on the theory of electrical potentials, and we assume that the brain signals are created as point's electrical sources. As such, accurate source localisation is useful for diagnosing brain diseases.

5. Experiment Modelling

In this chapter, we simulate a number of neural sources, corresponding to EEG data and fMRI data. We simulate neural activity first, and then the EEG and fMRI data used in an ICA algorithm in order to obtain the original neural activity. Finally, we compare the neural sources activity obtained by the algorithm to the original simulated neural sources. Simulated data is the most important section for testing the algorithm; this is because EEG signal separation is one of the classic blind source separation applications. If we only use the real EEG data for separation, it would be difficult to judge the algorithm on how well it separates and localises the sources, as no such information would be available. Therefore, using the simulated data is our best way to assess the quality of our algorithm.

5.1 Simulated EEG data

To simulate EEG data, the first thing we need to do is to calculate the lead field matrix using the Brainstorm Matlab toolbox, which was mentioned in section 3.3. The neural activity form can be supposed as an impulse, a sinusoid signal, or an event-related potential (ERP) damped sinusoid signal **[31].** In this chapter, we follow **[31]** and assume that the neural activity is the damped sinusoid signal. The form of neural activity can be shown as equation (5.1) **[5]**.

$$z(t) = \alpha e^{-bt}\sin(\beta\delta t) \tag{5.1}$$

Parameters α, β and δ are randomly created from the following ranges in the same order of appearance:（0，80), （1.7，10), （1，25). Each channel of the signal can be generated by different parameters. The simulated source matrix was made up from each channel and synthetic EEG data was created by multiplying the source $\boldsymbol{Z(t)}$ by the lead field matrix **L [31]**. Synthetic EEG data is estimated using equation (5.2).

$$\boldsymbol{S_{SyntheticEEG}(t) = L\,Z(t)} \quad (5.2)$$

The noise could also be added to the simulated EEG data; the synthetic EEG data with noise can be described as equation (5.3). **N** denotes the noise, as it can be considered as 10% of maximum value of the synthetic data **[5]**. It also can be considered as Gaussian white noise **[5]**.

$$\boldsymbol{S_{SyntheticEEG}(t) = L\,Z(t)} + \mathbf{N} \quad (5.3)$$

5.2 Simulated fMRI data

To simulate fMRI data, the first thing is to introduce the hemodynamic response function (hrf). The blood oxygen level dependent (BOLD) response is a measurement of the brain's metabolic rate and also indirectly explores the neural activity, which has the form of an impulse, a sinusoid or damped sinusoid. In this article the neural activity uses the form of a damped sinusoid signal **[31]**.

Friston proposed that the hemodynamic response function derived from neuronal activity was based on the Balloon/Windkessel model **[8]**. Robinson et al. gave the specific form of hemodynamic response function as in equation (5.4) **[31]**.

$$hrf(t) = A_1 e^{-t/\tau} - B_1 e^{-t/\alpha\tau} + e^{-kt/2}[C_1 \sin(\omega_0 t) - D_1 \cos(\omega_0 t)] \qquad (5.4)$$

where $\omega_0 = \sqrt{\gamma - k^2/4}$, and constants A_1, B_1, C_1 and D_1 are given by equations (5.5), (5.6), (5.7) and (5.8)

$$A_1 = V_0 \frac{(1-\beta)(k_1+k_2)\tau}{1-k\tau+\tau^2\gamma} \qquad (5.5)$$

$$B_1 = V_0 \frac{\alpha^2(k_1-k_3)\tau}{1-\alpha k\tau+\alpha^2\tau^2\gamma} \qquad (5.6)$$

$$C_1 = \frac{1}{2\tau\omega_0} A_1(2-k\tau) - B_1 \frac{(2-\alpha k\tau)}{\alpha} \qquad (5.7)$$

$$D_1 = A - B \qquad (5.8)$$

where k is the rate of signal decay and the value is 0.65 s^{-1}, γ denotes flow-dependent elimination constant and the value is 0.41 s^{-1}. τ is the hemodynamic transit time and value is 0.98 s, α is Grubb's exponent and the value is 0.32, while V_0 denotes resting blood volume fraction and the value is 0.02. ρ is the resting oxygen extraction fraction and the value is 0.34, k_1, k_2 and k_3 are BOLD response coefficients and corresponding values are 7ρ, 1.43ρ and 0.43 and $\beta = \frac{\rho+(1-\rho)\ln(1-\rho)}{\rho}$. After calculation, A_1=0.06, B_1=0.047,

C_1=0.051, D_1=0.055 and ω_0 =0.055 s^{-1}. The hemodynamic response function is shown in Figure 5.1.

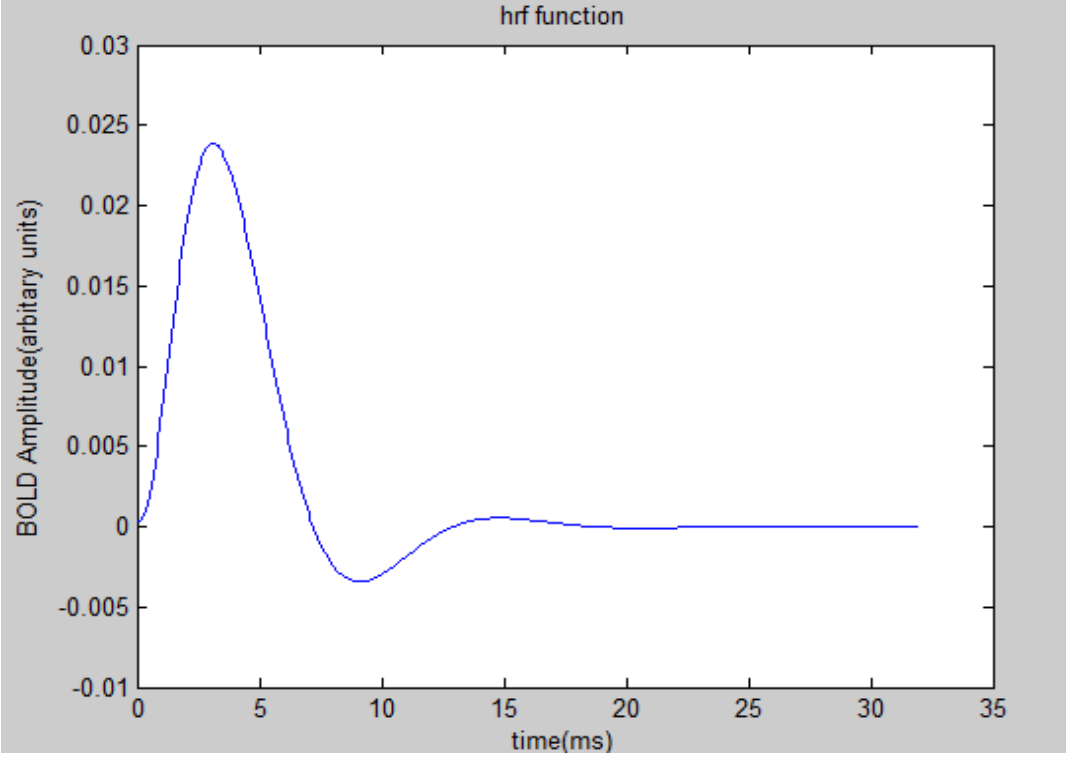

Figure 5.1 Hemodynamic response function diagram

FMRI simulation is based on the convolution between the neuronal activity source $\boldsymbol{z}(t)$ and hemodynamic response function $\boldsymbol{hrf}(t)$ mentioned already, whereby the form of simulated fMRI data is shown in equation (5.9). Similarly, the noise also can be considered in the fMRI data. The simulated fMRI data with noise is shown in equation (5.10).

$$\boldsymbol{S_{SyntheticfMRI}}(t)=\boldsymbol{z}(t) * \boldsymbol{hrf}(t) \tag{5.9}$$

$$\boldsymbol{S_{SyntheticfMRI}}(\boldsymbol{t})=\boldsymbol{z}(t) * \boldsymbol{hrf}(t) + \boldsymbol{N} \tag{5.10}$$

EEG simulation is based on the head model, which we use to multiply with the simulated neural source signal, whereas fMRI simulation is based on the convolution of hemodynamic response function (HRF) with a simulated neural source signal **[23]**. The simulated fMRI data is shown in Figure 5.2. First subplot is the hemodynamic response function, second subplot is the damped sinusoid

signal and the last subplot is the simulated fMRI signal. The diagram of simulated data is shown in Figure 5.3. From this diagram, we can see clearly that the synthetic EEG is where the neural activities multiply the lead field matrix whereas the synthetic fMRI is the convolution of the neural activities and the hemodynamic response function.

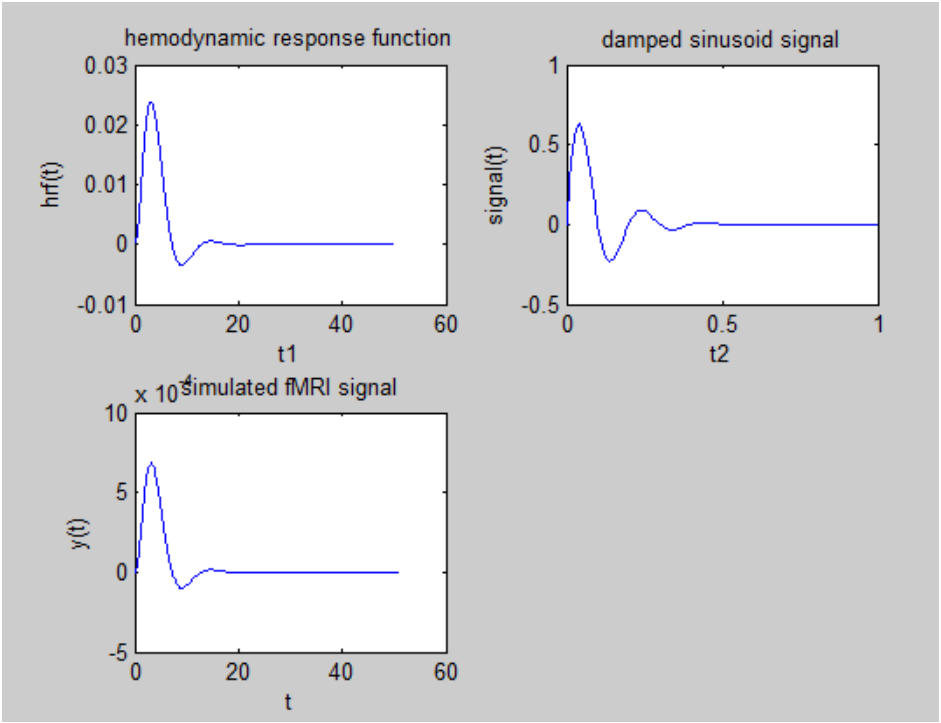

Figure 5.2 Simulated fMRI data figure

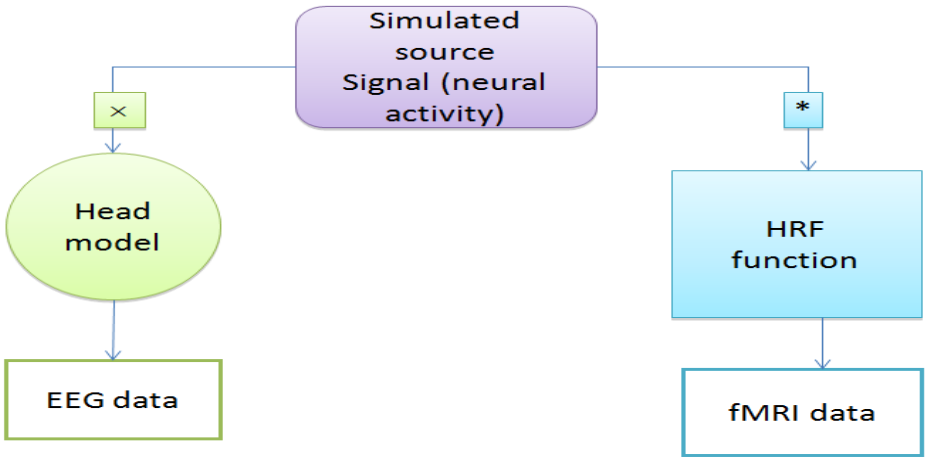

Figure 5.3 Diagram of simulated EEG and fMRI

5.3 Experiment and results

We started by simulating two neural activities, because it was easy to check the accuracy of the algorithm, and then we extended to the four neural activities. Two neural activities were created based on equation (5.2). Results are shown in Figure 5.4. The horizontal axis is time and the unit is millisecond; the vertical axis is the voltage and the unit is millivolts. The red curve is the first neural activity at the location of the red cross and the green curve is the second neural activity at the location of the green cross in Figure 5.6. The EEG observed signal can be calculated as equation (5.2), while the result of the EEG which corresponds to the two neural activities is shown in Figure 5.5. Each subplot denotes the subcomponent. For each subplot, the horizontal axis is time and the unit is millisecond; the vertical axis is the voltage and the unit is millivolts.

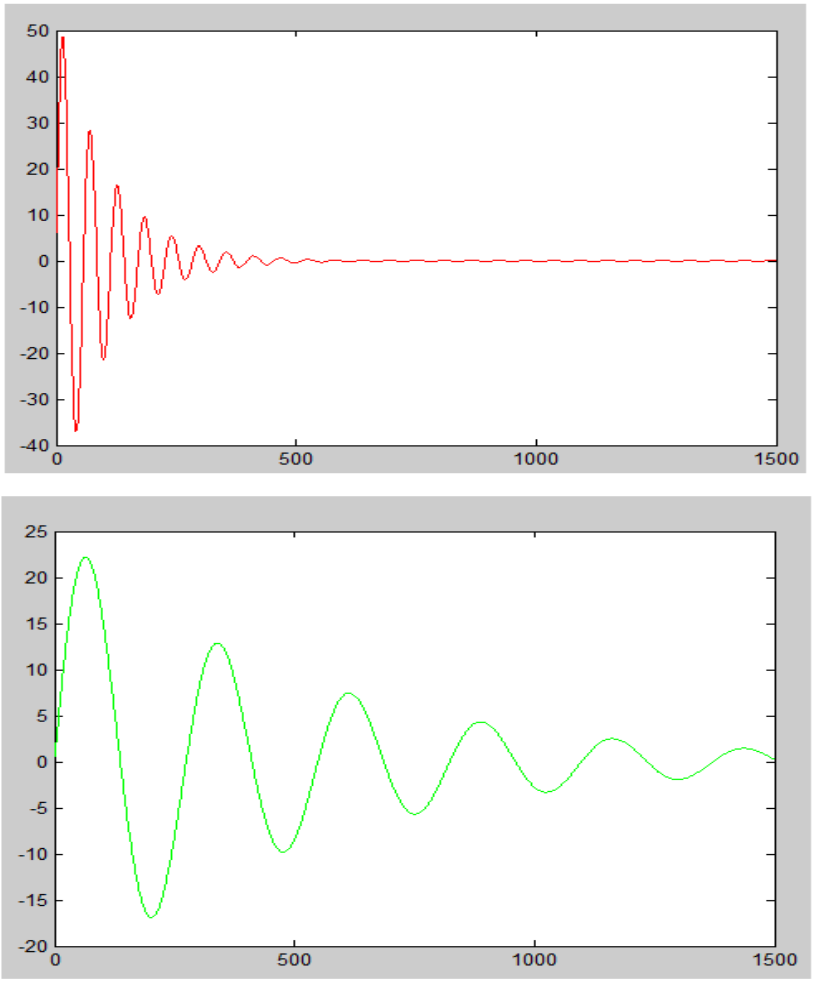

Figure 5.4 Two simulated neural sources

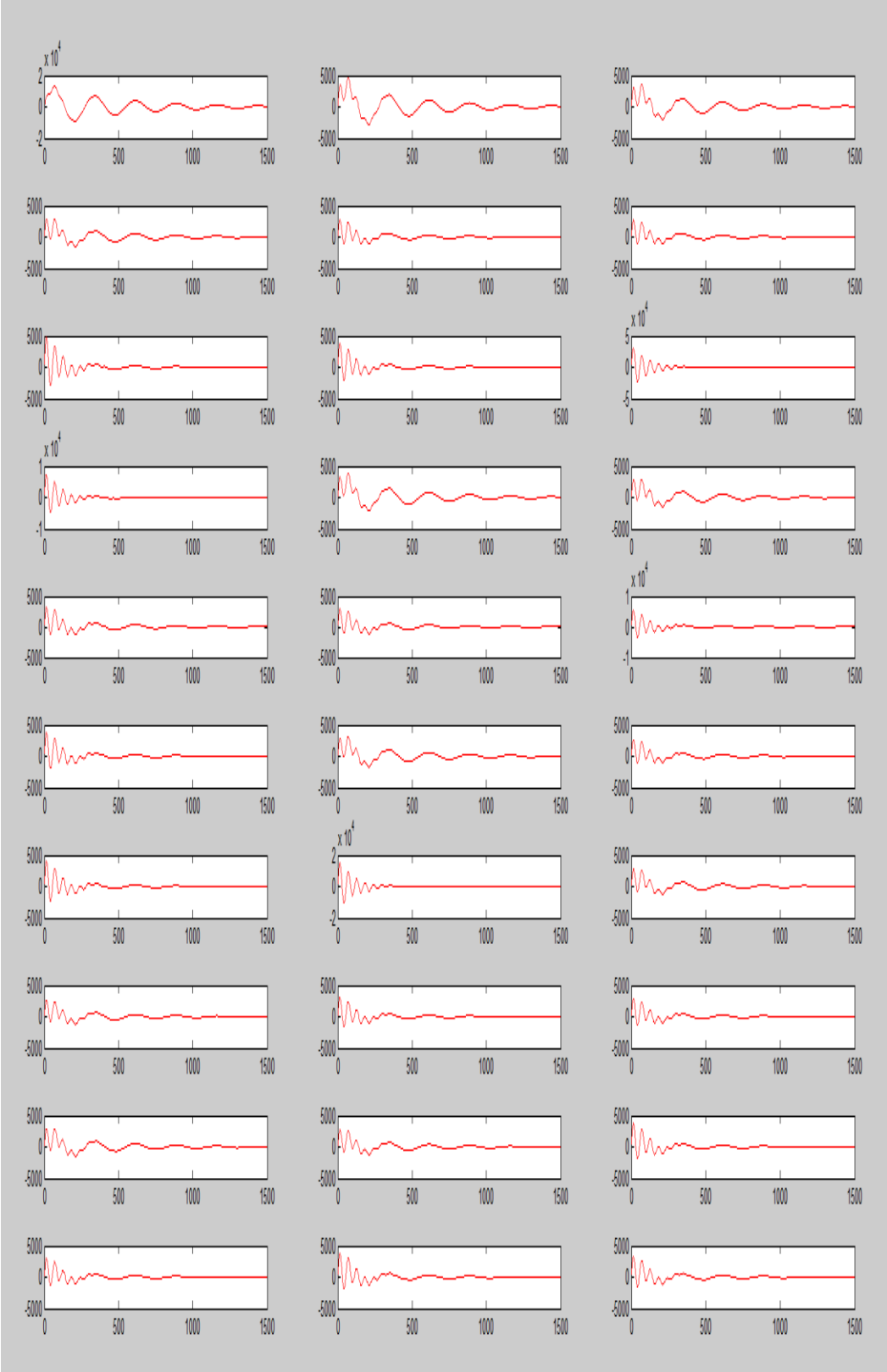

Figure 5.5 Simulated EEG data

The neural source 2D locations can be considered as the red and green crosses in Figure 5.6. In this figure, the blue spots are the neural activities, which are simulated by the head model. Two neural locations are randomly selected; the red is on the left side of the brain and the green is on the right side of the brain because the difference is obvious. We run the minimum norm algorithm (which is discussed in section 3.3) on the EEG, which is shown in Figure 4.5. The estimated source position is shown in Figure 5.7, which is calculated as in section 3.3.2, whereby the '+ 'denotes the original source position and the 'o' denotes the estimated source location. The estimated source is shown in Figure 5.8. The blue curve is the original source and both the green and red colours are two signals estimated by the MN algorithm.

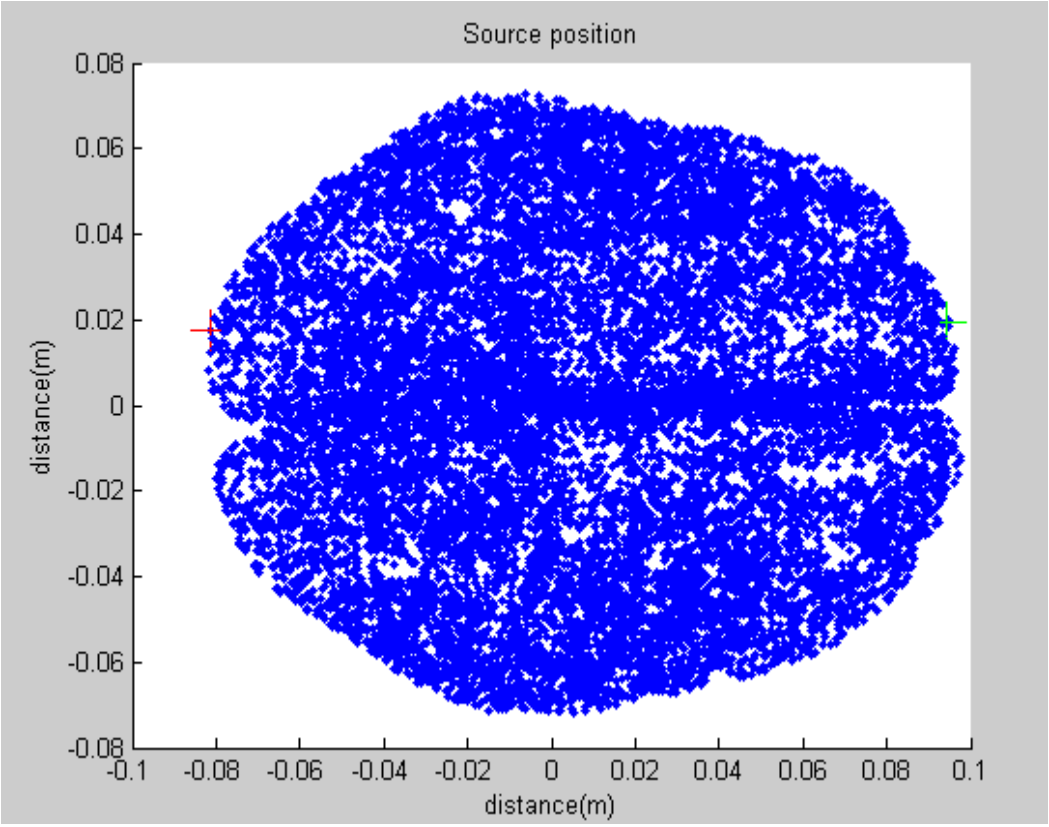

Figure 5.6 The position of two neural sources

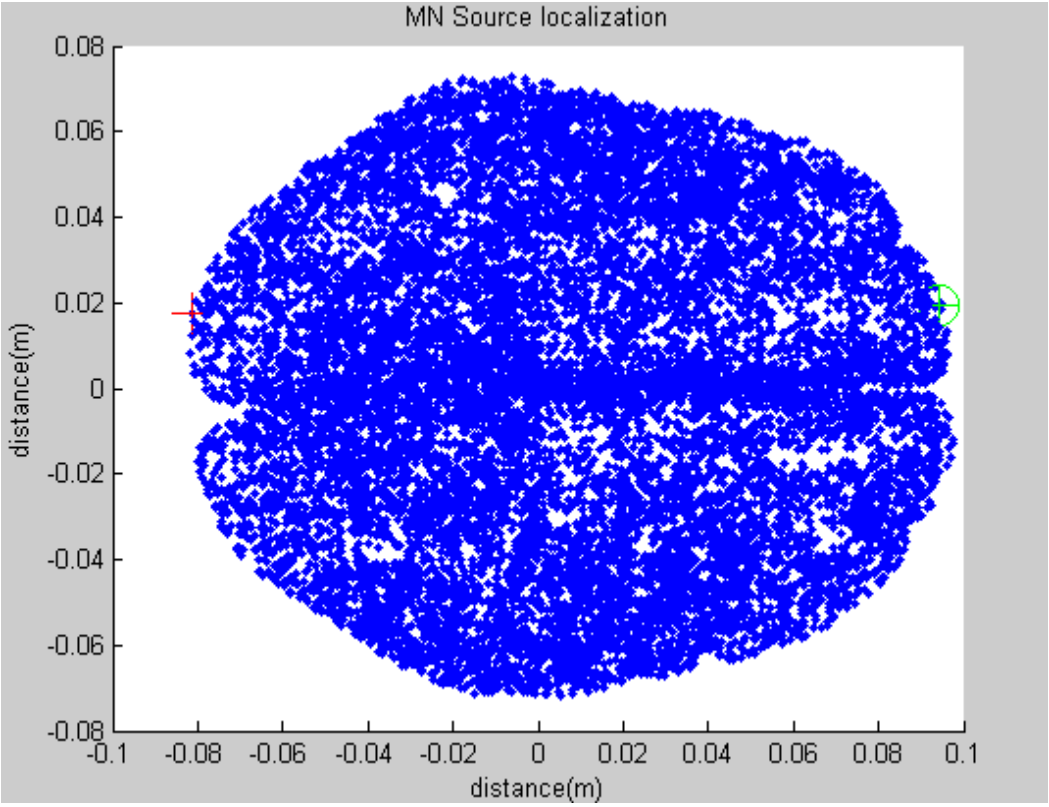

Figure 5.7 MN estimated position of the neural source

In Figure 5.7, the blue dots denote the neural activities and the red cross on the left side is the original neural source 1, but we cannot find the red circle near the red cross, so we cannot localise the source 1. On the right side of Figure 5.7 we can see both the green cross and the circle, and they are in the same location, therefore, we can localise the source 2.

On the first figure of Figure 5.8, this is the source 1 result of the EEG source separation, which is based on the ICA. The blue curve is the original source, and the red curve is the separation result. The peak value of the original source is 48.634 and the peak value of the separation is 17.823. On the second figure of Figure 5.8, this is the source 2 result of EEG source separation, whereby the blue curve is the original source, and red curve is the separation result. The peak value of the original source is 22.220 and the peak value of the separation is 3.478.

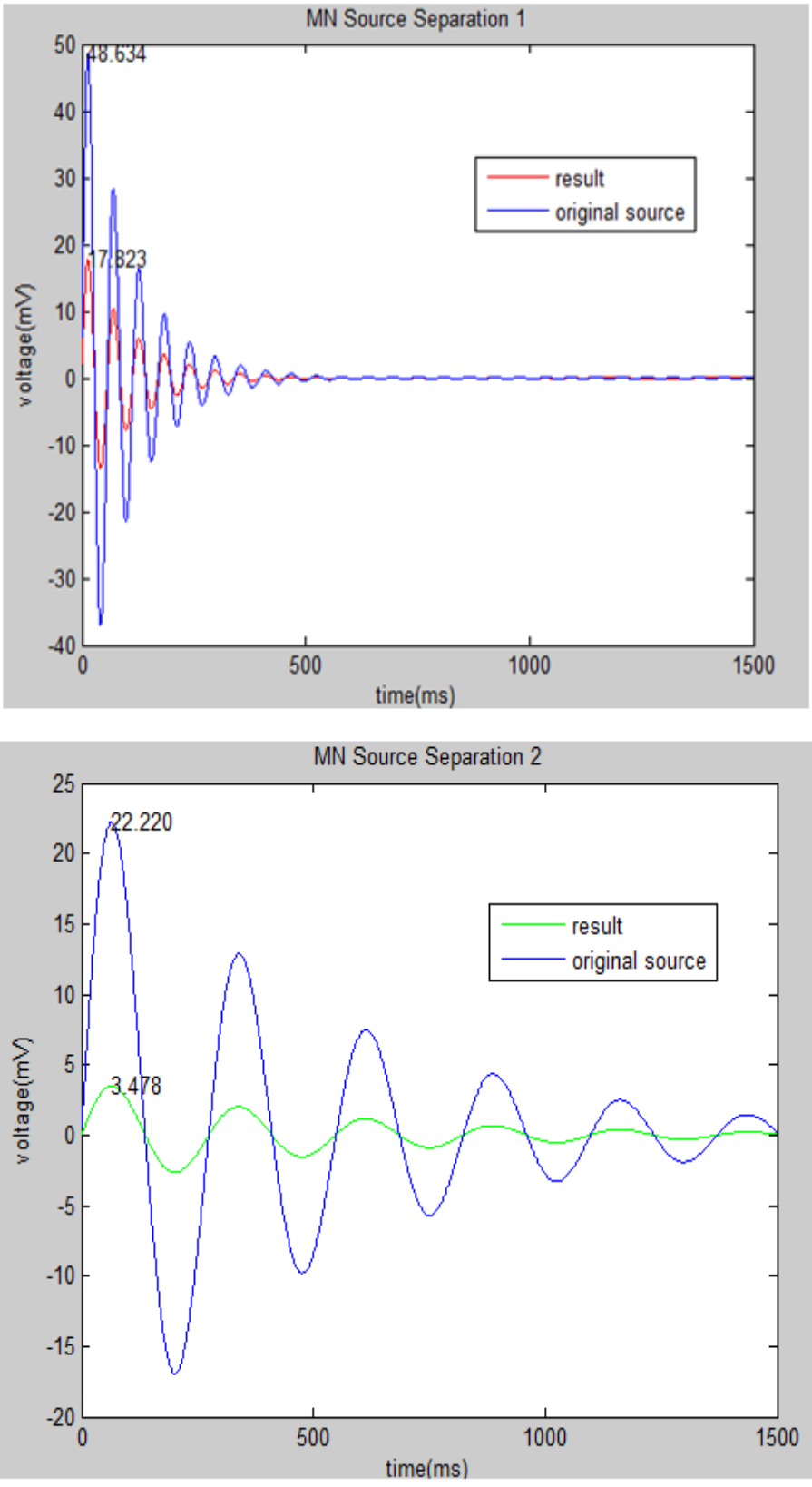

Figure 5.8 MN estimated neural sources signal

The simulated fMRI data is shown in equation (5.9). I then applied the MRJI algorithm, which is discussed in section 3.2.3. The estimated source is shown in Figure 5.9 and the estimated position is shown in Figure 5.10.

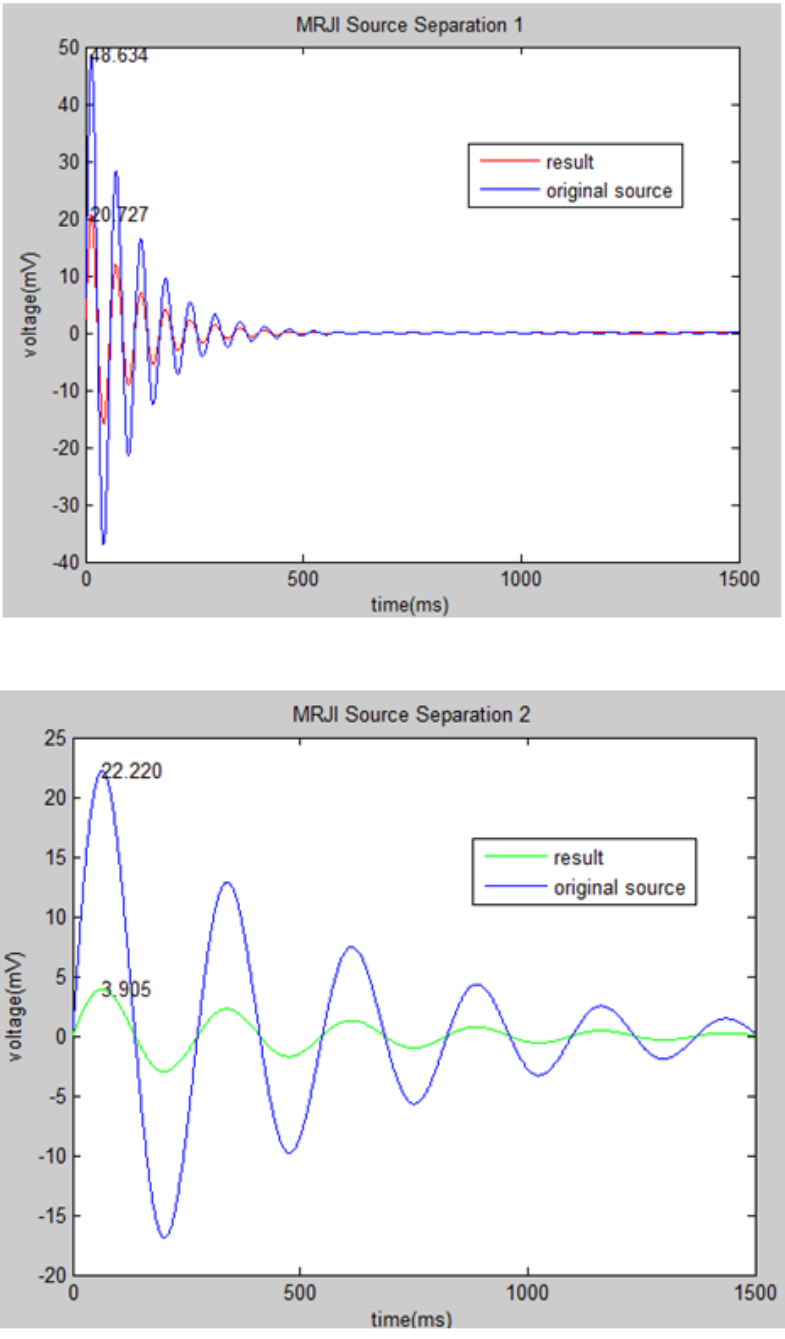

Figure 5.9 MRJI estimated the neural source

On the first figure of Figure 5.9, this is the source 1 result of EEG source separation on joint EEG and fMRI, and the method is MRJI. The blue curve is

the original source, and the red curve is the separation result. The peak value of the original source is 48.634 and the peak value of the separation is 20.727. On the second figure of Figure 5.8, this is the source 2 result of EEG source separation, whereby the blue curve is the original source, and red curve is the separation result. The peak value of the original source is 22.220 and the peak value of the separation is 3.905.

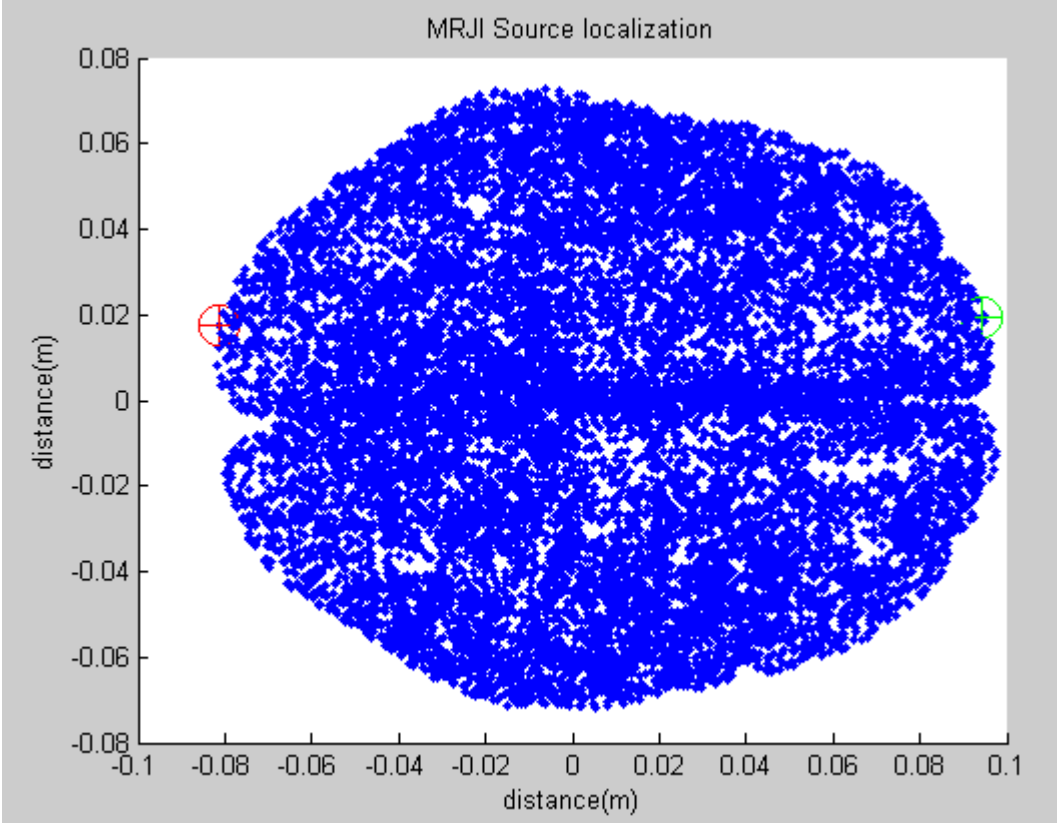

Figure 5.10 MRJI estimated position of the neural source

In Figure 5.10, the blue dots denote the neural activities and the red cross on the left side is the original neural source 1, while in the same place we can see the red circle, which is the localisation result on MRJI. Therefore, we localise the source 1 based on MRJI. On the right side of Figure 5.7, the green cross is the original neural source 2 and, in the same place, we can see the green circle, which is the localisation result on neural source 2. Therefore, we could localise the source 2 based on MRJI.

Compared with Figures 5.8 and 5.9, MRJI can provide more accurate source

separation. The peak value of the estimated source by MRJI is 20.727 for source 1 and 3.905 for source 2. Whereas the peak value of the estimated source by MN is 17.823 for source 1 and 3.905 for source 2. In addition, the correlation of both source and original source are same, both are 1. Therefore, we compare whether the peak value is enough for the result. In Figure 5.7, source 1, which is the red colour source, is lost after the MN algorithm; source 2, which is the green colour source, has the correct localisation. However, both sources (red and green) got the correct localisation in Figure 5.10. Compared with Figures 5.7 and 5.10, the latter is better than the former. Therefore, MRJI can achieve more precision in source localisation than MN.

From this experiment, it is clearly shown that MRJI can give the more accurate results in terms of both separation and localization. We hope that MRJI can also produce better results using a model of correlations between EEG and fMRI as opposed to using joint EEG/fMRI readings. We investigate this hypothesis in the next chapter.

6. Joint EEG/FMRI Model

This chapter introduces the new method for joint EEG and fMRI separation and localisation, which is uses a model of correlations between EEG and fMRI based the Gaussian Mixture Model (GMM). Therefore, we need to introduce the GMM.

GMM is a parametric probability density function *p(x)* represented as a weighted sum of Gaussian component densities.

$$p(x) = \sum_{k=1}^{K} \pi_k N(x; \mu_k, \sum_k) \quad (6.1)$$

where K is the number of clusters which need to be defined, and the scalar π_k is the weight factor; it is the probability of the cluster *k* being selected. The notation μ_k is the mean of the distribution, and $\sum_k$ is the covariance of the distribution. The GMM parameters can be estimated from the real data. In this work, we do not know the sample classification; we need to use an expectation maximisation (EM) algorithm for clustering. We will use GMM in joint EEG-fMRI separation to obtain more accurate results than when we use EEG only, as described in detail later in this chapter.

GMM parameters can be estimated from the real data and obtained simply via underlying processing. In this chapter, we use GMM to represent the correlations between EEG and fMRI data obtained simultaneously during an experiment. We used this GMM in joint EEG-fMRI separation and localisation as it can provide more accurate results than when we use EEG only.

6.1 Experiment on two neural activities

This experiment is based on the two neural activities undertaken for both training and test data. This experiment can be divided into several parts. Firstly, we create GMM from simulated EEG and corresponding fMRI data. Secondly, we create a test EEG sequence. We then generated the artificial fMRI data from the test EEG data and the GMM model from the first step. Then, we ran the EEG-fMRI source separation and localisation with the data from the last step. Finally, we compared the result between joint EEG-fMRI by using the EEG signal only.

6.1.1 Creating the GMM

Firstly, we used the damped sinusoid function for the simulated neural activity. We created two different neural activities in two different locations. We created 1500 samples for this experiment. Then we used the lead field matrix obtained from the Brainstorm Matlab toolbox. After that we obtained the simulated EEG data, by multiplying the lead field matrix with the neural activity **[5]**.

Next, we simulated the hemodynamic function (hrf function) from **[31]**. We can get the simulated fMRI data as a convolution between the hrf function and the neural activities from the last step. We then obtained simulated fMRI, which still has two neural activities with the same location from the last step.

Thirdly, we model joint EEG and fMRI data using principle component analysis (PCA) and GMM. We keep 99% of the data's information. The results are shown in Figure 6.1, with the ten red dots in the figure representing the Gaussian centre. It is shown more clearly in different colours as seen in Figure 6.2. Six coloured crosses '+' represent the six Gaussian centres and the corresponding colour dots represent the distribution; in addition, the four coloured circles 'o' represent the other four Gaussian centres and the corresponding colour stars denote the distribution.

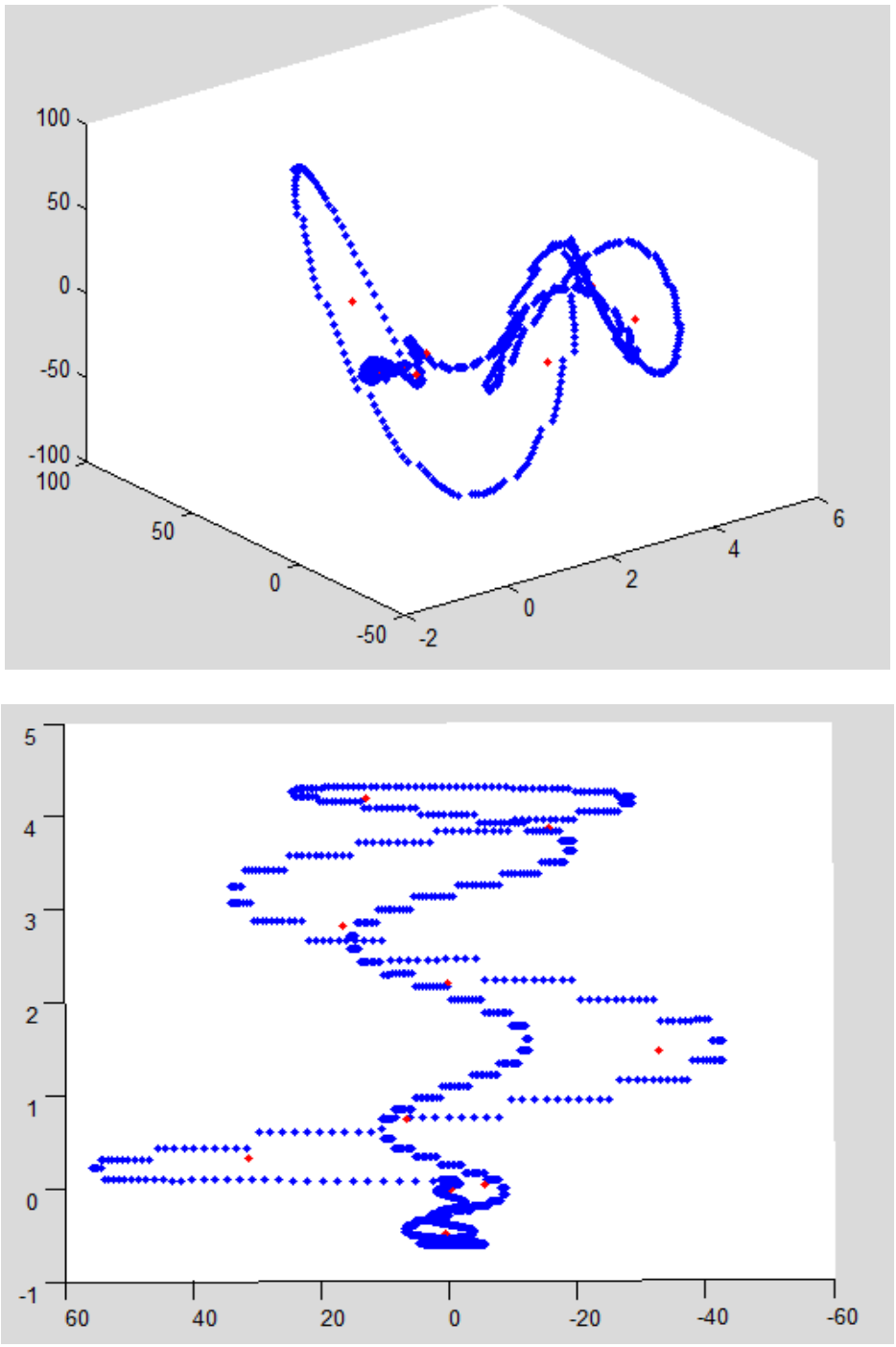

Figure 6.1 Three main principal axes of EEG/fMRI dataset

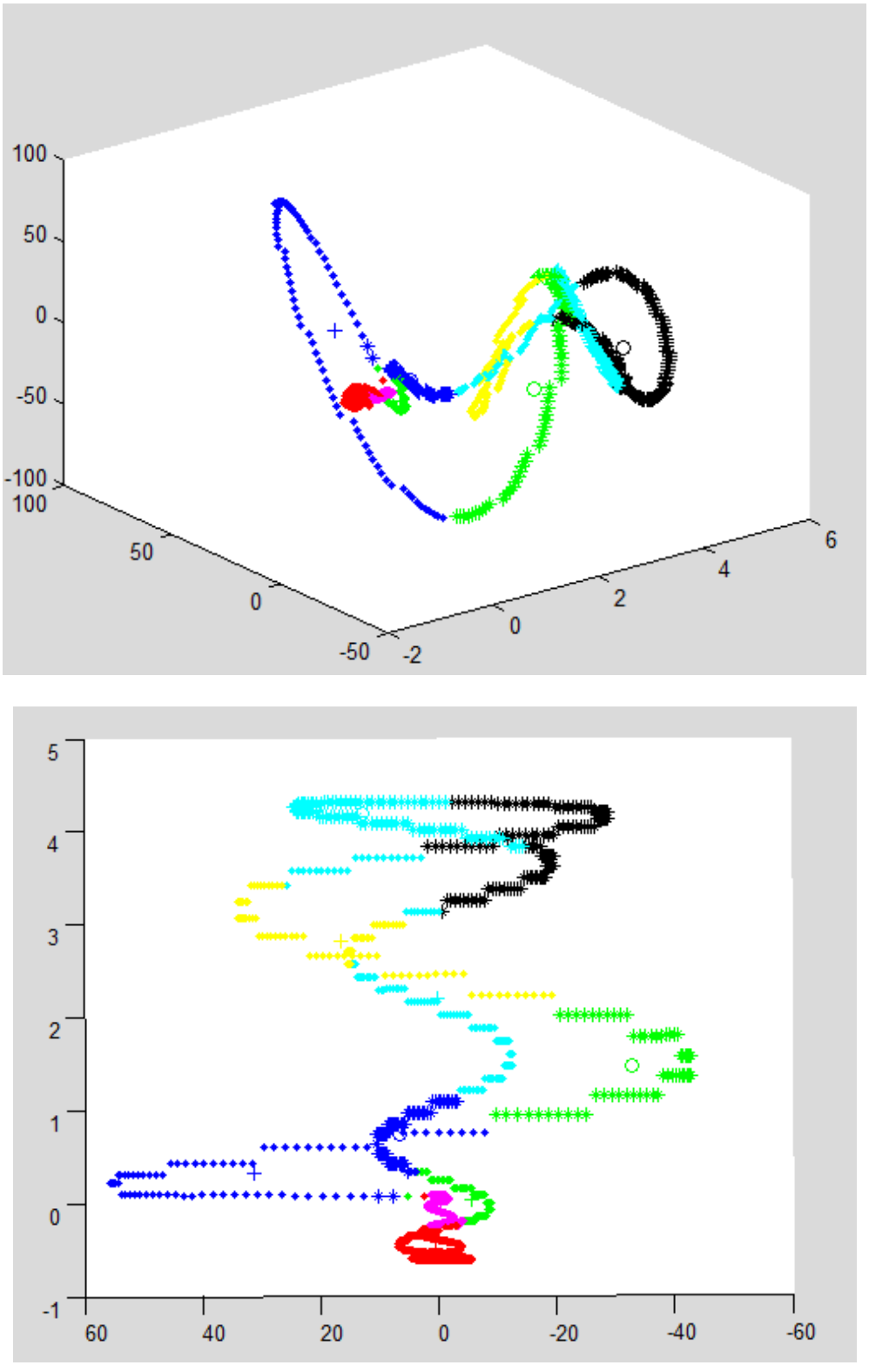

Figure 6.2 Three main principal axes of EEG/fMRI dataset and Gaussian distribution information

6.1.2 Creating the simulated fMRI data

In this step, we create two new neural activities with different amplitude and frequency but in the same location. Then, we created the new simulated EEG data using the lead field matrix as described previously and based on the GMM from the last step. We calculated the Mahalanobis distance of each cluster centre to the projected EEG data in order to estimate the closest fMRI data.

For testing, we created simulated fMRI from the simulated neural sources and the hrf function. This is shown in Figure 6.3. The green line is the simulated fMRI from the hrf function; the red colour point is the estimate fMRI from GMM. It is shown clearly that the red colour has discrete points, but in fact the fMRI should be a continuous line, therefore, smoothing the data is essential.

Next, we need to smooth the result by using curve fitting and the Matlab spline function; this is where the results show several discrete points. It is quite different to the real fMRI data, which has more continuous nature. The simulated fMRI result after curve fitting is shown in Figure 6.4. It is obvious that the green colour is the simulated fMRI based on the hrf function and the red colour is the estimated fMRI from GMM and spline. We compare the red colour dots between Figures 6.3 and 6.4. The result in Figure 6.4 is continuous but the result in Figure 6.3 has some discrete points. Therefore, the simulated fMRI from GMM after spline is better than not through the spline. However, the simulated fMRI from GMM after spline is still not very smooth, it looks like a pause; therefore, we need to clean the data by using a filter.

We built a Gaussian filter to clean the data, because the result is quite rough. Different bandwidth filters could create quite different results. The result of the bandwidth is 40 Hz, which is shown in Figure 6.5, and the filter information is shown in Figure 6.6. The result of the bandwidth is 200 Hz, while the result is shown in Figure 6.7 and the filter information is shown in Figure 6.8. We compare Figures 6.5 and 6.7; it is obvious that the red colour dots in Figure 6.7 are smoother than in Figure 6.5. However, the bandwidth is not huge, so the

result is too flat. Empirically, we chose the Gaussian filter bandwidth of 200 Hz for the experiment.

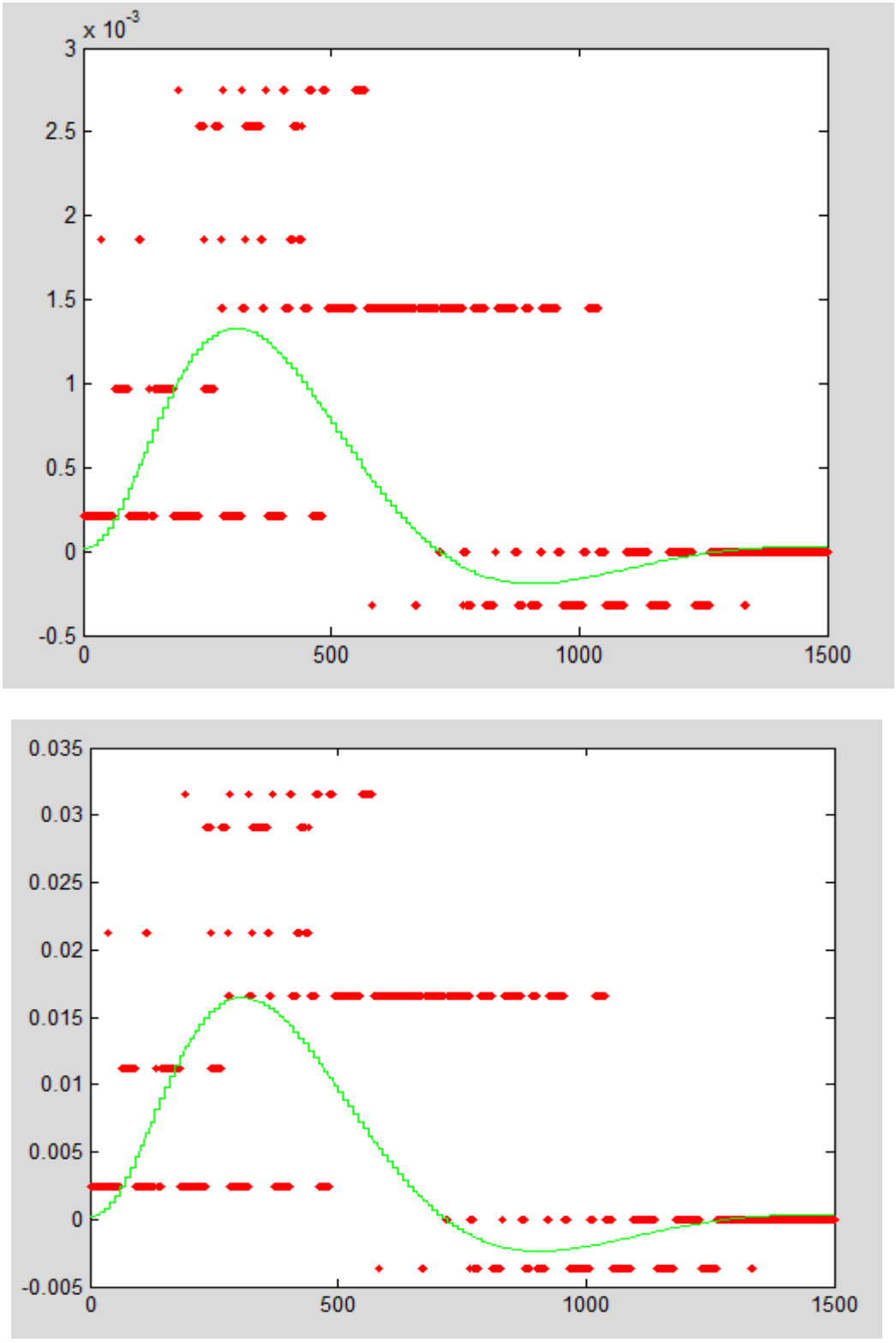

Figure 6.3 Simulated fMRI result (red colour is simulated fMRI from GMM and the green colour is simulated fMRI from hrf function)

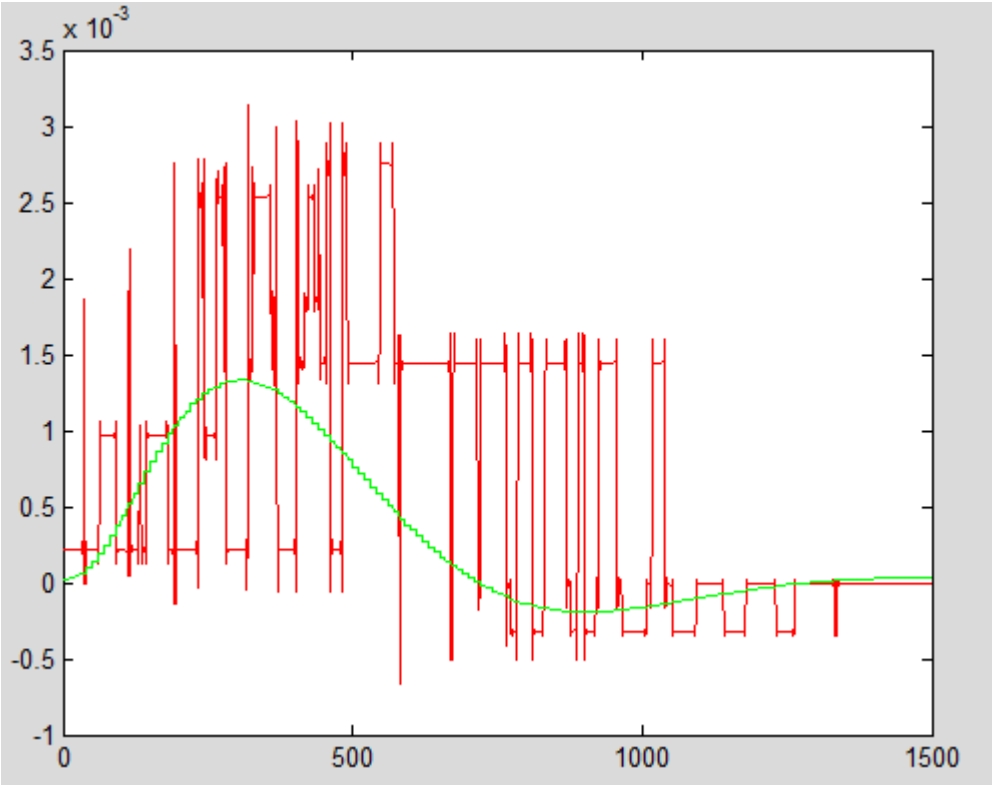

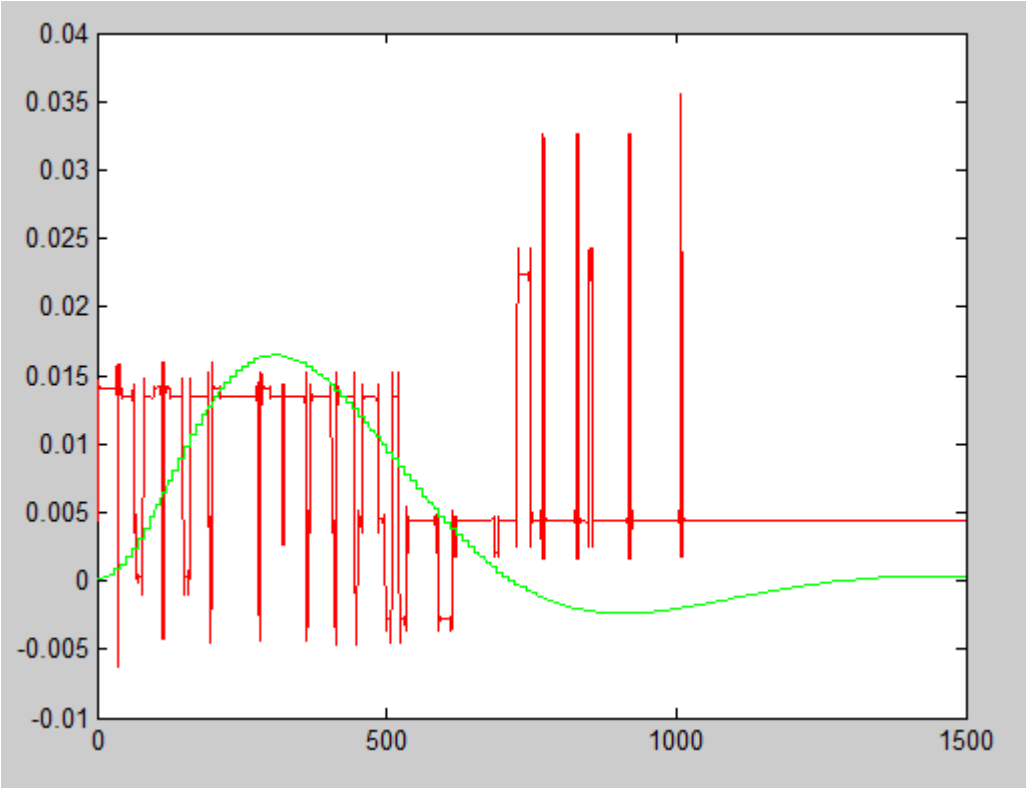

Figure 6.4 Simulated fMRI after curve fitting (red colour is simulated fMRI from GMM and the green colour is simulated fMRI from hrf function)

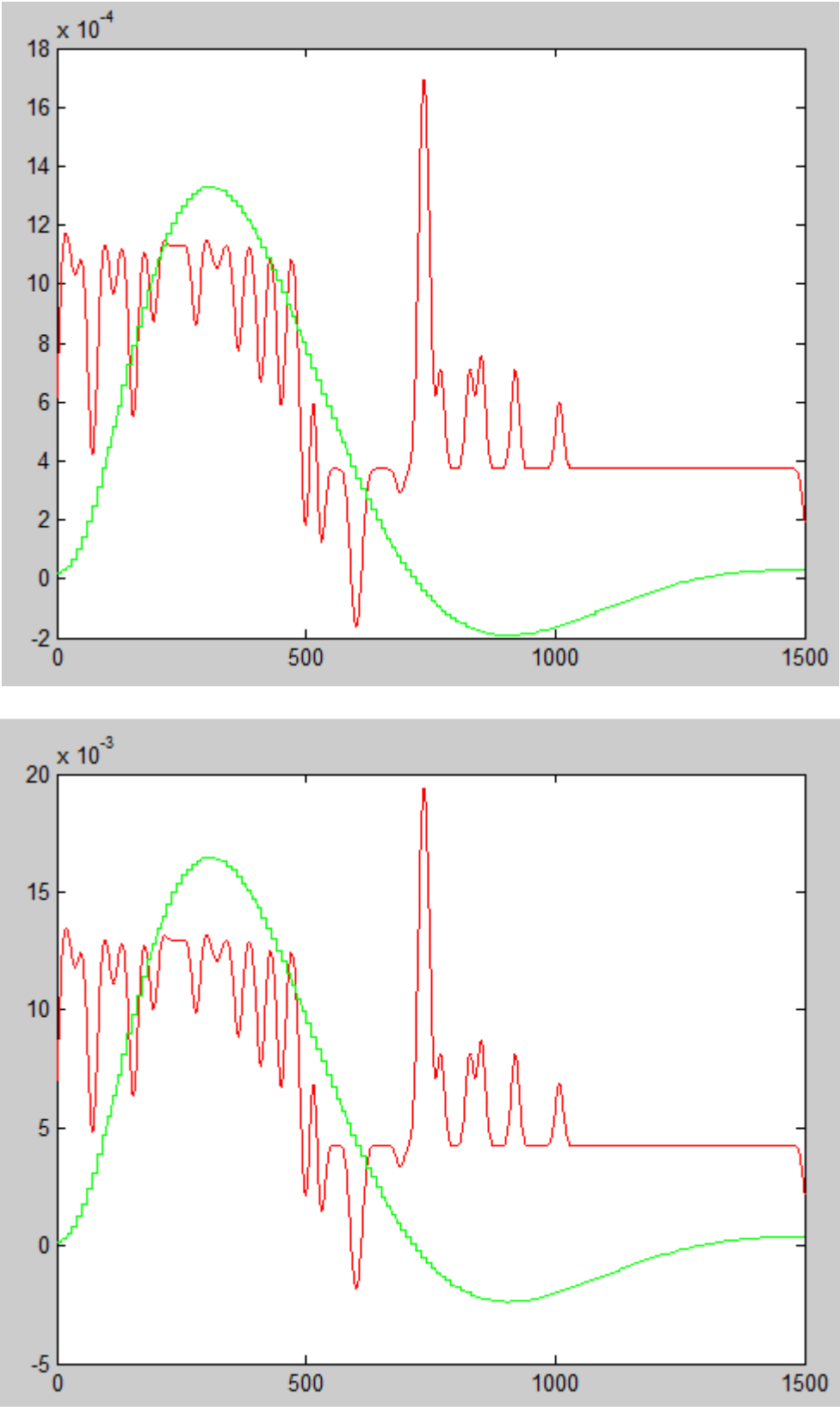

Figure 6.5 Simulated fMRI result with 40 Hz bandwidth Gaussian filter (the red colour is simulated fMRI from GMM and the green colour is simulated fMRI from hrf function)

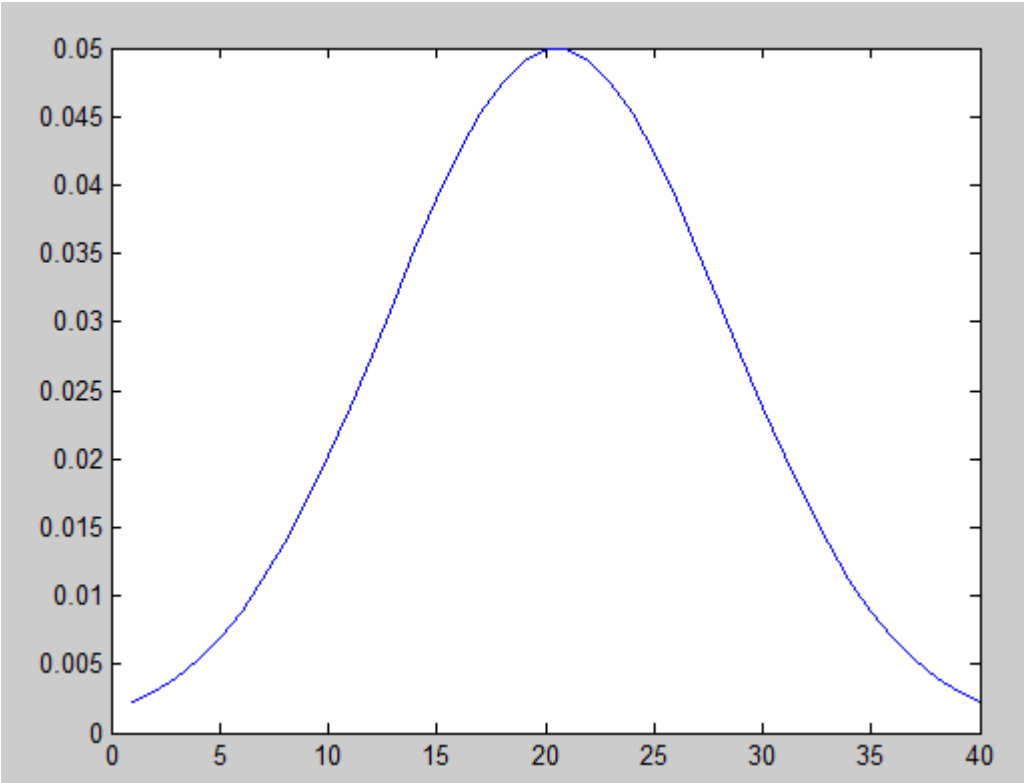

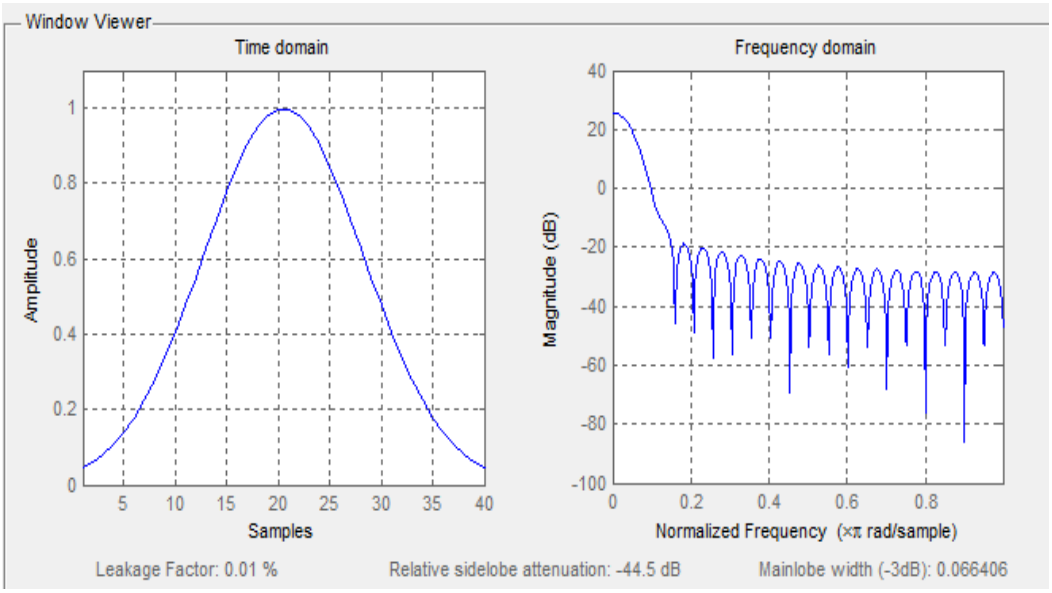

Figure 6.6 40 Hz Bandwidth Gaussian filter

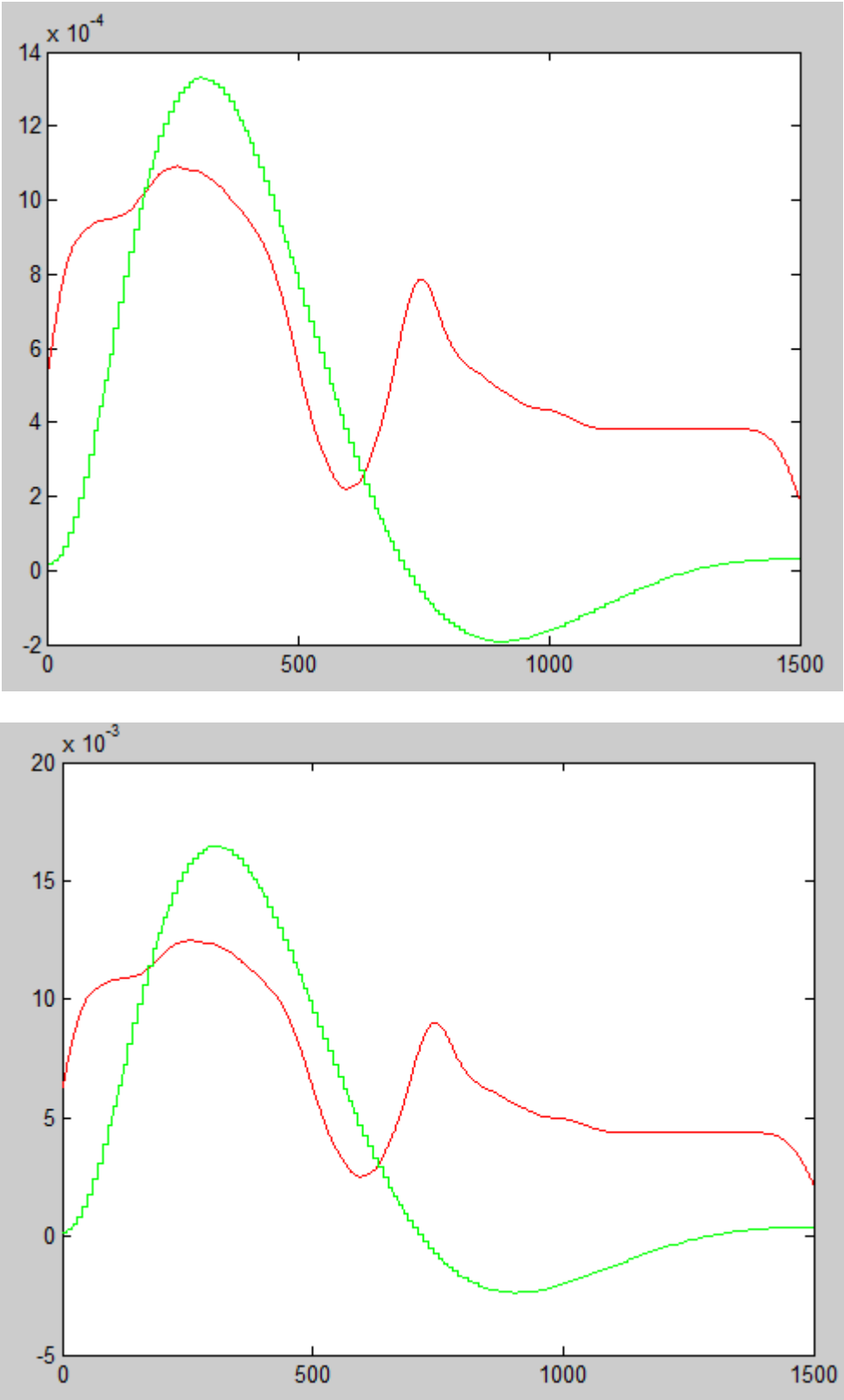

Figure 6.7 Simulated fMRI result with 200 Hz bandwidth Gaussian filters (the red colour is simulated fMRI from GMM and the green colour is simulated fMRI from hrf function)

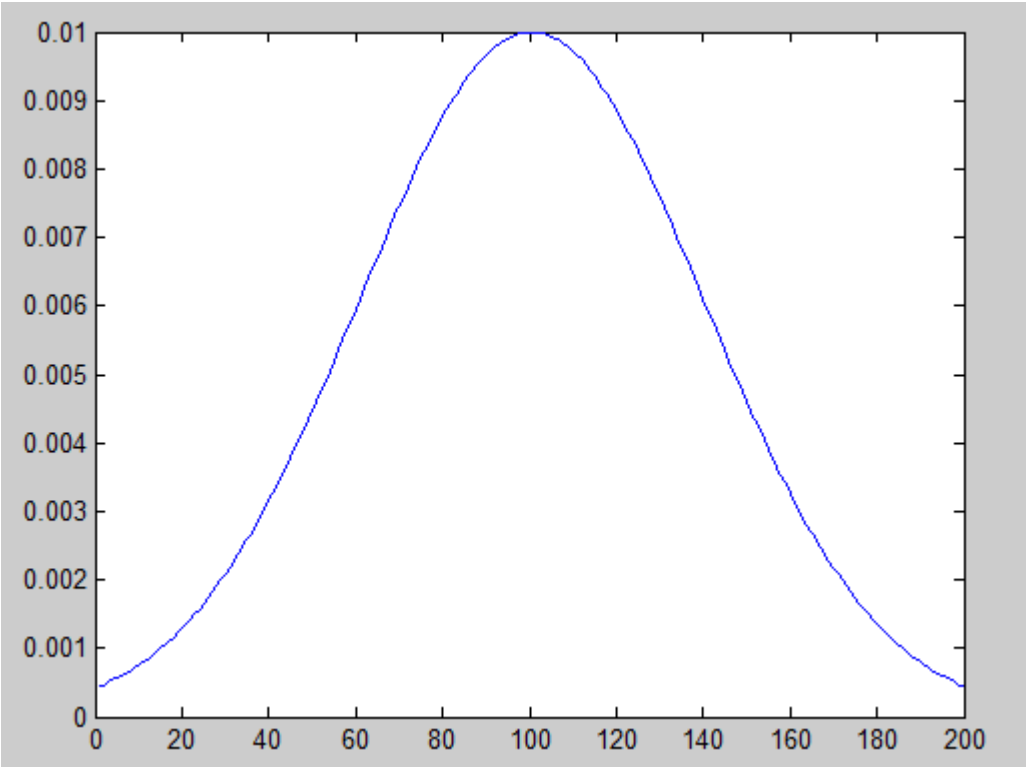

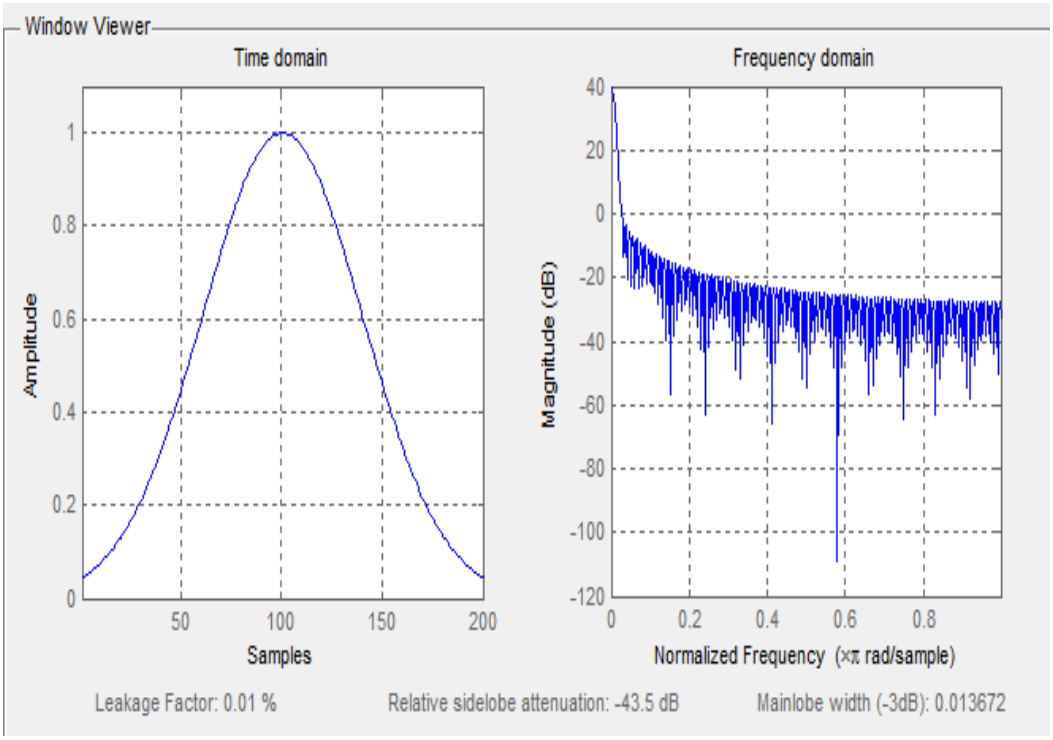

Figure 6.8 200 Hz bandwidth Gaussian filter

6.1.3 EEG-fMRI separation and localisation

In this section, we used synthesis fMRI data from the last section for joint EEG and fMRI separation and localisation. Then, we compared the result from the joint EEG and fMRI with the result from EEG only.

Firstly, we used the minimal norm for EEG only separation. The result is shown in Figure 6.9, whereby the blue line is the original line and the red and green is the result after the minimal norm. The first peak value of original source 1 is 6.452 and the first peak value of original source 2 is 48.224. In addition, the first peak value of the estimated source 1 from EEG only is 2.371 and the first peak value of the estimated source 2 from EEG only is 7.541.

The aim is to get the red and green lines close to the blue lines. The EEG localisation result is shown in Figure 6.10. We choose quite different locations for the original source location in order to show them clearly. The red and green cross '+' represents the original location and the circles denote the result after localisation, so we can see clearly that the green colour source gets the correct localisation but the red colour source is missing.

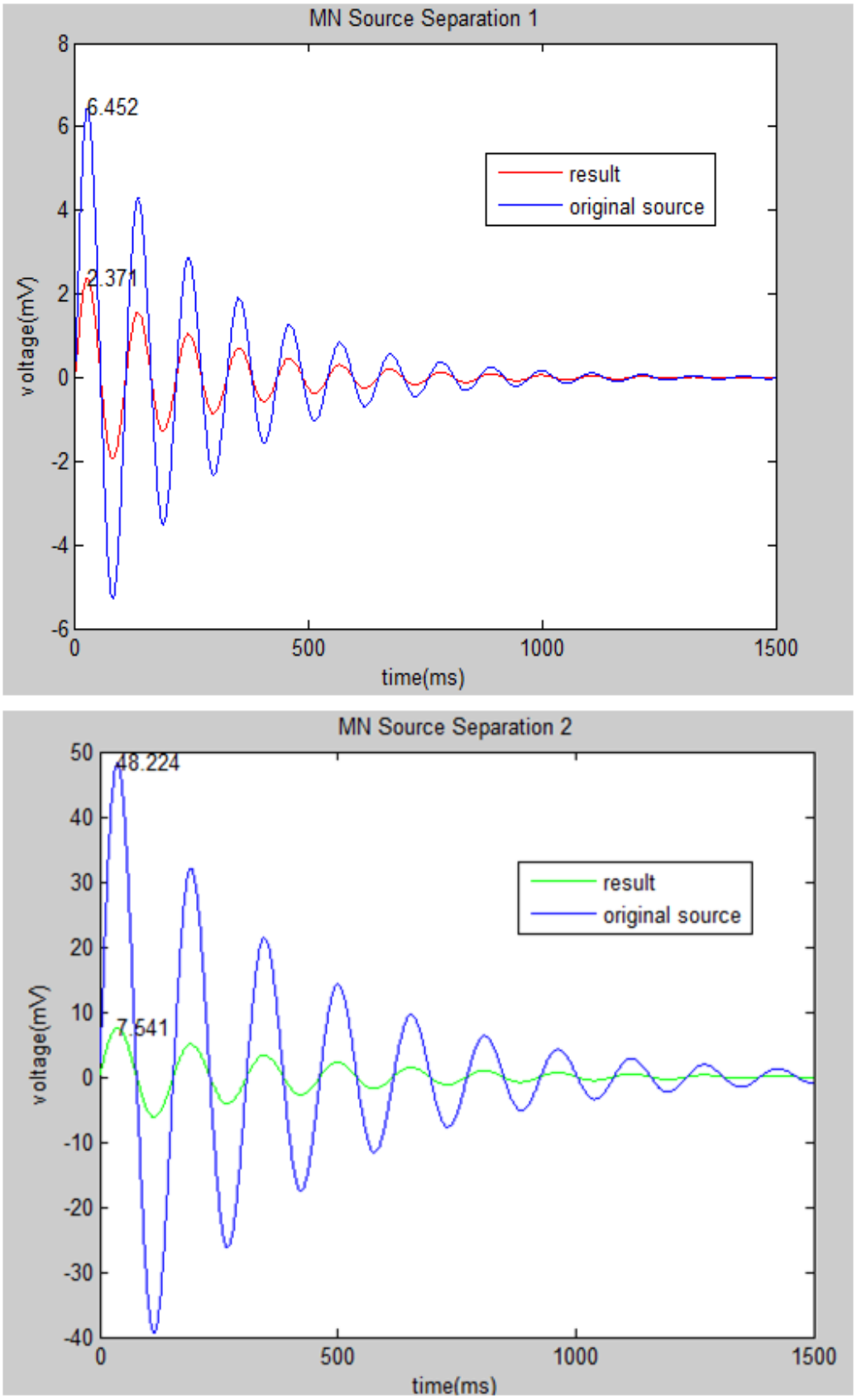

Figure 6.9 Minimal norm separations EEG only

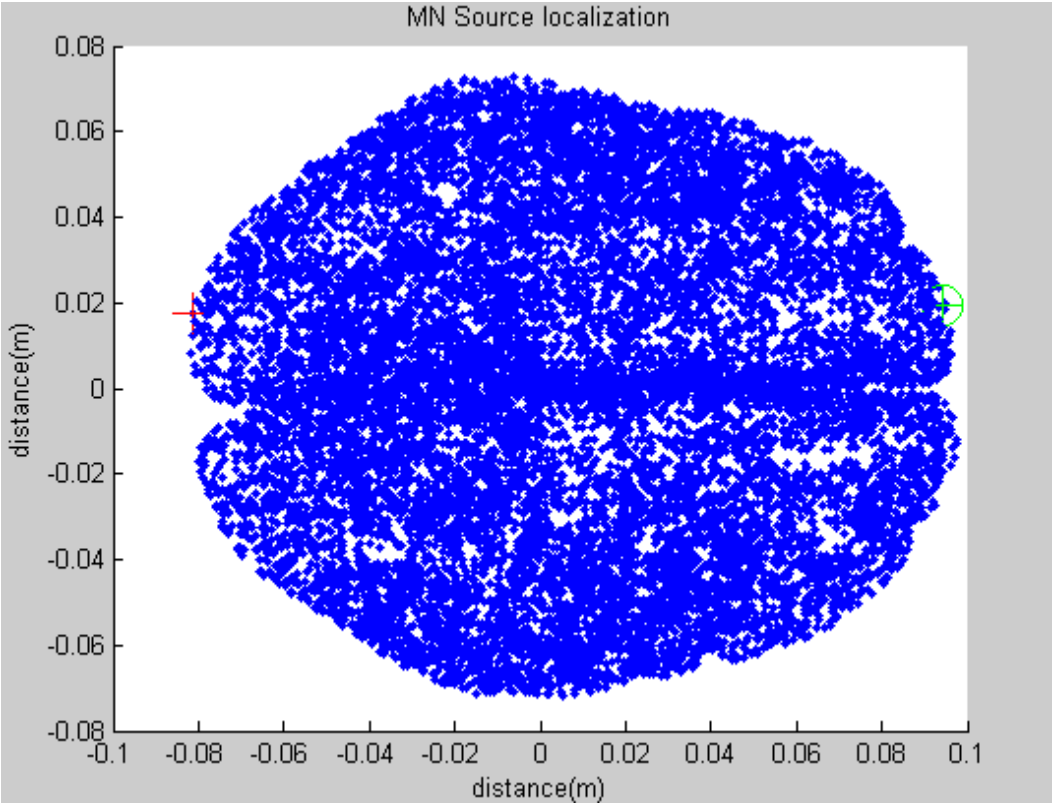

Figure 6.10 Source localisation use EEG only

Secondly we used the joint EEG and fMRI separations, from Brookings' model of reduce joint inverse algorithm (MRJI) **[31]**. The result of the source separation can be seen in Figure 6.11 and the source localisation result is shown in Figure 6.12. The first peak value of the original source 1 is 6.452, and the first peak value of the original source 2 is 48.224. The first peak value of the estimated source 1 from MRJI is 2.825, and the first peak value of the estimated source 2 from MRJI is 8.483, which means that MRJI algorithm which uses EEG and fMRI provides more accurate estimates than MN algorithm which uses EEG only.

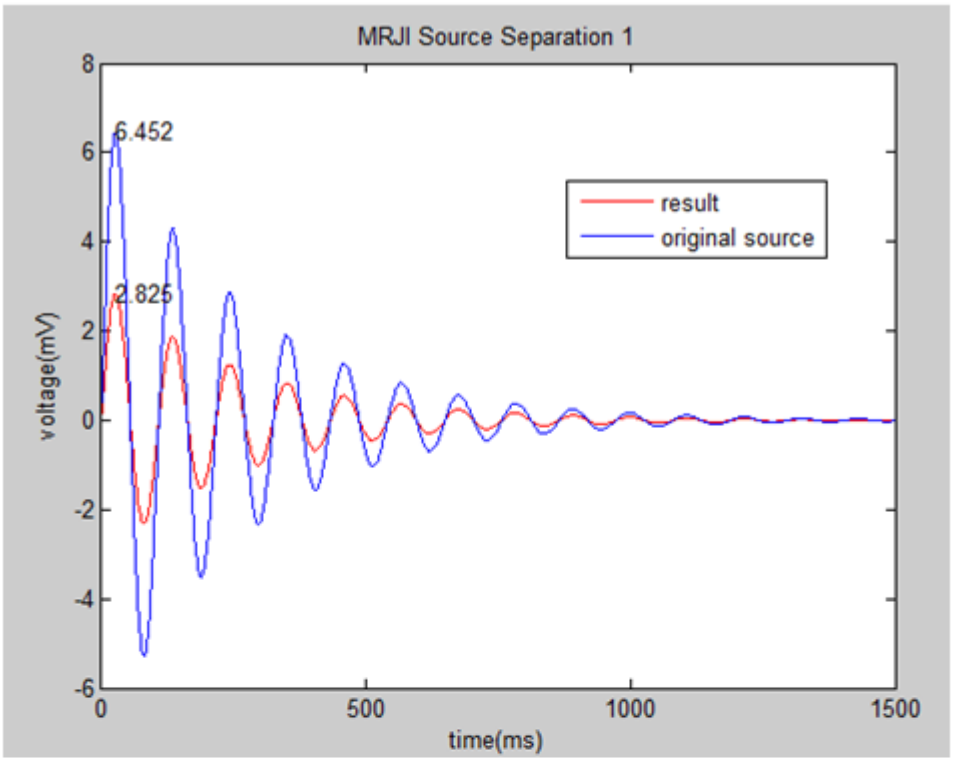

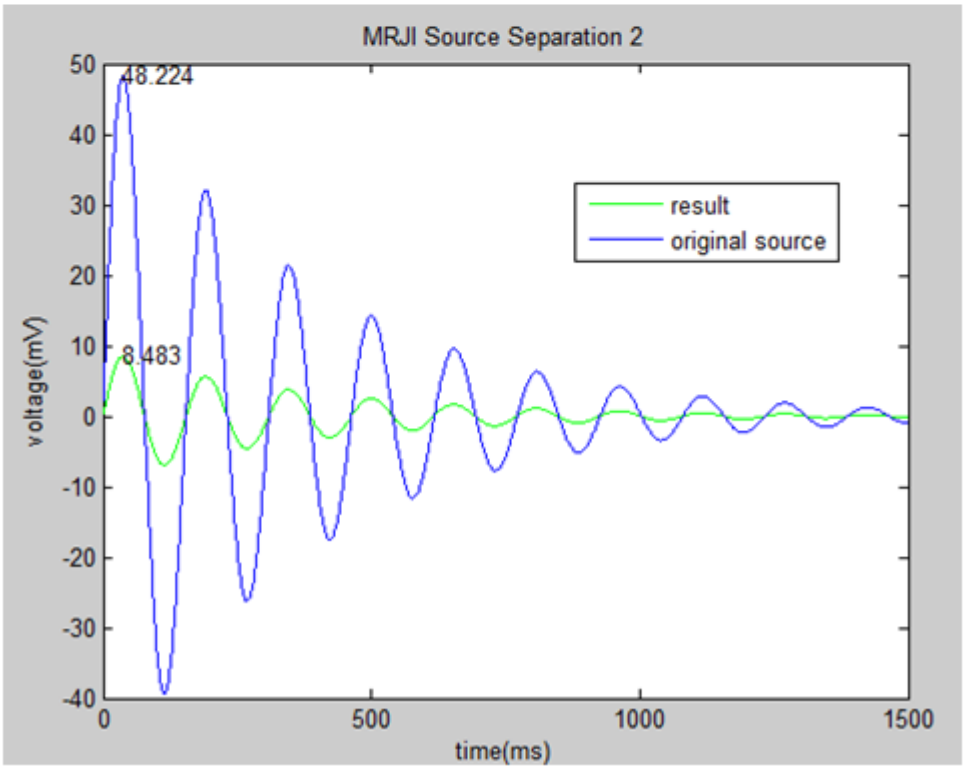

Figure 6.11 MRJI source separations

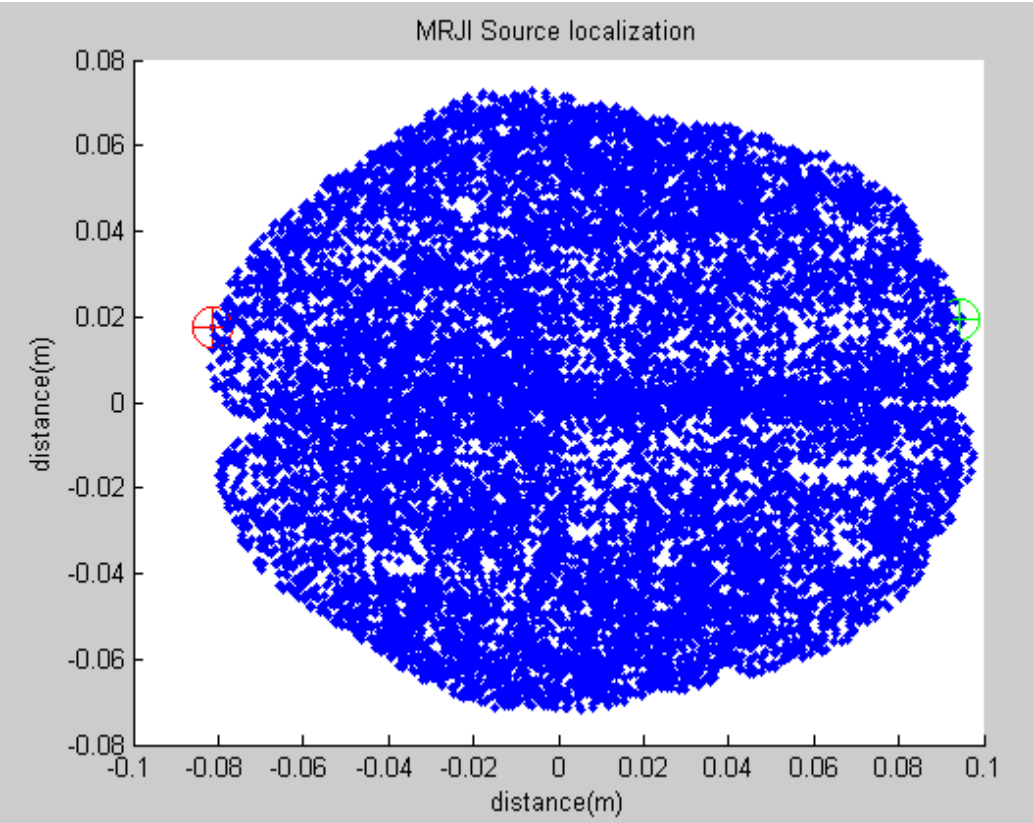

Figure 6.12 Source localisation base on joint EEG-fMRI

Compared with Figures 6.9 and 6.11, the red and green curves are close to the blue line in Figure 6.11; specifically, the source 1 for MN separation is 2.371 in Figure 6.9 and for MRJI is 2.825 in Figure 6.11; the source 2 for MN separation is 7.541 in Figure 6.9 and 8.483 in Figure 6.11. In addition, both the correlation between the original and estimated sources from the EEG only and from MRJI are 1, therefore, it is enough to compare the result while only using the first peak value. Therefore, joint EEG and fMRI can get more accurate separation. Compared with Figures 6.10 and 6.12, the result of Figure 6.10 got one successful localisation but missed one source, whereas Figure 6.12 got both sources correct. Therefore, joint EEG and fMRI can obtain more precision localisation.

6.2 Experiment on four neural activities

In this section, we extend the number of neural activities to four to test our algorithms with a larger number of sources. This number is in line with the number of sources used in similar evaluations by other researchers [5,6]. This experiment is based on four neural activities (two pairs of neural activities) for training data, and only uses two neural activities (one pair of neural activities) for test data. The experiment procedure is similar to two neural activities (section 6.1).

We created four neural activities using damped sinusoid, as two neural activities only work on 1 to 1500 and the other two work on 1501 to 3000. Four neural activities are shown in Figures 6.14 and 6.15. Four neural activities locations are shown in Figure 6.13. The red curve in Figure 6.14 corresponds to the red cross in Figure 6.13; the green curve in Figure 6.14 corresponds to the green cross in Figure 6.13; the magenta curve in Figure 6.15 corresponds to the magenta cross in Figure 6.13 and the cyan curve in Figure 6.15 corresponds to the cyan cross in Figure 6.13.

We can obtain the EEG and fMRI signals, which use the four neural activities only, by using the lead field matrix and hrf function, which is solved before the EEG signals shown in Figure 6.16.

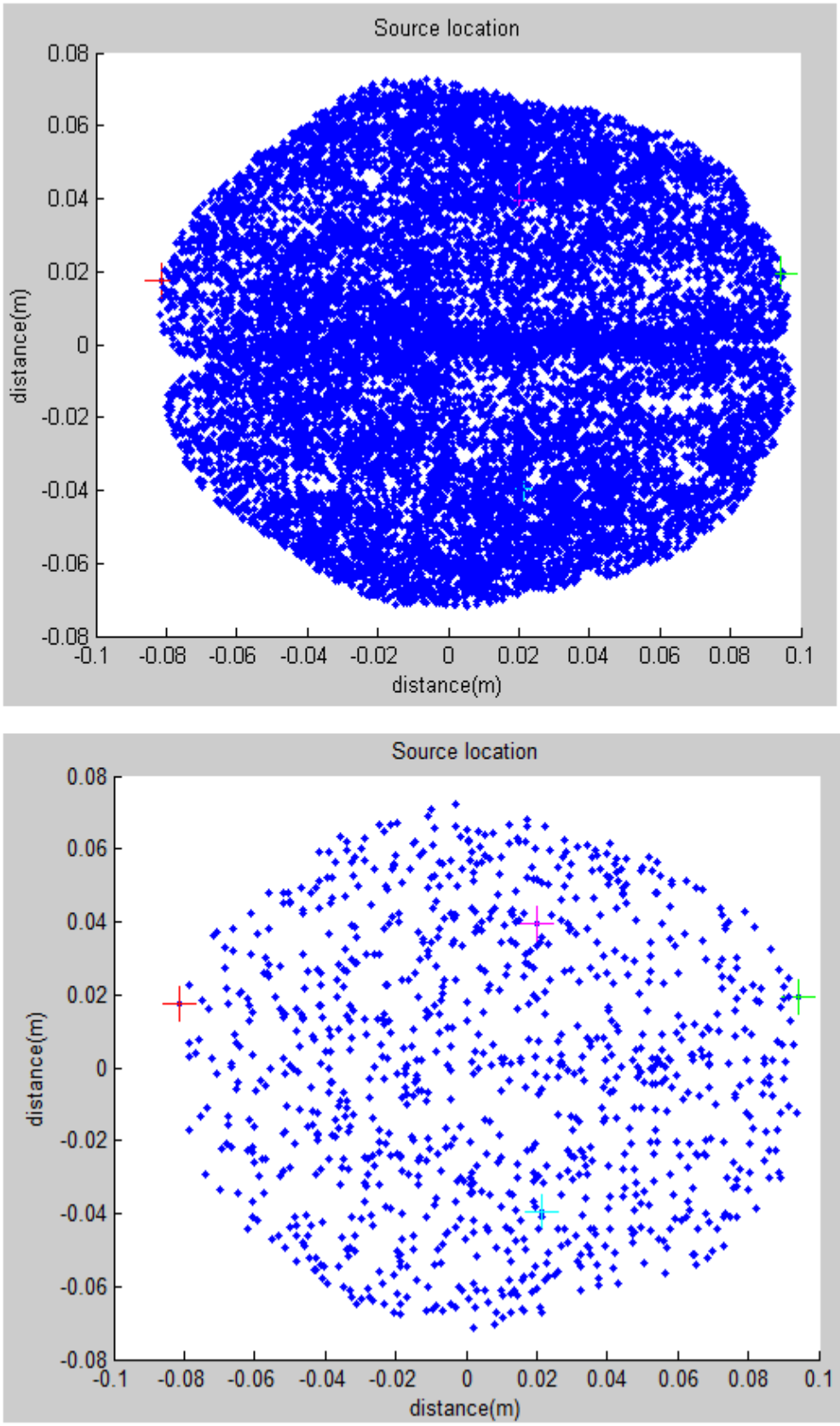

Figure 6.13 Four neural activities location

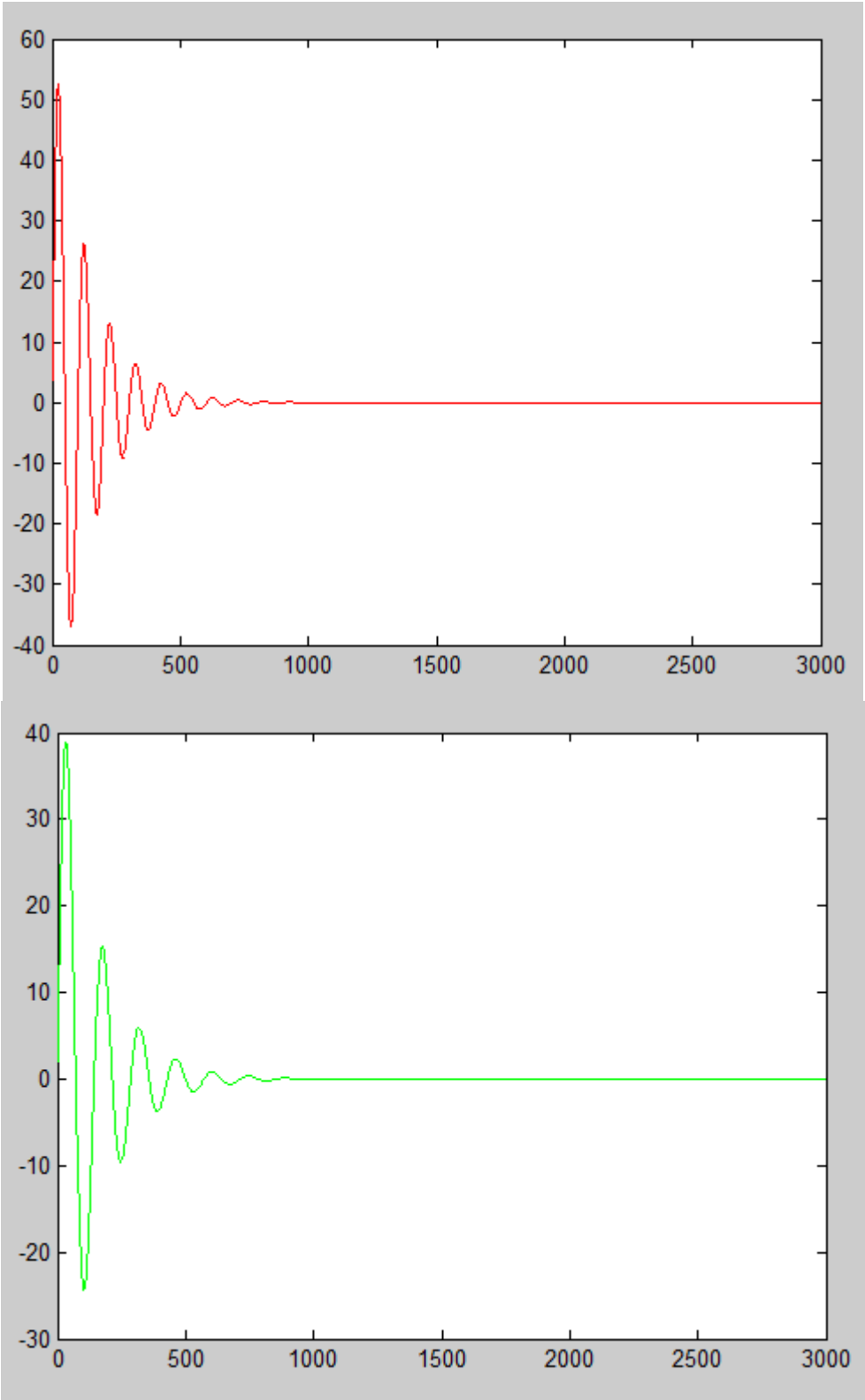

Figure 6.14 Four neural activities

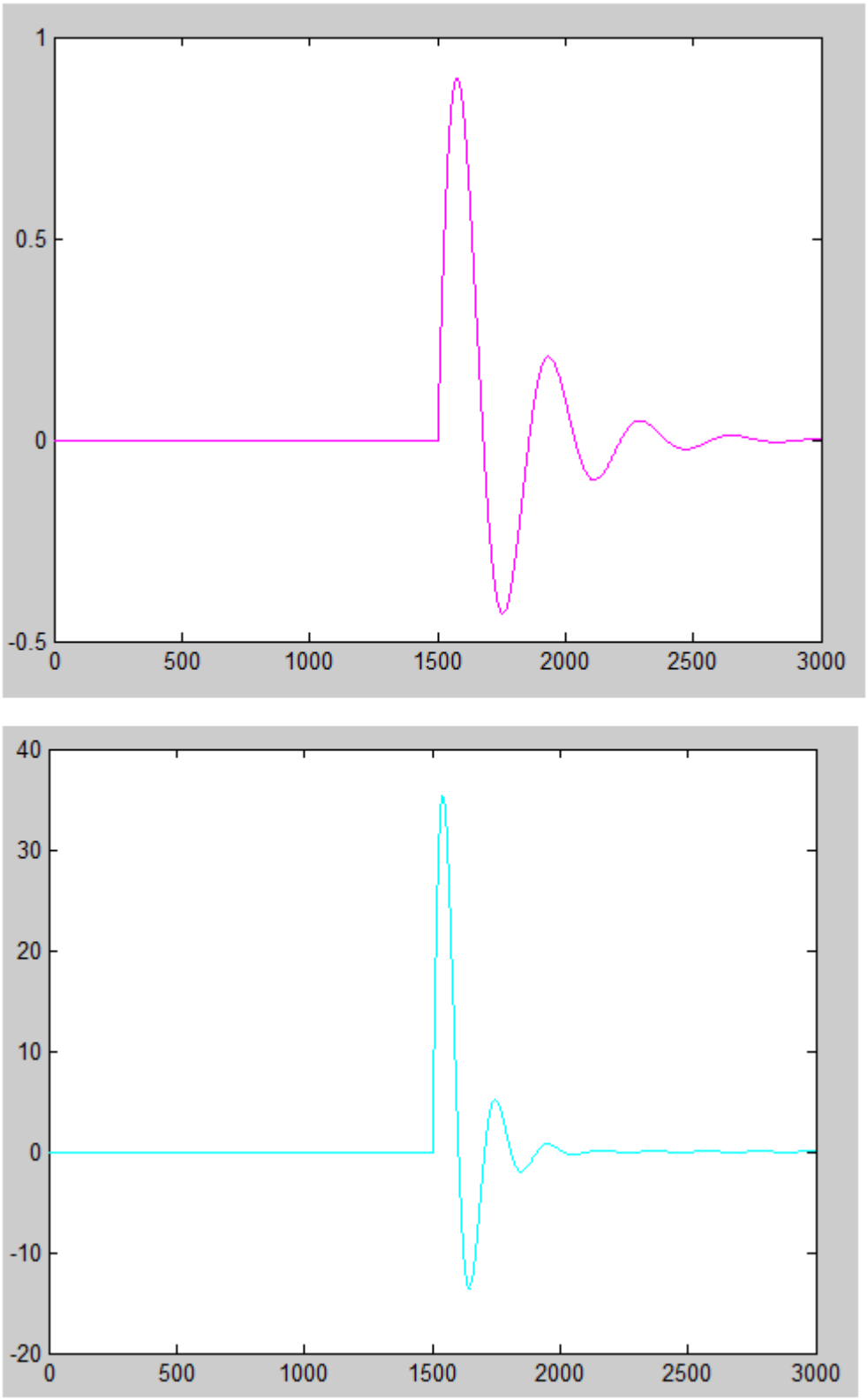

Figure 6.15 Four neural activities

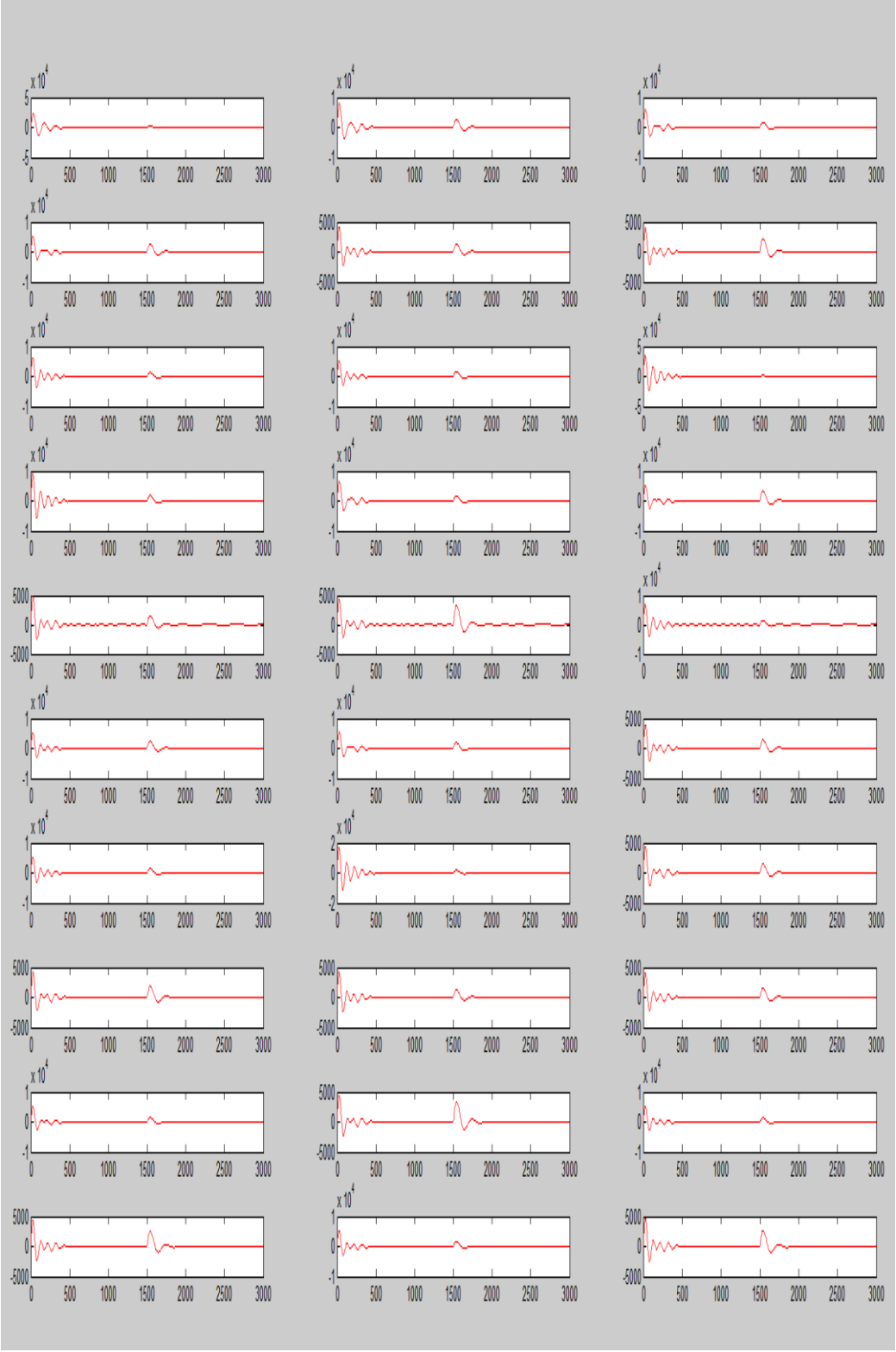

Figure 6.16 EEG from four neural activities

Then, we build the GMM dataset based on PCA, as shown in Figure 6.17. These three subplots are the three dimensionality of the dataset.

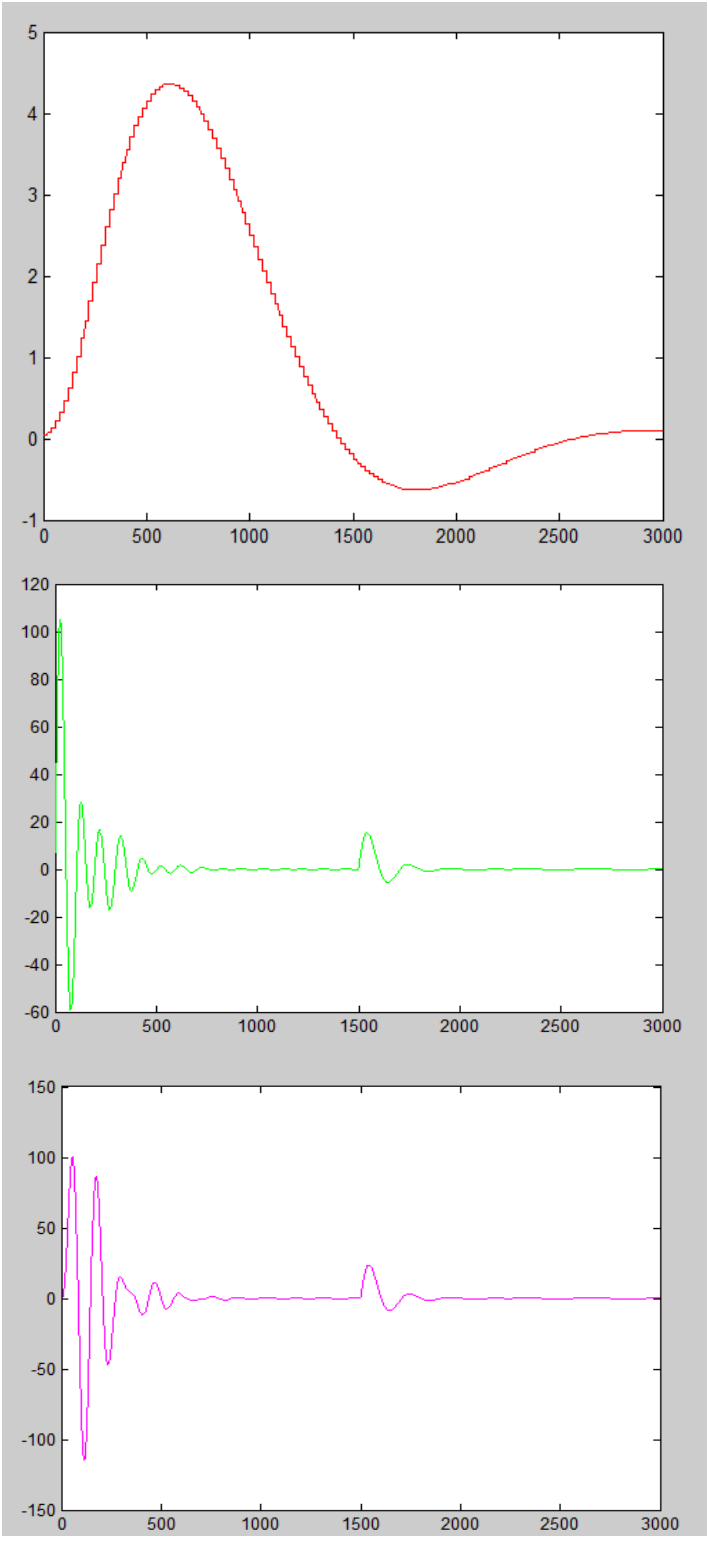

Figure 6.17 GMM dataset

GMM parameters are estimated using expectation maximisation (EM) algorithm. Next we build the GMM, and the clusters distribute in 3D can be shown in Figure 6.18, whereby each red dot is the cluster centre and the blue curve is a

GMM dataset. The ellipsoid distribution is shown in Figure 6.19 and the clearer distribution of the cluster is shown in Figure 6.20, with each colour and each sign denoting different distributions.

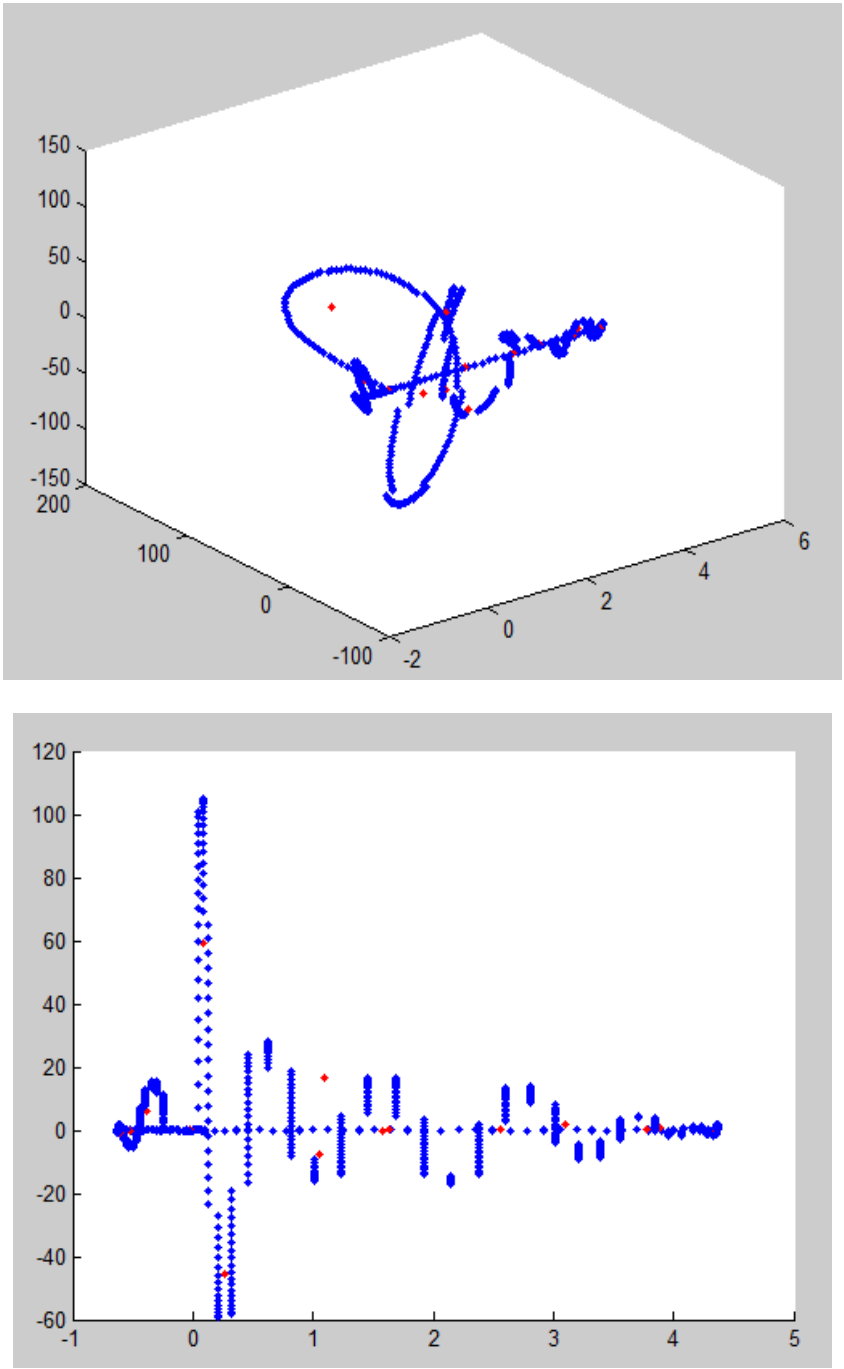

Figure 6.18 GMM cluster distribution

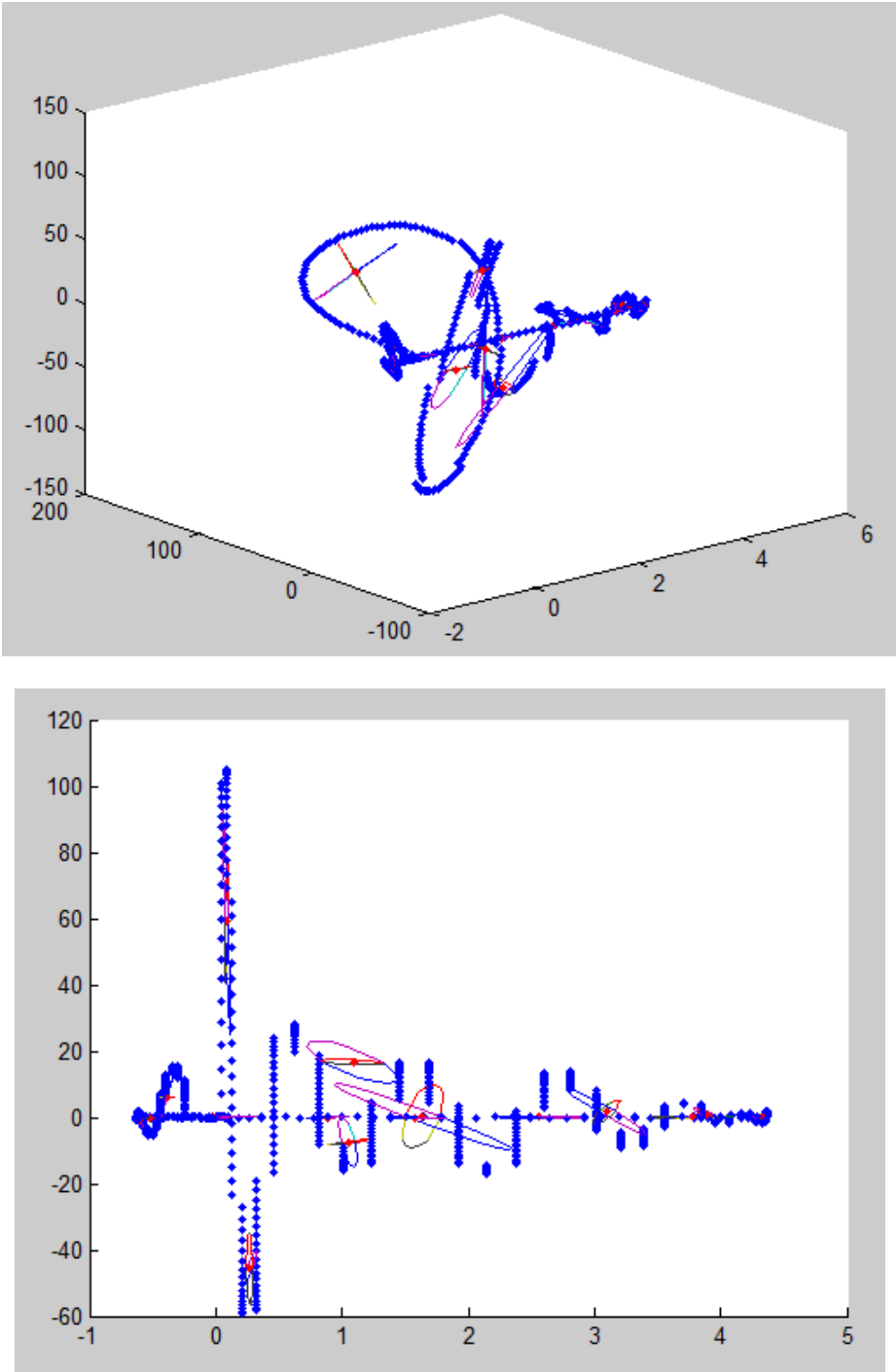

Figure 6.19 GMM cluster ellipsoid distribution

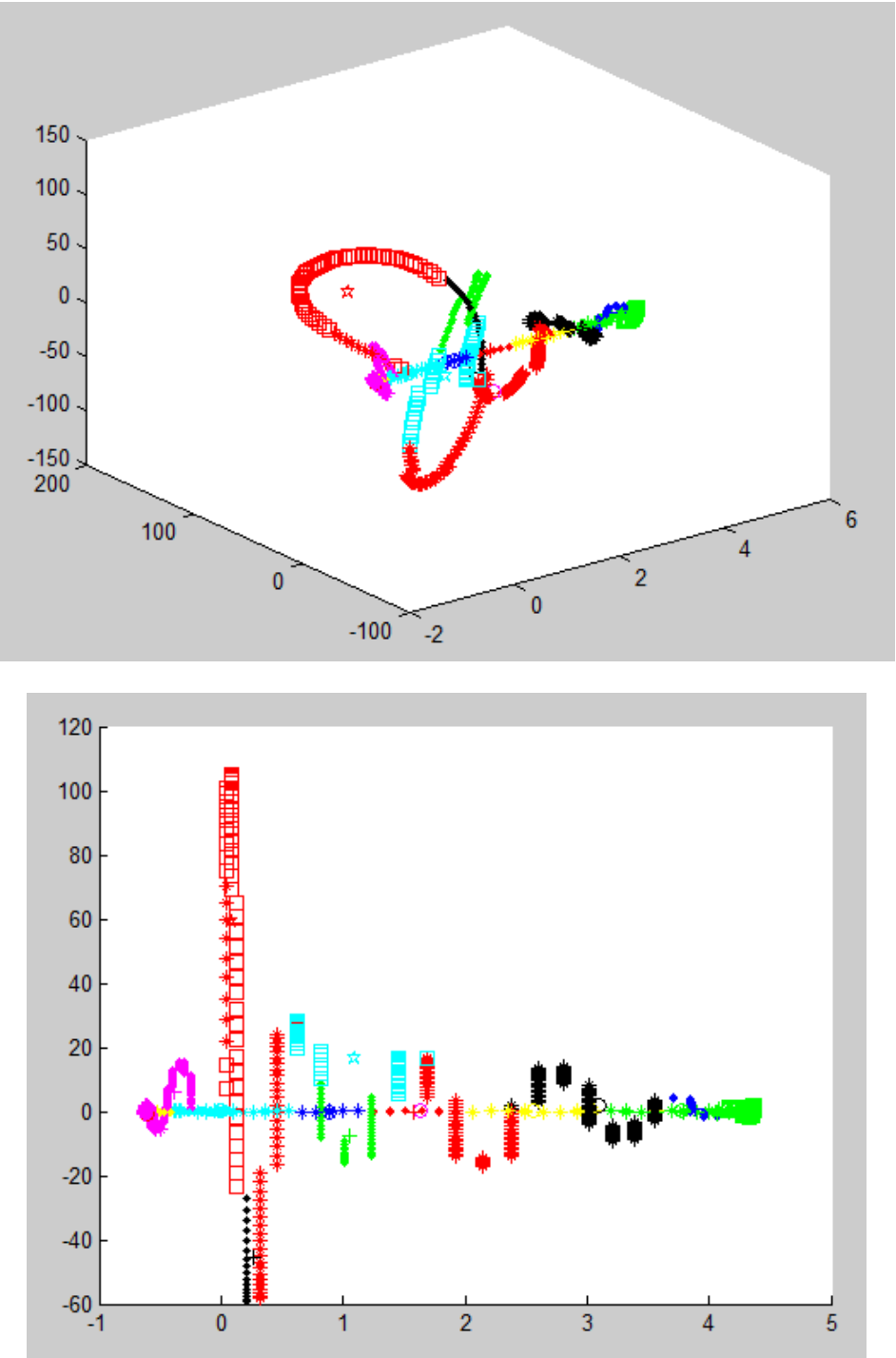

Figure 6.20 GMM clusters clearly distribution

For test data, we only used the two neural activities. Firstly, we used the neural activities from Figure 6.14 for test data, and the result is shown in Figure 6.21. The green colour curve is the simulated result from hrf function and the red colour dot is the result from GMM. The simulated result after the spline function is shown in Figure 6.22. Gaussian filter information is shown in Figure 6.23 and

the final simulated fMRI result is shown in Figure 6.24.

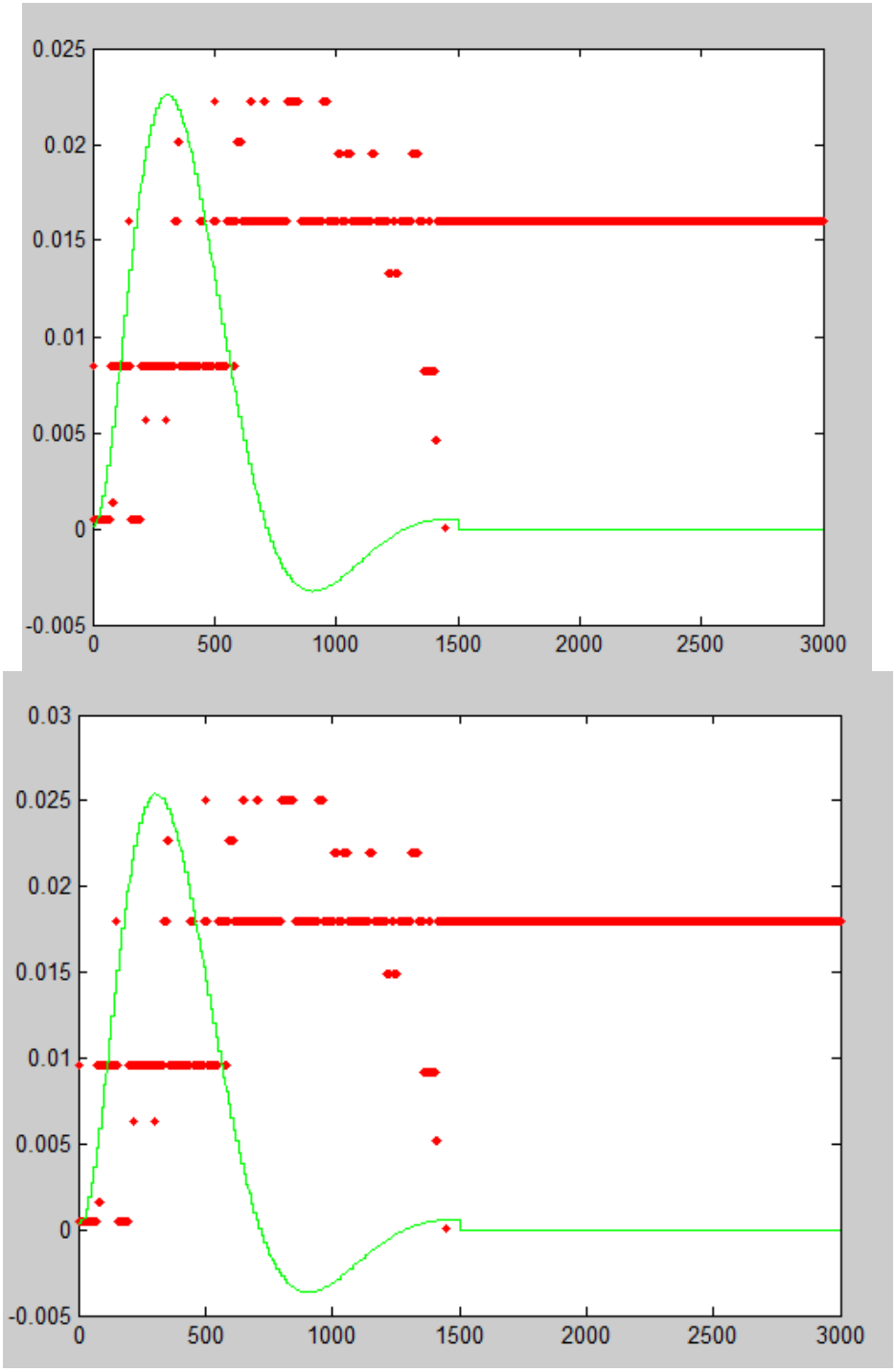

Figure 6.21 Simulated fMRI results after GMM

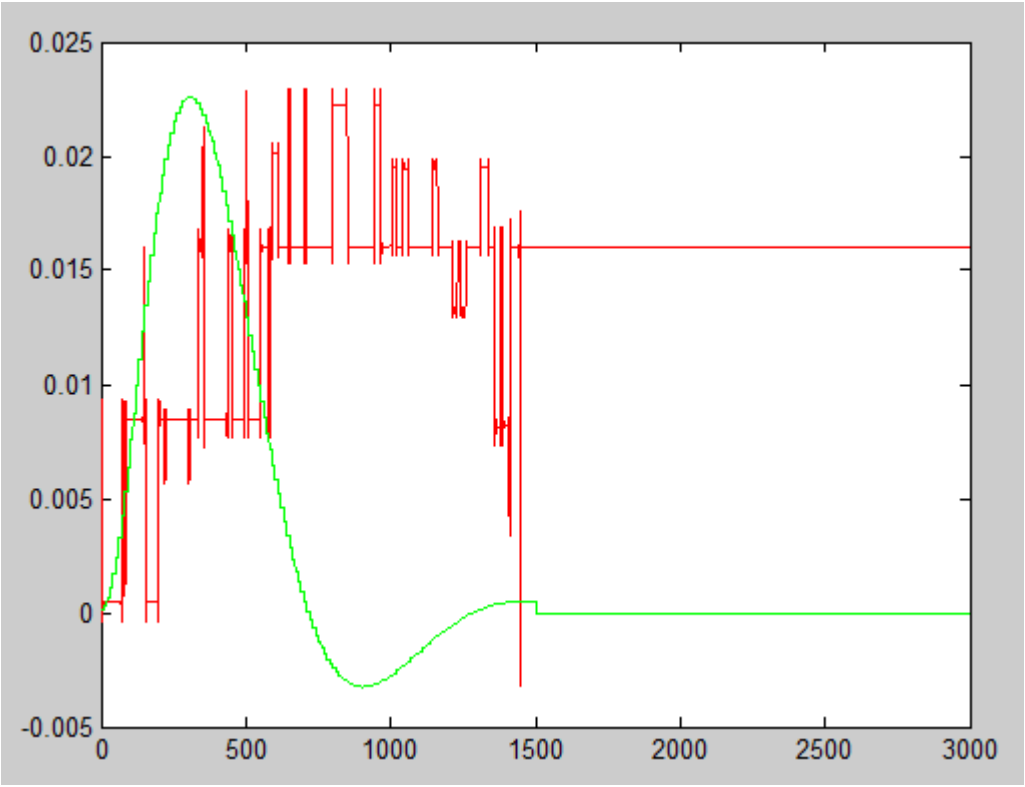

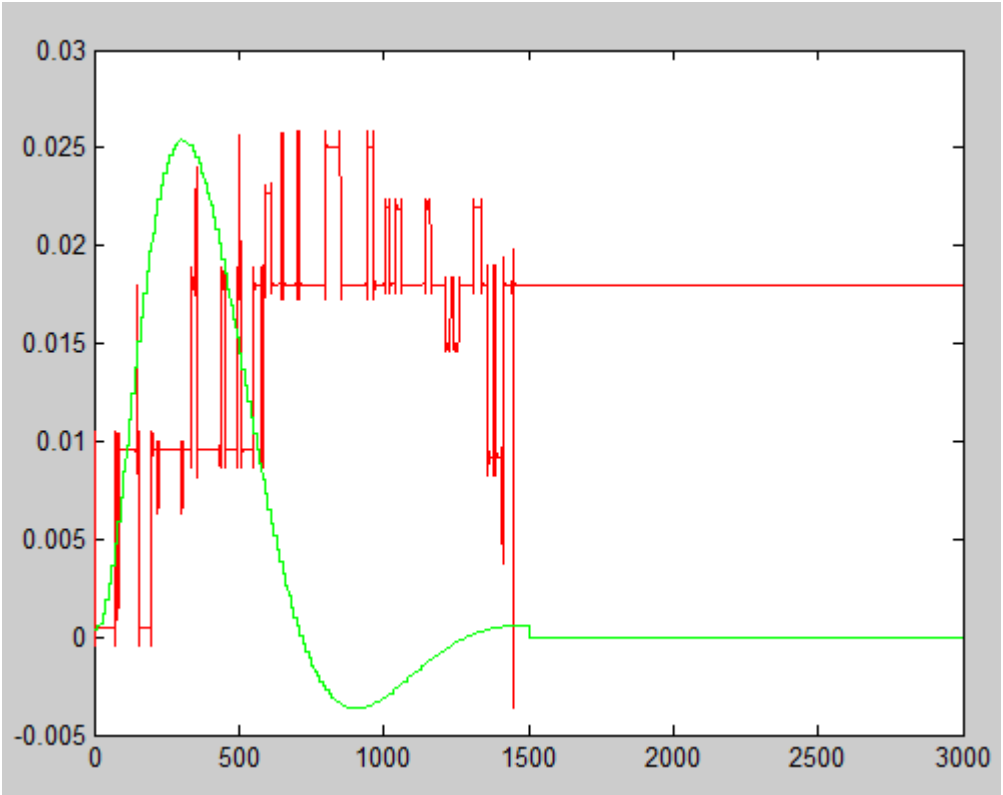

Figure 6.22 Simulated fMRI results after spline function

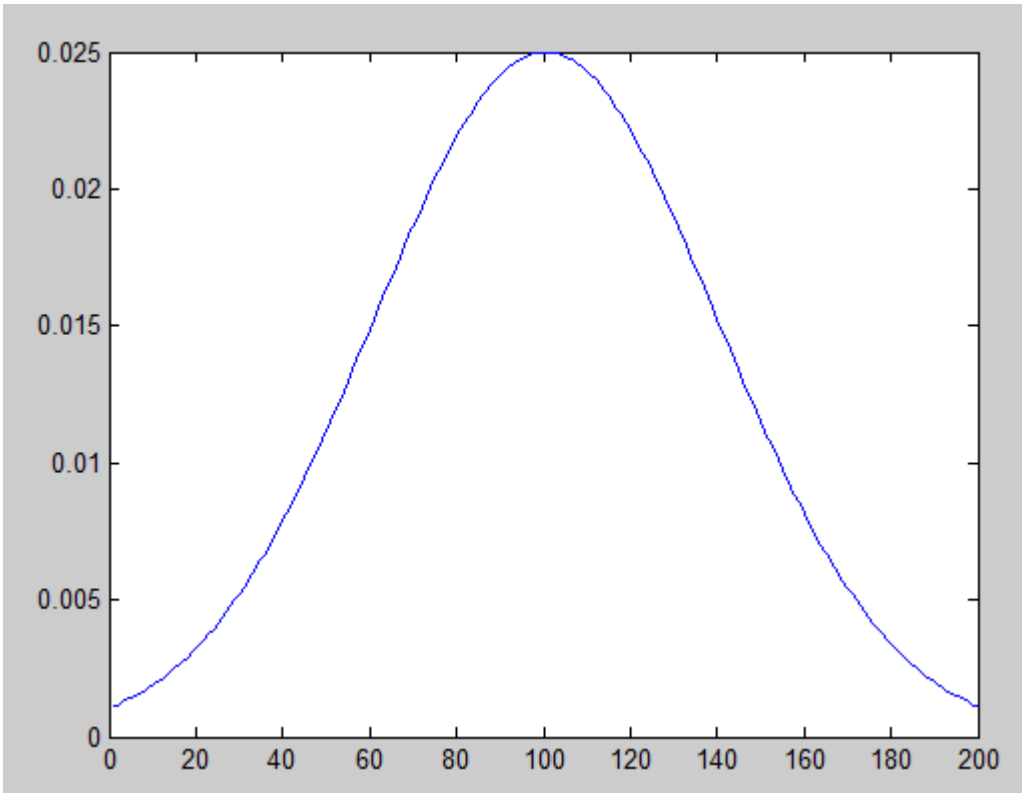

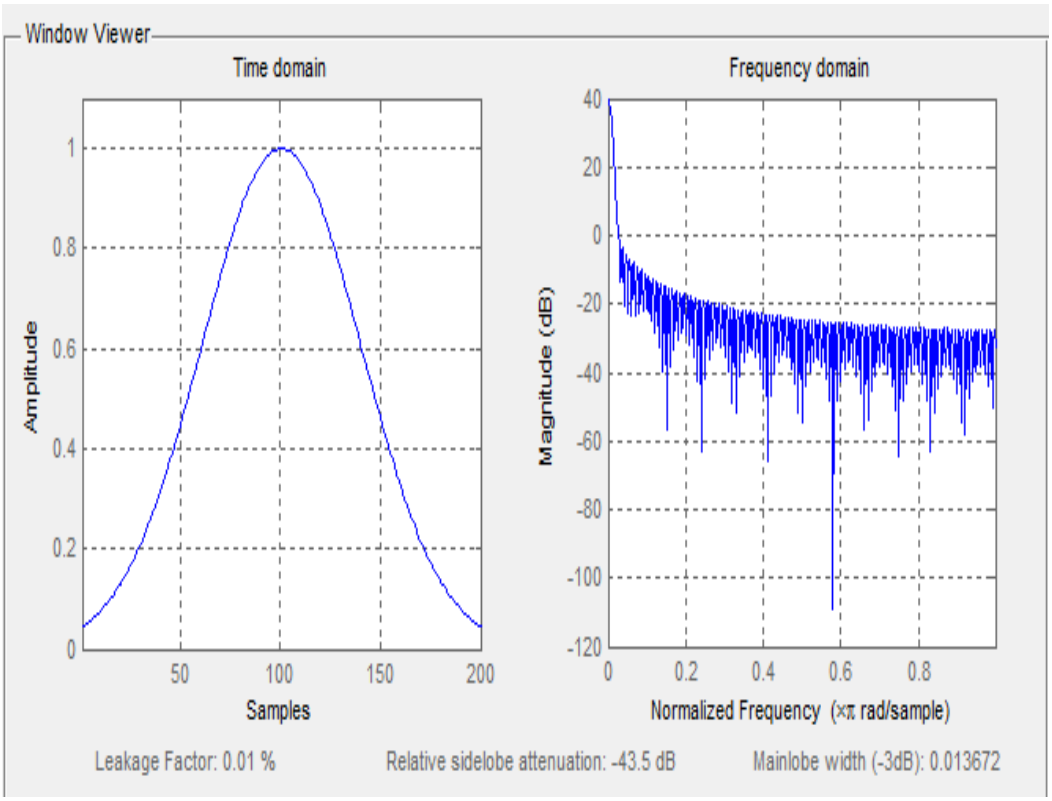

Figure 6.23 Gaussian filter information

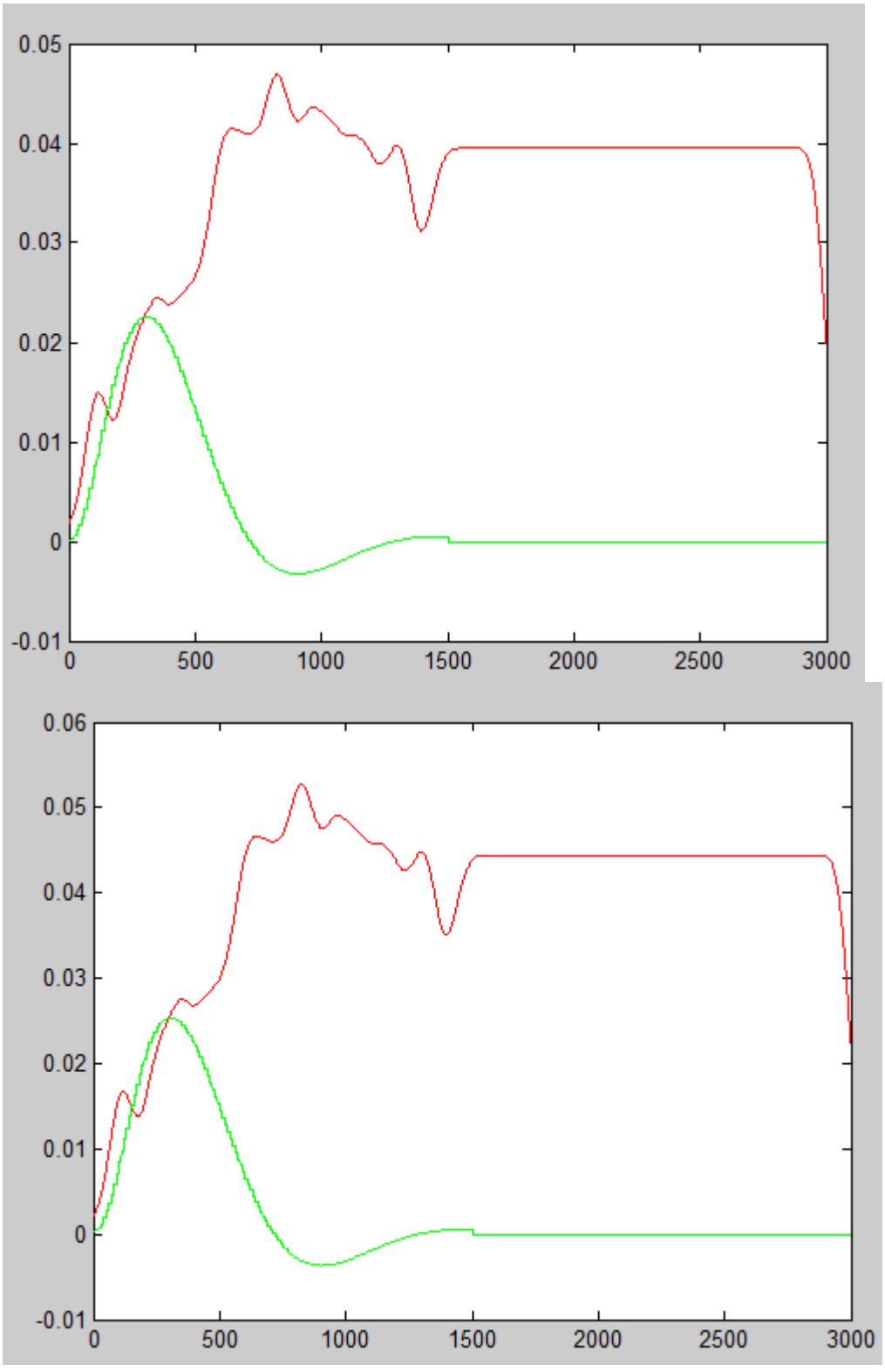

Figure 6.24 Simulated fMRI results after Gaussian filter

After that we ran the fMRI data into the MRJI algorithm and compared the result to the MN algorithm. MN source separation result is shown in Figure 6.25 and localisation result is shown in Figure 6.26. MRJI source separation result is

shown in Figure 6.27 and the localisation result is shown in Figure 6.28.

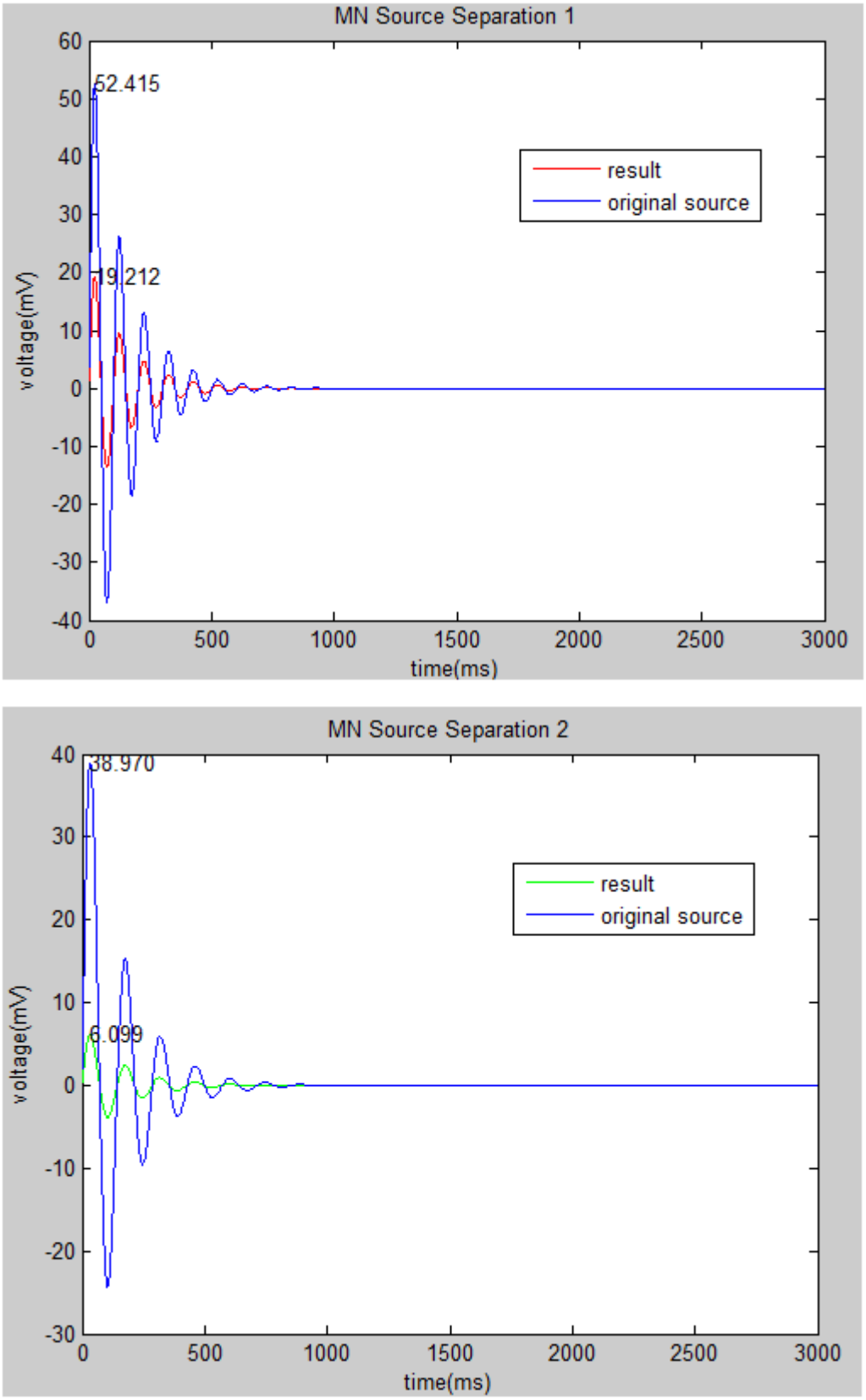

Figure 6.25 MN source separations

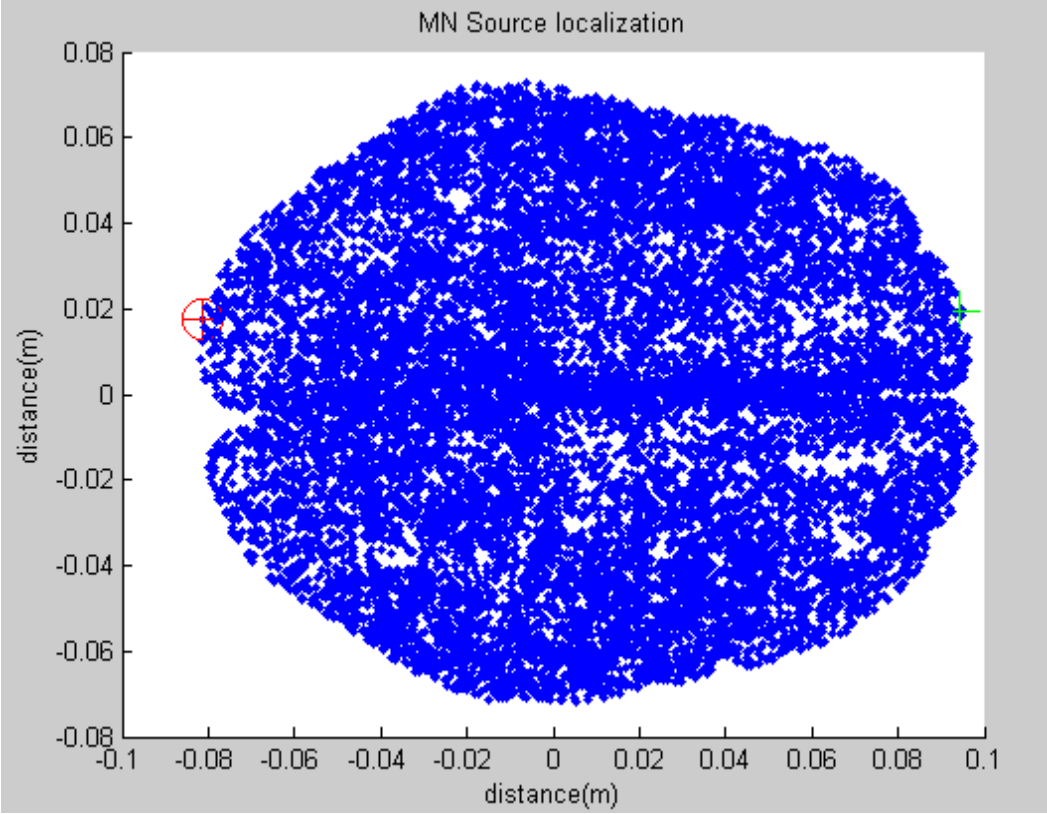

Figure 6.26 MN source localisations

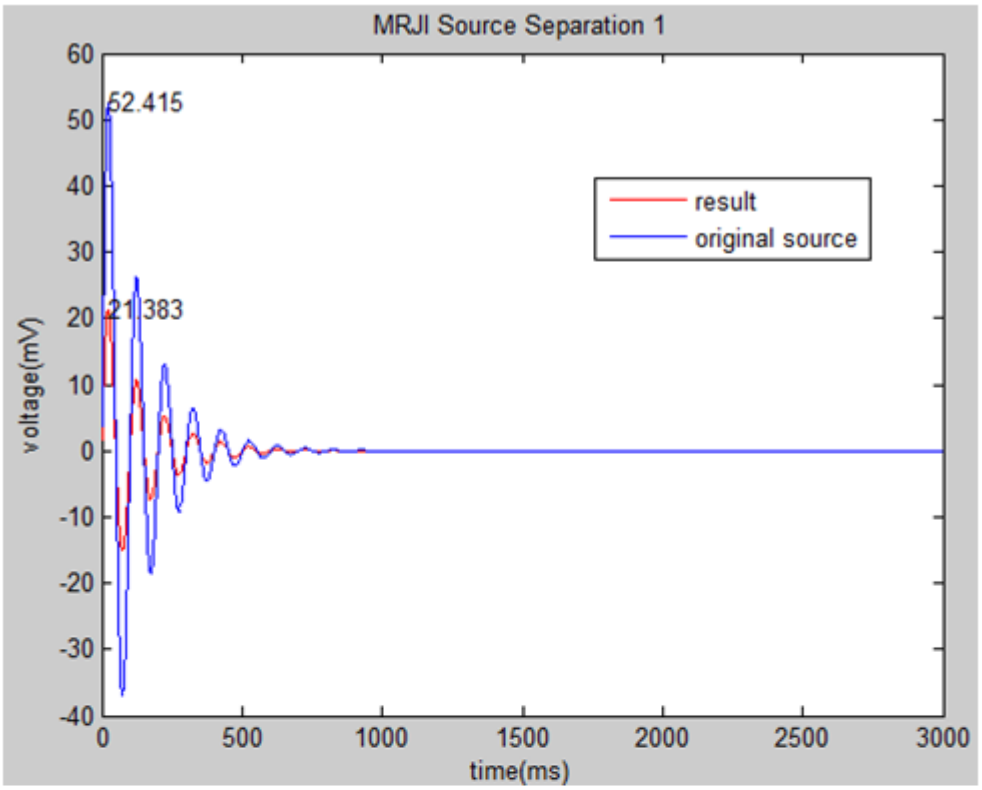

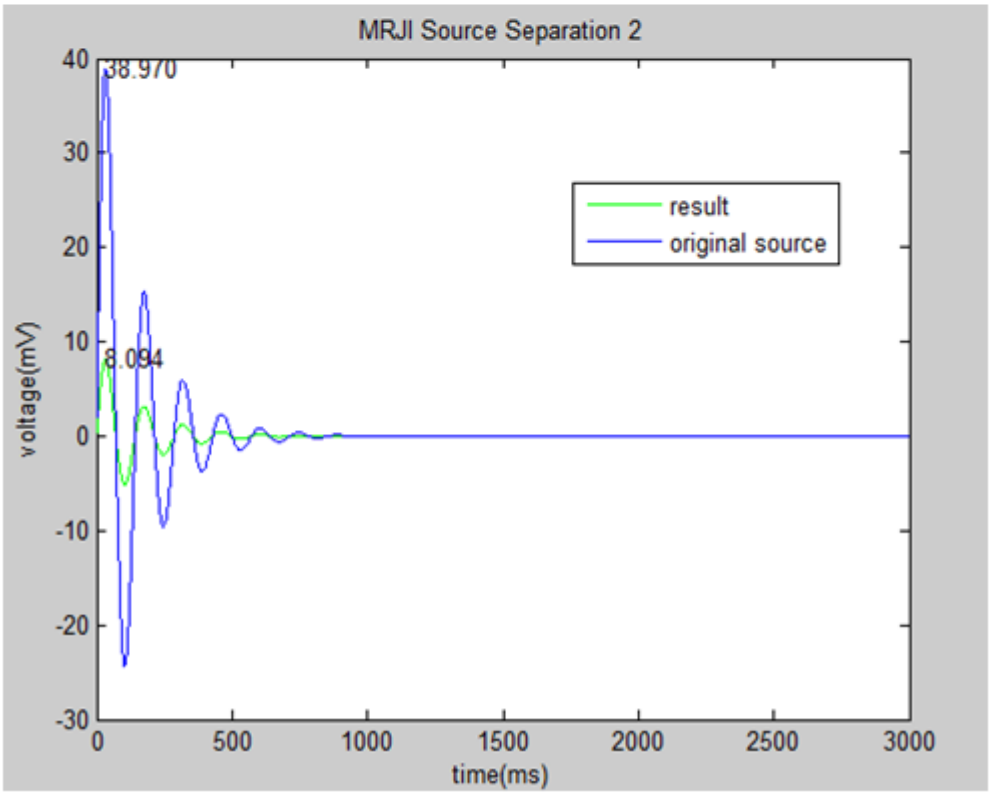

Figure 6.27 MRJI source separations

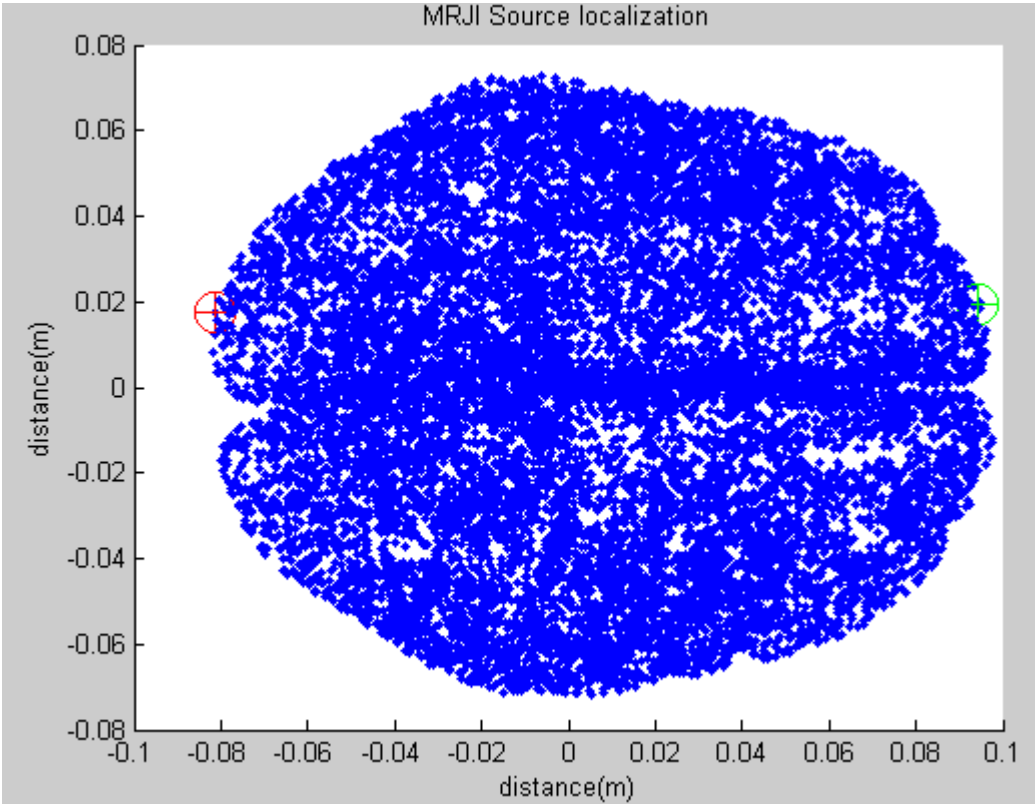

Figure 6.28 MRJI source localisations

Compared with Figures 6.25 and 6.27, the peak value of first source separation by MRJI is 21.383, which is better than the peak value of first source separation by MN is 19.212. And for the second source separation, the peak value solved by MRJI is 8.094, which is better than the peak value solved by the MN algorithm of 6.099. In addition, both the correlation between the original source and the estimated source form EEG only and from MRJI are equal 1. Therefore, it is enough for the result to only compare the first peak value. For localisation, the MN source localisation misses the source 2, which cannot find the green circle in Figure 6.26. For MRJI source localisation, both sources obtain the correct localisation in Figure 6.28. Therefore, MRJI can better obtain the EEG source separation and localisation.

Therefore, synthesis fMRI for joint EEG and fMRI source separation and localisation could also give a better result than EEG only.

7. Conclusion and future work

7.1 Conclusion

The focus of this research was separation of EEG signals into the signals produced by independent neural sources in the brain. The applications of this technique are numerous, including neuroscience, medicine and Human Brain Interfaces.

Whilst the preferable mode of recording the brain signals in many applications is EEG due to its low cost and easy portability, it is known that fMRI recording modality produces superior spatial resolution and hence could be better for interpreting brain activity. It has also been shown in the past that joint EEG-fMRI source separation separates the signals more accurately.

The hypothesis that was tested in this research is that we can create a joint model of EEG-fMRI signals recorded simultaneously, which could be used in the future in conjunction with the new EEG-only signals in the source separation procedure to improve the accuracy of estimating the independent neural sources.

The original objectives of this research were as follows:

1. Develop a set of generative features describing EEG and fMRI signals to decrease the dimensionality of the data by removing irrelevant information and unwanted noise.
2. Create a model of the correlations between EEG and fMRI data to remove the necessity of using fMRI machines for fMRI-assisted EEG separation.
3. Develop a method for source separation of EEG data relying on the above model of correlations to increase the accuracy of source separation from EEG only.
4. Develop a method for source localisation of EEG data relying on the above model of correlations to increase the precision of source localisation from

EEG only.

5. Develop the framework for more accurate EEG source separation and localisation based on a joint EEG and fMRI model of correlations.

All of the objectives listed above were achieved within the research described in this dissertation. PCA was used to extract a set of generative features both for EEG and fMRI signals, which reduced the dimensionality of the data and removed the unwanted noise. GMM was used to build a model of correlations between EEG and fMRI data.

We modified existing MRJI method for joint EEG-fMRI separation to draw on the fMRI signal generated from the joint EEG-fMRI GMM model and demonstrated an improvement in accuracy in comparison to EEG only source separation.

We also showed an improvement in source localisation when using additional information from the joint EEG-fMRI model.

For testing, we simulated several sources if neural activities with known patterns and locations. The simulated neural activities are created using a damped sinusoid function and combined with the lead field matrix and the hemodynamic response function to simulate EEG and fMRI signals, which used for testing of MN and our own source separation and localisation algorithms in order to compare results of these algorithms with the known ground truth. The algorithm using joint EEG and fMRI data obtains better separation and localisation results than the MN algorithm which uses EEG data only.

7.2 Future work

In the future, this work should be extended to using real EEG and fMRI data to build the GMM model and then it can be applied to real EEG and fMRI datasets. One possible important application of the work presented in this thesis is a Brain Computer Interface based on the EEG signals, as it requires good accuracy of source separation and localisation.

7.3 Publications

Peng, S., Hicks, Y.A., Setchi, R. Joint EEG-fMRI model for EEG source separation. IEEE International Conference on Systems, Man, and Cybernetics (IEEE SMC), San Diego, October 2014.

References

[1]. Bell, A. J. and Sejnowski, T. J. 1995. An information maximization approach to blind separation and blind deconvolution. *Neural Comput*, vol. 7, no. 6, pp. 1129-1159.

[2]. Bledowski, C., Prvulovic, D., Hoechstetter, K., Scherg, M., Wibral, M., Goebel, R. and Linden, D. E. J. 2004. Localizing P300 generators in visual target and distractor processing: A combined event-related potential and functional magnetic resonance imaging study. *Neuroscience*, vol. 24, no. 42, pp. 9353-9360.

[3]. Bonmassar, G., Schwartz, D.P., Liu, A. K., Kwong, K. K., Dale, A. M. and Belliveau J. W. 2001. Spatiotemporal brain imaging of visual-evoked activity using interleaved EEG and fMRI Recordings. *NeuroImage*, vol. 13, no. 6, pp. 1035-1043.

[4]. BrainMaster Technology Inc. (n. d.) The international 10-20 system [online]. Available at: http://www.brainm.com/generalinfo/electrodeuse/eegbands/1020/1020.html

[5]. Brookings, T., Ortigue, S., Grafton, S. and Carlson, J. 2009. Using ICA and realistic BOLD models to obtain joint EEG/fMRI solution to the problem of source location. *NeuroImage*, vol. 44, pp. 411-420.

[6]. Brown, K. S., Ortigue, S., Grafton, S. T. and Carlson, J. M. 2009. Improving human brain mapping via joint inversion of brain electrodynamics and BOLD signal. *NeuroImage*, vol. 49, pp. 2401-2415.

[7]. Brown University. 2012. People with paralysis control robotic arms using brain-computer interface. [Online]. Available at: http://news.brown.edu/articles/2012/05/braingate2

[8]. Coope, I. D. 2000. Reliable computation of the points of intersection of n spheres in n-space, *ANZIAM Journal*, vol. 42, no. 5, pp. 461-477.

[9]. Correa, N. M., Eichele, T., Adali, T., Li, Y-O. and Calhoun, V. D. 2010. Multi-set canonical correlation analysis for the fusion of concurrent single trial ERP and functional MRI. *NeuroImage*, vol. 50, no. 4, pp. 1438-1445.

[10]. David, S. 2007. Multiple hit hypotheses for dopamine neuron loss in Parkinson's disease. *Trends in Neuroscience*, vol. 30, no. 5, pp. 244-250.

[11] Denbener, S., Ullsperger, M., Siegel, M., Fiehler, K., von Cramon, D. Y. and Engel, A. K. 2005. Trail by trail coupling of concurrent electroencephalogram and functional magnetic resonance imaging identifies the dynamics of performance monitoring. *Neuroscience*, vol. 14, no. 25, pp. 11730-11737.

[12]. Eichele, T., Calhoun, V. D., Moosmann, M., Specht, K., Jongsma, M. L., Quiroga, R. Q., Nordby, H. and Hugdahl, K. 2009. Unmixing concurrent EEG-fMRI with parallel independent component analysis. *Int J Psychophysiol*, vol. 67, no. 3, pp. 222-234.

[13] Friston, K. J, Mechelli, A. Turner, R. and Price, J. 2000. Nonlinear response in fMRI: the balloon model volterra kernels and other hemodynamics. *NeuroImage*, vol. 12, pp. 466-477.

[14]. Grech, R., Cassar, T., Muscat, J., Camilleri, K. P., Fabri, S. G., Zervakis, M., Xanthopoulos, P., Sakkalis, V. and Vanrumste, B. 2008. Review on solving the inverse problem in EEG source analysis. *Journal of NeuroEngineering and Rehabilitation*, vol. 5, p. 25.

[15]. Hallez, H., Vanrumste, B., Grech, R., Muscat, J., De Clercq, W., Vergult, A., D'Asseler, Y., Camilleri, K. P., Fabri, S. G., Van Huffel, S. and Lemahieu, I. 2007. Review on solving the forward problem in EEG source analysis. *Journal of NeuroEngineering and Rehabilitation*, vol. 4, p. 46.

[16]. Hamalainen, M. S. and IImoniemi, R. J. 1994. Interpreting magnetic fields of the brain: minimum norm estimates. *Biomedical Engineering*, vol. 32, pp. 35-42.

[17]. Hannah, D. 2005. What is the Functional Magnetic Resonance Imaging (fMRI)? [Online] Available at: http://psychcentral.com/lib/what-is-functional-magnetic-resonance-imaging-fmri/0001056

[18]. Hunter, H. 2009. HITLab, and Affiliate Faculty U.W. Radiology and Psychology. Available at: http://www.hitl.washington.edu/projects/magnet/.

[19]. Hyvarinen, A. and Oja, E. 1997. A fast fixed-point algorithm for independent component analysis. *Neural Comput*, vol. 9, no. 7, pp. 1483-1492.

[20]. Hyvarinen, A., Karhunen, J. and Oja, E. 2001. *Independent component analysis*. Canada: John Wiley and Sons Ltd.

[21]. Jing, M. 2009. *Predictability of epileptic seizures by fusion of scalp EEG and fMRI*. Centre for digital signal processing, Cardiff University.

[22]. Laureys, S. and Schiff, N. 2011. *Coma and consciousness: paradigm reframed by neuroimaging*. Coma Science Group, Cyclotron Research Centre and Neurology Department, University and University Hospital of Liege, 4000 Liege, Belgium. Department of Neurology and Neuroscience, LC-803, Weill Cornell Medical College, 1300 York Ave, New York, NY 10065 USA.

[23] Lei, X., Ostwald, D., Hu, J., Qiu, C., Porcaro, C., Bagshaw, A. P. and Yao, D. 2011. Multimodal function network connectivity: An EEG-fMRI fusion in network space. *PLoS ONE*, vol. 6, no. 9, e24642.

[24]. Liu, A. K., Belliveau, J. W. and Dale, A. M. 1998. Spatiotemporal imaging of human brain activity using functional MRI constrained magnetoencephalography data: Monte Carlo simulations. *Proc Natl Acad Sci (PNAS)*, vol. 95, no. 15, pp. 8945-8950.

[25]. McKeown, M. J., Makeig, S., Brown, G. G., Jung, T.-P., Kindermann, S. S., Bell, A. J. and Sejnowski, T. J., 1998. Analysis of fMRI data by blind separation into independent spatial components. *Hum. Brain Mapp*, vol. 6, pp. 160-188.

[26]. Mulert, C. and Lemieux, L. 2010, *EEG-fMRI*, Berlin: Springer.

[27]. Ogawa, S., Lee, T. M., Kay, A. R. and Tank, D. W. 1990. Brain magnetic resonance imaging with contrast depends on blood oxygenation, *Proc Natl Acad Sci*, vol. 87, pp. 9868-9872.

[28]. Ogawa, S., Lee, T. M., Nayak, A. S. and Glynn P. 1990. Oxygenation-sensitive contrast in magnetic resonance image of rodent brain at high magnetic field. *Magn Reson Med*., vol. 14, pp. 68-78.

[29]. Phillips, C., Mattout, J., Rugg, M. and Friston, K. 2005. An empirical Bayesian solution to the source reconstruction problem in EEG. *NeuroImage*, vol. 24, pp. 997-1011.

[30]. Ritter, P. and Villringer, A. 2006. Simultaneous EEG-fMRI. *ScienceDirect*, vol. 30, pp. 823-838.

[31]. Robinson, P. A., Drysdale, P. M., Van der Merwe, H., Kyriakou, E., Rigozzi, M. K., Germanoska, B. and Rennie, C. J. 2005. BOLD responses to stimuli: dependence on frequency, stimulus form, amplitude, and repetition rate. *NeuroImage*, vol. 31, pp. 585-599.

[32]. Salido Ruiz, R. A., Ranta, R. and Louis-Dorr, V. 2011. EEG montage analysis in blind source separation framework. *Biomedical Signal Processing and Control*, vol. 6, no. 1, pp. 77-84.

[33]. Sanei, S. and Chambers, J. 2007. *EEG signal processing*. Sussex: John Wiley and Sons Ltd.

[34]. Sarvas, J. 1987. Basic mathematical and electromagnetic concepts of the biomagnetic inverse problem. *Physics in Medicine and Biology*, vol. 32, no. 1, pp. 11-22.

[35]. Spyrou, L., Jing, M., Sanei, S. and Sumich, A. 2006. Separation and localization of P300 sources and their subcomponents using constrained blind source separation. *EURASIP Journal*, vol. 2007, no. 1, pp. 89-99.

[36]. Uhle, C. and Reiss, J. 2010. *Determined source separation for microphone recordings using IIR filters.* Audio Engineering Society. San Francisco, CA, USA.

[37]. Vatta, F., Meneghini, F., Esposito, F., Mininel, S. and Disalle, F. 2009. Realistic and spherical head modeling for EEG forward problem solution: A comparative cortex-based analysis. *Computational Intelligence and Neuroscience*. 10.1155/2010/972060.

[38]. Vidal, J. 1977. Real-*time detection of brain events in EEG*. IEEE Proceedings, vol. 65, no. 5, pp. 633-641.

[39]. Weinstein, D., Zhukov, L. and Johnson, C. 2000. Lead-field bases for electroencephalography source imaging. *Biomedical Engineering Society*, vol. 28, pp. 1059-1065.

[40]. Weissman, D. Attention and cognitive control laboratory: What is EEG?

[Online] Available at:
http://www.lsa.umich.edu/psych/danielweissmanlab/whatiseeg.htm

[41]. World Health Organization, Neurology disorders public health challenges. [Online]. Available at:
http://www.who.int/mental_health/neurology/neurological_disorders_report_web.pdf